

THE STRUCTURE AND DYNAMICS OF RINGED GALAXIES. III. SURFACE PHOTOMETRY AND KINEMATICS OF THE RINGED NONBARRED SPIRAL NGC 7531

R. BUTA¹

Mount Stromlo and Siding Spring Observatories, Research School of Physical Sciences, Australian National University

Received 1986 May 2; accepted 1986 October 10

ABSTRACT

The southern galaxy NGC 7531 is a large example of a nonbarred (SA) spiral possessing a very bright inner ring. This paper explores the photometric and kinematic properties of this galaxy via *UBVRI* surface photometry and emission-line spectroscopy. The inner ring is $\sim 4\text{--}6$ times higher in surface brightness than that in NGC 1433, a prototype “theta” spiral previously described in this series, and is also about 2.5 times smaller in linear size. As for NGC 1433, the inner ring of NGC 7531 is a zone of currently active star formation consisting of discrete associations and H II regions superposed within a slightly diffuse old stellar background. The feature is sharp and well defined in color-index maps, which also show that there are large radial color gradients present, the bluest indices being achieved in the outer disk and arms. Diffuse H α emission is found to permeate the entire region inside a radius of 85'', but discrete H II regions are found only within and outside the inner ring.

The velocity field within the inner 85'' is very regular and suggests that the motions in the plane are predominantly circular. This is in spite of the fact that a subtle bar is visible within the inner ring in near-infrared light. A Fourier analysis suggests that the “intermediate zone” between the ring and the outer arms may also be ovaly distorted. This feature, if real, is viewed at an unfavorable orientation for detecting the noncircular motions characteristic of bar-driven gas flow.

An analysis of the rotation curve of NGC 7531 reveals a curious coincidence: the inner ring lies almost exactly at the “turnover radius.” This is unlike the inner rings of typical (intermediate-type) barred spirals, which usually lie well into the flat portion of the rotation curve, but is similar to a coincidence observed for the nuclear rings of such spirals. Arguments are presented which favor a link between the ring and the inner Lindblad resonance. If the velocity dispersion is ignored, this identification leads to a pattern speed which places corotation in the vicinity of the outer arms. These arms are dominated, especially in the southwest region, by recent star formation and are unlike the arms of most recently studied typical barred spirals.

A plausible but uncertain decomposition of the blue-light luminosity distribution is presented. The light distribution cannot be modeled in terms of a simple combination of an $r^{1/4}$ spheroid and exponential disk, but instead the disk must be allowed to have red and blue components with different scale lengths in order to account for the complexity of the light distribution within the inner ring. For the best model, the bulge contributes 13% of the *B*-band luminosity, in reasonable agreement with values for other Sbc spirals.

A large, very low surface brightness galaxy is identified 2.6° west of the center of NGC 7531. This object, known as A2311.8–4353, has a mean blue light effective surface brightness of only 3%–4% of the night sky, and may be a foreground dwarf. Some basic properties of the object are presented in an appendix.

Subject headings: galaxies: individual (NGC 7531) — galaxies: internal motions — galaxies: stellar content — galaxies: structure — nebulae: H II regions

I. INTRODUCTION

The southern spiral galaxy NGC 7531 is one of the brightest and largest examples of a “nonbarred,” or SA, ringed system (de Vaucouleurs 1959). It is one of the prominent members of the nearby Grus cloud (de Vaucouleurs 1956, 1975a), and is also one of the least known members of that cloud. In this series of papers I am exploring the properties of ringed galaxies of all types, and in this paper I present for

¹Visiting Astronomer, Cerro Tololo Inter-American Observatory, which is operated by the Association of Universities for Research in Astronomy, Inc., under contract with the National Science Foundation; and Anglo-Australian Observatory.

NGC 7531 detailed *UBVRI* photographic surface photometry, CCD photometry, and emission-line kinematic data. The galaxy provides a good contrast to NGC 1433, the prototype “theta” spiral which I described previously (Buta 1986b, hereafter Paper II). As in Paper I (Buta 1986a) and Paper II, the purpose of this series is to examine whether the bright rings observed in many galaxies are in general manifestations of the interaction between a nonaxisymmetric perturbation in the mass distribution and its resonances within the disk. It was shown in Paper II that many of the properties of the three ringlike structures in NGC 1433 can be understood in terms of this resonance hypothesis and that the theoretical

models of Schwarz (1979, 1981, 1984a, b, c, 1985) provide the best account of the rings. However, NGC 7531 is so different from NGC 1433 that we need to examine very carefully how this kind of galaxy fits into the theoretical framework.

The main reason why nonbarred ringed systems should be studied equally as intensively as the barred ones is that it was shown by de Vaucouleurs and Buta (1980b; see also Buta and de Vaucouleurs 1982) that the features classified as "inner rings" in such galaxies show a large intrinsic dispersion in size, both in terms of the relative diameter with respect to the isophotal galaxy dimension and in absolute diameter. Athanassoula *et al.* (1982) found the same effect in ring ratios for those SA systems possessing an inner and an outer ring, and the inhomogeneity seems to be present among the rings of both spiral and S0 galaxies. Statistical studies alone have not led to a definitive explanation of its cause. A mixture of resonance features might be involved, and there are reasons to believe that several processes could be at work in forming rings in SA galaxies. We need to study in detail individual examples of SA(r) systems to better understand this inhomogeneity, and to deduce the reasons why the rings should be different from those in SB galaxies.

The morphology of NGC 7531 is described in § II. Section III describes the observations, while § IV presents an analysis of the data. A discussion is presented in § V. Conclusions are presented in § VI.

II. MORPHOLOGY

NGC 7531 is classified in the *Second Reference Catalogue of Bright Galaxies* (de Vaucouleurs, de Vaucouleurs, and Corwin 1976, hereafter RC2) as SA(r)bc. A number of basic parameters of the galaxy, as well as types from other catalogs, are compiled in Table 1.

The photographs in Figure 1 (Plate 1) illustrate the interesting structure of the galaxy. Details of the plates and CCD frames are given in § III. In the long-exposure blue-light photograph (Fig. 1a), a relatively well-defined, patchy two-armed spiral pattern of low surface brightness is visible emerging from an intermediate region. The long-exposure *I*-band photograph (Fig. 1b) barely shows this outer spiral pattern. In Figures 1c and 1d short-exposure photographs show that the overexposed region includes an intensely bright, knotty inner ring that looks obscured on the east side. In *U*-band light the knots in the ring are especially intense (Fig. 1e). Interior to the ring are two prominent dust lanes which are nearly along the major axis of the galaxy. The character of these dust lanes is somewhat similar to those observed in the bars of normal barred spiral galaxies, yet no obvious bar is visible in the interior of the ring in blue light. A definite suggestion that a very weak bar is present is provided only by the near-infrared image. This feature is highlighted by the schematic in Figure 1f, and its presence suggests that the classification of this galaxy could be revised to SAB(r)bc.

The ring structure is different from that observed in NGC 1433. It has a small size relative to the extent of the outer arms, and a much higher surface brightness. The character of the spiral pattern is also worth noting. In their schematic of a cross section of the revised Hubble system, de Vaucouleurs and de Vaucouleurs (1964) highlight the fact that in many

TABLE 1
BASIC PARAMETERS FOR NGC 7531

Parameter	Value	Notes
Right ascension (1950)	23 ^h 12 ^m 05	1
Declination (1950)	-43°52'4	1
<i>l, b</i>	346°4, -64°5	1
SGL, SGB	247°7, 6°2	1
RC2 Hubble type	SA(r)bc	1
RSA Hubble type and luminosity class	Sbc(r) I-II	2
SGC Hubble type and luminosity class	SA(rs)bc? II	3
Adopted type	SAB(r)bc	4
$\log A_e$	0.96 ± 0.01	
$\log D_{25}$	(1.52)	5
$\log R_{25}$	(0.24)	5
θ_0 (1950)	25° ± 1°	6
Mean disk axis ratio	0.45 ± 0.01	6
Inclination <i>i</i>	65° ± 2°	6
B_T	12.04 ± 0.02	
$(B-V)_T$	0.72 ± 0.02	
$(U-B)_T$	0.01 ± 0.02	
$(V-R)_T$	0.53 ± 0.02	
$(V-I)_T$	1.20 ± 0.02	
C_{21}	1.87(<i>U</i>), 1.84(<i>B</i>), 1.89(<i>V</i>)	7
C_{32}	1.93(<i>U</i>), 2.02(<i>B</i>), 2.05(<i>V</i>)	7
C_{31}	3.61(<i>U</i>), 3.72(<i>B</i>), 3.88(<i>V</i>)	7
V_\odot (km s ⁻¹)	1600 ± 5	8

NOTES.—(1) From RC2. (2) From Sandage and Tammann 1981. (3) From Corwin, de Vaucouleurs, and de Vaucouleurs 1985. (4) See text for discussion of this type. (5) These parameters are uncertain because the $\mu_B = 25.0$ mag arcsec⁻² isophote is disturbed by the outer arms. (6) Based on ellipse fits to outer isophotes in the range $2.7 \leq a \leq 2.9$. (7) See de Vaucouleurs 1977 for the definitions of these concentration indices. (8) New value from slit spectroscopy.

typical SA(r) galaxies, the spiral structure is multiarmed and rather nonglobal. NGC 7531 is a type of SA(r) galaxy which nevertheless shows a global two-armed outer spiral pattern (other examples are NGC 4622 and NGC 5364 [Buta 1984]).

The long-exposure plates revealed the presence of a large, low surface brightness galaxy (designated A2311.8–4353) 2.6' west of the center of NGC 7531 (see Fig. 2 [Pl. 2]). This object, whose apparent diameter is more than half that of NGC 7531, has a mean surface brightness less than 5% of night-sky brightness and, judging from its large angular size, could be a foreground dwarf. The object is not, however, resolved on the prime-focus plates obtained for this study. More information on this object is provided in the Appendix.

III. OBSERVATIONS

a) Surface Photometry

Plates for the surface photometry of NGC 7531 were obtained from three sources. The first is a set of plates closely approximating the standard *UBVR* passbands obtained in 1981 July and October at the prime focus of the 4 m telescope of Cerro Tololo Inter-American Observatory (CTIO). These cover a range of exposure times, are of good photometric quality, and were all obtained under good seeing conditions. The second set consists of three plates in the *B_J*, *R_F*, and *I*-band systems obtained at the prime focus of the 3.9 m

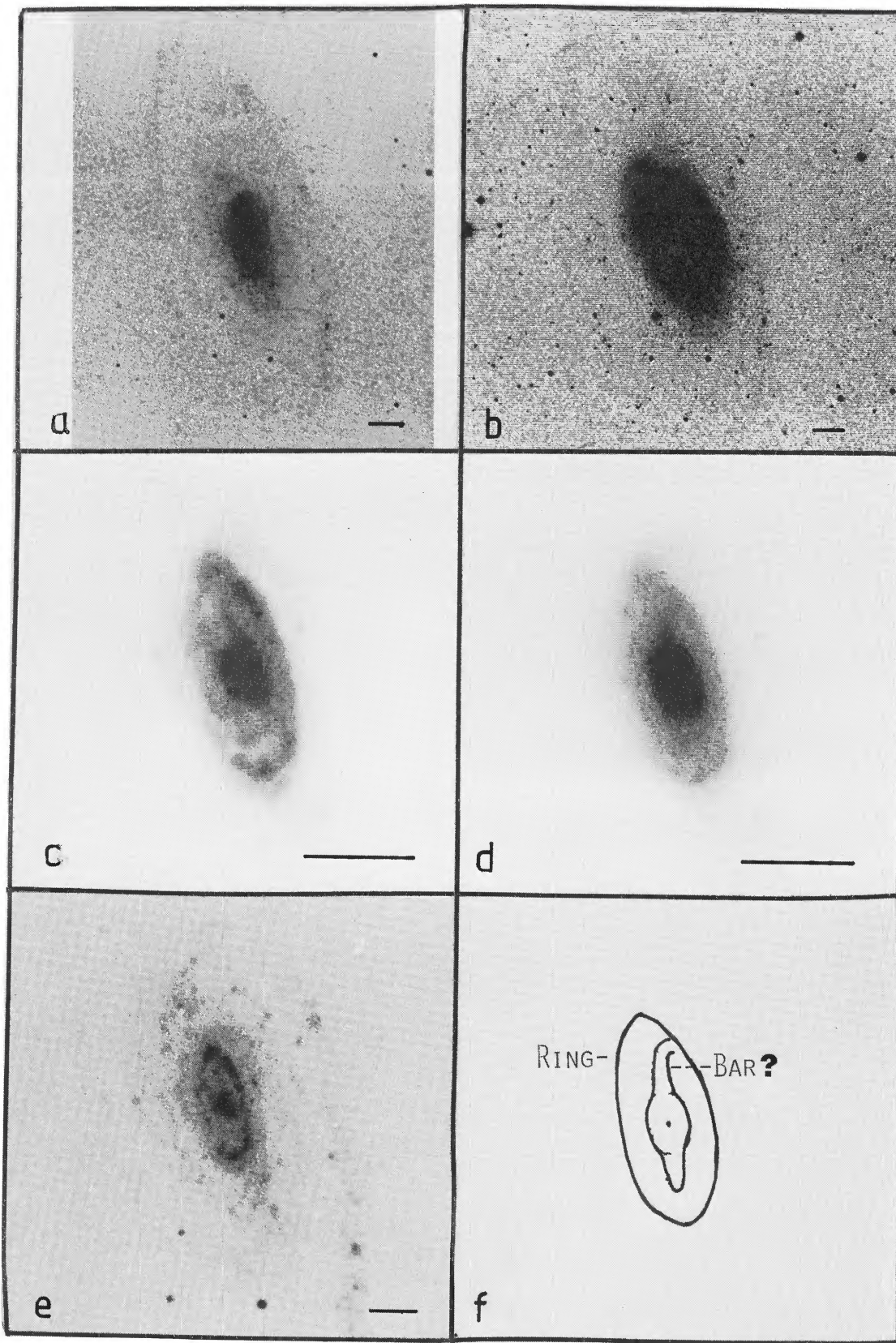


FIG. 1.—Photographs of NGC 7531: (a) from *B*-band CTIO plate 5297; (b) from *I*-band AAT plate 2333; (c) inner ring and nuclear region from a *B*-band CCD frame; (d) inner ring and nuclear region from an *I*-band CCD frame; (e) inner ring and nucleus region from *U*-band CTIO plate 5358; (f) schematic of inner regions highlighting possible weak bar interior to ring. The horizontal line on each image is 30'' in length. North is at the top, and east is to the left.

BUTA (see page 2)

PLATE 2

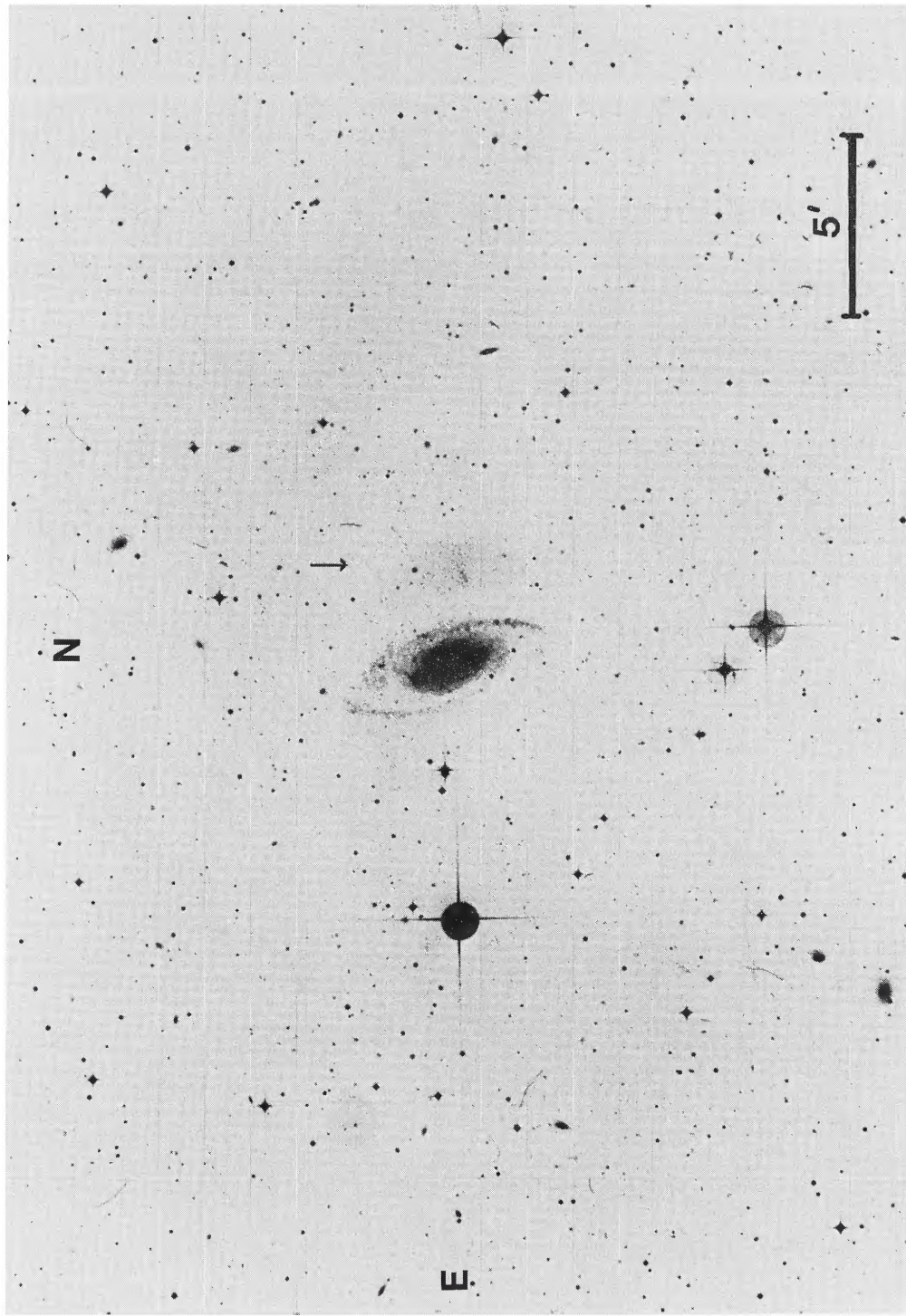


FIG. 2.—Photograph of NGC 7531 showing the dwarf companion A2311.8–4353 (arrow), reproduced from a Science Research Council copy IIIa-J film from the UK Schmidt Southern Sky Survey.
BUTA (see page 2)

TABLE 2A
PLATE MATERIAL FOR SURFACE PHOTOMETRY

Plate Number	Emulsion	Filter	Exposure Time (minutes)	$\langle \mu_s \rangle$ (mag arcsec $^{-2}$)	Mean Error	σ_1	N	$\lambda_{\text{eff}}^{\text{a}}$ (Å)	Plate Scale (arcsec mm $^{-1}$)	Seeing
CTIO Observations										
5297.....	IIa-O	GG 385	30	22.47 ^b	0.006	0.030	23	4360	18.62	1''-2''
5299.....	103a-D	GG 495	55	21.39 ^b	0.006	0.027	24	5500	18.62	2
5306.....	103a-D	GG 495	40	21.04	0.004	0.018	26	5500	18.62	1
5307.....	098-04	RG 610	40	20.51	0.005	0.022	22	6400	18.62	<1
5308.....	IIa-O	GG 385	5	22.20	0.006	0.031	26	4360	18.62	<1
5313.....	103a-D	GG 495	15	21.47 ^b	0.006	0.028	23	5500	18.62	<1
5314.....	098-04	RG 610	15	20.91	0.004	0.011	9	6400	18.62	<1
5358.....	IIa-O	UG 2	75	21.76	0.011	0.056	26	3520	18.62	1
AAT Observations										
2333.....	IV-N	RG 695	90	19.45 ^b	0.004	0.014	16 ^c	7780	16.40	<1
2334.....	IIIa-J	GG 385	15	22.34 ^b	0.007	0.036	24	4560	16.40	<1
2335.....	IIIa-F	RG 630	15	20.60 ^b	0.007	0.018	7	6690	16.40	<1
UKSTU Observations										
J2533	IIIa-J	GG 395	...	22.73 ^d	0.02	4570	67.12	...
I10417 ...	IV-N	RG 715	90	19.59 ^b	0.009	0.040	20 ^c	7880	67.12	...

^aFrom Elmegreen 1980 or Carignan 1983.^bNucleus subtracted.^cZero points were determined using simulated aperture photometry from two *J*-band CCD frames and standard stars.^dA large part of the inner regions of the galaxy was not usable on this copy plate. The zero point was fixed by comparing the azimuthally averaged luminosity profile in the outer regions with that from CTIO plate 5297.

TABLE 2B
CCD MATERIAL FOR SURFACE PHOTOMETRY

Frame (1)	Filter (2)	t (s) (3)	x (4)	$\langle C \rangle$ (5)	Mean Error (6)	σ_1 (7)	n (8)
1	B	300.0	1.408	20.369	0.005	0.024	23
2	B	300.0	1.447	20.362	0.005	0.023	23
1	V	200.0	1.466	19.724	0.003	0.012	23
2	V	200.0	1.499	19.725	0.003	0.013	23
1	R	100.0	1.518	18.999	0.005	0.016	9
2	R	100.0	1.548	18.999	0.005	0.015	9
1	I	100.0	1.562	17.779	...	0.012	...
2	I	100.0	1.591	17.777	...	0.012	...

Col. (1).—CCD frame number.

Col. (2).—Passband (*R* and *I* are Kron-Cousins).

Col. (3).—Integration time.

Col. (4).—Mean airmass.

Col. (5).—Mean zero-point constant (not normalized to sky) ignoring color terms.

Col. (6) and (7).—Mean error and standard deviation of mean zero point.

Col. (8).—Number of aperture photometry measurements used for zero-point calculation; for the *I* band the zero points are based on standard stars and not on aperture photometry.

Anglo-Australian Telescope (AAT) in 1984 October, also under good seeing conditions. The final source consists of a new near-infrared plate and a copy of an older deep IIIa-J plate taken with the United Kingdom Schmidt telescope at Siding Spring Observatory. Details of all of the plates are compiled in Table 2A.

In addition to this plate material, eight frames in the *B*, *V*, *R*, and *I* systems were obtained with the prime-focus CCD camera on the AAT in 1984 December (details are given in Table 2B). These were obtained under somewhat poorer seeing conditions than the plates and a photometric sky. Transformations to the standard systems were provided by observations of five Landolt (1983) standards, using mean extinction coefficients measured in 1984 November. This places the *R* and *I* measurements in the Kron-Cousins systems (Bessell 1979). The adopted transformations were as follows:

$$B - V = 0.369 + 1.193(b - v)_0,$$

$$V = 21.72 + v_0 - 0.003(B - V),$$

$$V - R = 0.077 + 1.002(v - r)_0,$$

$$V - I = 1.355 + 0.971(v - i)_0.$$

where v_0 , $(b - v)_0$, $(v - r)_0$, and $(v - i)_0$ are the extinction-corrected natural indices. Owing to the limited field (2.6' × 4.2') of the CCD, the camera was aligned east-west nearly along

TABLE 3
PHOTOELECTRIC MULAPIERTURE PHOTOMETRY

A	$\log A$ (0.1)	V	$B - V$	$U - B$	$(V - R)_{KC}$	$(V - R)_J$	$(V - I)_{KC}$	Source
9''.6	0.20	13.95	1.00	0.57	0.60	BU (SSO)
9.6.....	0.20	13.96	1.00	0.50	0.57	BU (SSO)
15.4.....	0.41	13.37	0.98	0.47	0.57	BU (SSO)
23.5.....	0.59	12.86	0.93	0.36	0.55	BU (SSO)
23.5.....	0.59	12.90	0.92	0.36	0.56	BU (SSO)
33.2.....	0.74	12.51	0.88	0.31	0.55	BU (SSO)
33.3.....	0.74	12.51	0.85	0.26	...	0.85	...	BU (CTIO)
33.3.....	0.74	12.52	0.84	0.28	...	0.87	...	BU (CTIO)
47.6.....	0.90	12.14	0.83	0.26	0.54	BU (SSO)
47.6.....	0.90	12.14	0.85	0.25	0.53	BU (SSO)
47.6.....	0.90	12.15	0.85	0.29	0.53	BU (SSO)
59.7.....	1.00	11.93	0.81	0.16	GR
65.8.....	1.04	11.86	0.77	0.12	...	0.80	...	BU (CTIO)
65.8.....	1.04	11.85	0.75	0.10	...	0.82	...	BU (CTIO)
65.8.....	1.04	11.86	0.76	0.12	...	0.77	...	BU (CTIO)
90.8.....	1.18	11.67	0.77	0.14	GR
90.8.....	1.18	11.66	0.74	0.15	GR
98.8.....	1.22	11.63	0.77	0.13	...	0.78	...	BU (CTIO)
98.8.....	1.22	11.64	0.73	0.09	...	0.76	...	BU (CTIO)
106.7.....	1.25	11.61	0.76	0.02	SH
131.1.....	1.34	11.54	0.74	0.10	...	0.78	...	BU (CTIO)
131.1.....	1.34	11.51	0.74	0.07	...	0.78	...	BU (CTIO)
131.1.....	1.34	11.52	0.71	0.04	...	0.75	...	BU (CTIO)
135.6.....	1.35	11.52	0.73	0.11	GR
203.0.....	1.53	11.46	0.72	0.00	0.47	...	0.95	SM
207.8.....	1.54	11.38	0.74	0.06	...	0.72	...	BU (SSO)
262.1.....	1.64	11.32:	0.71	0.01	...	0.68	...	BU (CTIO)
262.1.....	1.64	11.25:	0.76	0.09	...	0.68	...	BU (CTIO)

SOURCES.—BU = new CTIO and Siding Spring observations; GR = Griersmith 1980; SH = Shobbrook 1966; SM = R. J. Smyth 1983, private communication.

the short axis of the galaxy to ensure that sky-subtraction errors are minimal. The scale is 0''.49 per pixel.

The photographic surface photometry was performed using the numerical mapping technique of Jones *et al.* (1967). Details of the reductions are given by Buta (1984). The zero points of both the plates and the CCD frames were determined using the multiaperture photoelectric photometry compiled in Table 3. Most of this photometry was obtained by me, using either the CTIO 0.91 m telescope or the SSO 0.6 and 1.0 m telescopes. Other measurements were taken from a general compilation of UBV data (Longo and de Vaucouleurs 1983).

Figure 3 illustrates the results of the calibration for (a) the plates and (b) the CCD frames separately. The zero points are reasonably independent of aperture diameter in both cases, but the scatter is smaller for the CCD frames. The standard deviation is 0.017 mag for these, compared with 0.031 mag for the photographic plates. Some of the larger scatter for the plates is due to the fact that the calibration had to be made in annular apertures owing to slight overexposures of the center. There is also a slight slope in the calibrations in the sense that the zero-point constants decrease slightly with increasing aperture size. This is mostly due to a small zero-point disagreement between the Siding Spring and CTIO photoelectric observations. Note that for the CCD frames, the color terms derived above were taken into account. This is especially important for the B band, in order that the zero points from the standard stars and aperture photometry may

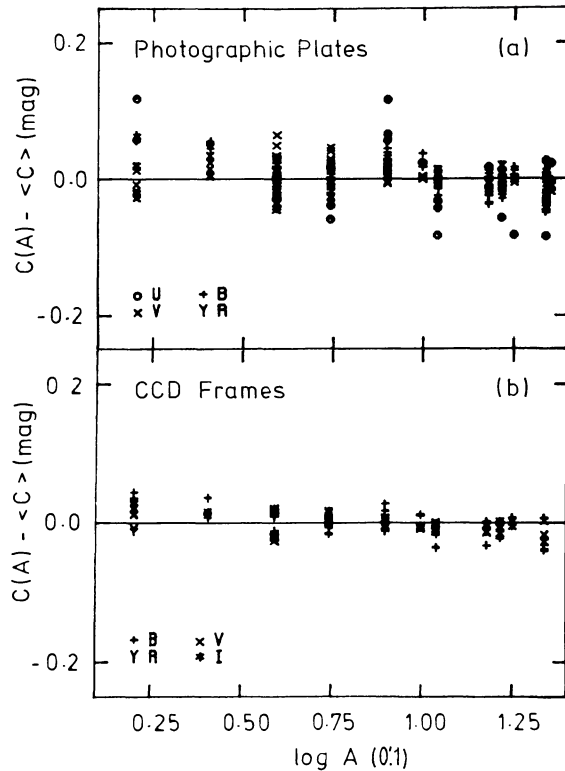


FIG. 3.—Zero-point residuals from multiaperture photometry for (a) photographic plates; (b) CCD photometry.

be directly compared. From simulated aperture photometry, the following mean differences are found:

$$\langle V_{\text{SS}} - V_{\text{AP}} \rangle = -0.022 \pm 0.011 (\text{s.d.}), \quad N = 22,$$

$$\langle (B-V)_{\text{SS}} - (B-V)_{\text{AP}} \rangle = +0.004 \pm 0.021 (\text{s.d.}), \quad N = 22,$$

$$\langle (V-R)_{\text{SS}} - (V-R)_{\text{AP}} \rangle = +0.019 \pm 0.005 (\text{s.d.}), \quad N = 8,$$

$$\langle (V-I)_{\text{SS}} - (V-I)_{\text{AP}} \rangle = +0.25, \quad N = 1,$$

where the subscript AP refers to the magnitudes and colors from aperture photometry (Table 3) and SS refers to the magnitudes and colors calculated within the identical apertures from the CCD arrays using the standard star transformations. The differences are satisfactorily small for V , $B-V$, and $V-R$, but not for $V-I$. The single available $V-I$ measurement is from the unpublished photometry obtained with the SSO 0.4 m telescope by R. J. Smyth (1983, private communication), and may be in error. Lacking any additional independent measurements, I cannot further evaluate this discrepancy. The CCD BVR photometry has therefore been calibrated using only the zero points from the more direct aperture photometry calibrations, after taking into account the color terms derived from the standard stars. That for the I band is based solely on the standard stars. The transformations used for the UBV plates are similar to those used by Jensen, Talbot, and Dufour (1981). For the R and I plates, only the zero points in the Kron-Cousins system are used, the I -band zero points being fixed by the CCD calibration. For the J -band plates 2334 and 2533, the transformation $J = B - 0.35(B-V)$ was used to fix zero points following a discussion by Corwin (1981). Since $B-V$ is known throughout the two-dimensional image from the CTIO plates and the CCD frames, the J -plate surface photometry will simply be reduced to the B -band system.

No drift scans were obtained to check more accurately the density-to-intensity conversions for the plates. However, the CCD frames are linear in intensity and can equally well serve this purpose. Figure 4 shows a comparison between major- and minor-axis profiles in B , V , R , and I light for the plates and CCD frames. The profiles were constructed by integrating the flux every $2''$ within apertures whose size was increased with radius to maintain a similar signal-to-noise ratio. Only for the minor axis do the CCD frames allow the comparison to be made to very low intensity levels, while along the major axis the comparisons can be made to only about 2 mag below sky level in each passband. These demonstrate that the photographic photometry is accurate to better than ± 0.05 mag in the intermediate ranges within ± 2 mag of sky brightness. In the nuclear region the agreement is poorer. Differences in seeing can explain some of this disagreement, but more important, in the case of the longer exposure plates, it is more likely that scattered light in the prime-focus optics, or the PDS used for scanning the plates, or a combination of both have led to systematic errors in the nuclear surface brightnesses. In the outer parts the scatter is (not surprisingly) larger, and systematic errors can be virtually entirely attributed to small errors in the sky subtraction, for both the plates and the CCD frames (see, for example, de Vaucouleurs and

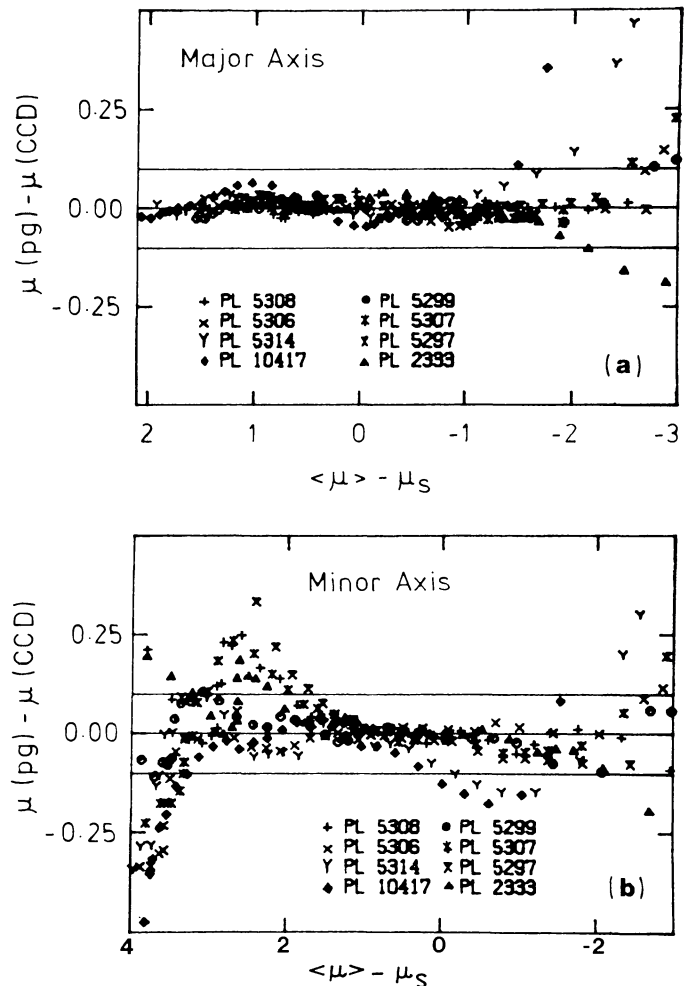


FIG. 4.—Comparison between photographic and CCD profiles along the major and minor axes, as a function of the mean surface brightness relative to the night-sky surface brightness.

Capaccioli 1979). To improve precision in the later analysis, the light distribution will be azimuthally averaged in the galaxy plane.

Table 1 summarizes the standard photometric parameters derived from the new photometry. The total magnitude, $B_T = 12.04 \pm 0.02$, was obtained by extrapolating a mean equivalent luminosity profile (see Buta 1984); it is in good agreement with the revised post-RC2 value of $B_T^w = 11.97 \pm 0.10$. It is also in excellent agreement with the magnitude obtained by fitting a mean growth curve to the aperture photometry (Fig. 5). The best fit is obtained using a revised (post-RC2) standard curve (RSC) for stage $T = 3$ (Sb), which gives $B_T = 12.04 \pm 0.03$ mag. The integrated magnitudes in the other passbands were obtained using the color-aperture relations illustrated in Figure 6. The fully corrected integrated colors, $(B-V)_T^0 = 0.58$, $(U-B)_T^0 = -0.09$, are consistent with a Hubble stage of Sbc-Sc according to the mean color-color relation derived by de Vaucouleurs (1977). The concentration indices $C_{21}(B) = 1.84$, $C_{32}(B) = 2.02$, defined by the ratios of equivalent radii enclosing one-quarter, one-half, and three-quarters of the total light (de Vaucouleurs 1977), are unusual

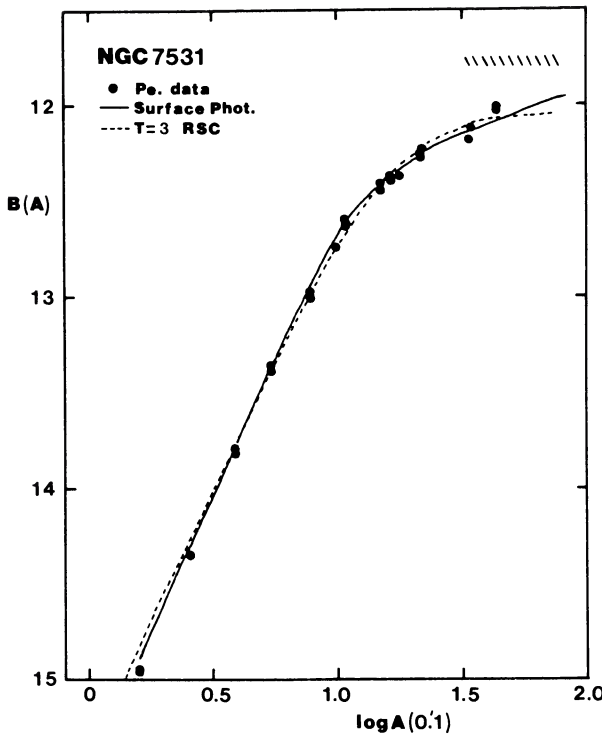


FIG. 5

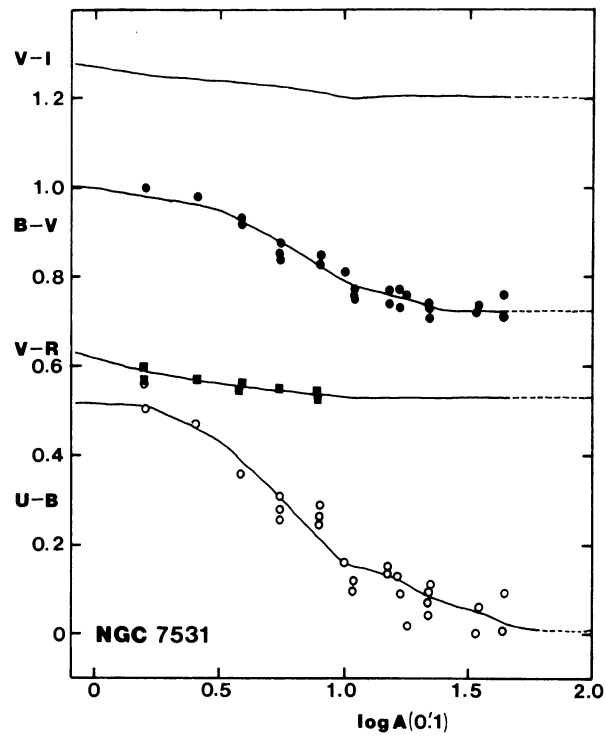


FIG. 6

FIG. 5.—Integrated magnitude-aperture relation of NGC 7531, used as a means for deducing the total magnitude B_T . The solid curve is based on CTIO plates 5297 and 5308, while the dashed curve represents a revised (post-RC2) standard growth curve for stage Sb. Points are from Table 3. Hatched region indicates apertures which would be affected by the nearby dwarf companion.

FIG. 6.—Integrated color-aperture relations of NGC 7531, used as a means for deducing the asymptotic color indices $(U - B)_T$, $(B - V)_T$, $(V - R)_T$, and $(V - I)_T$. Solid curves are based on surface photometry; points are from Table 3.

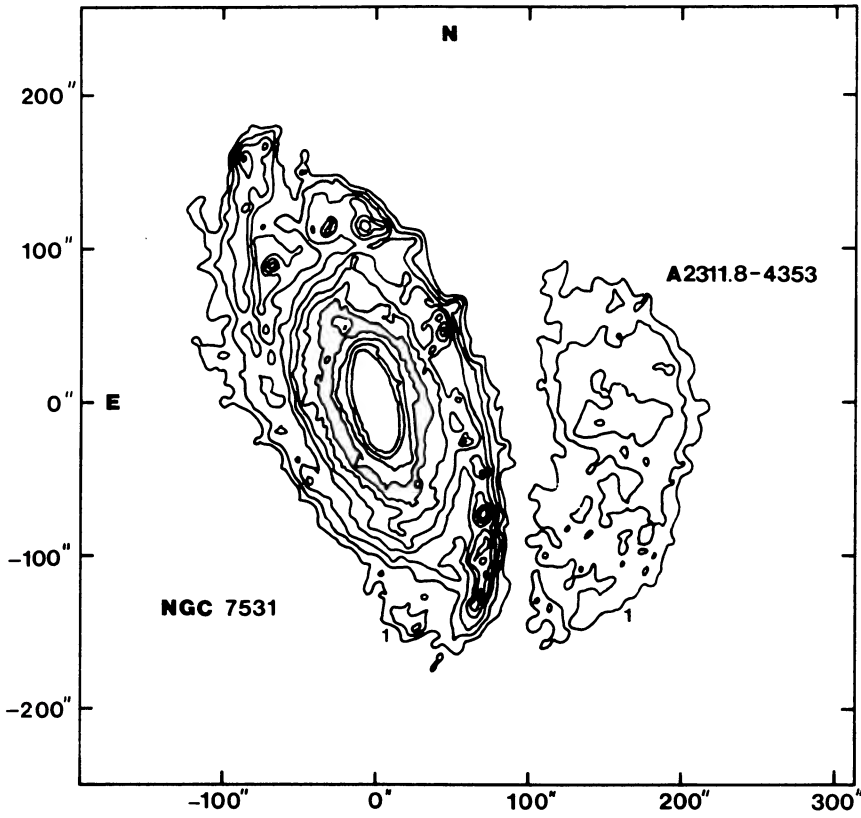


FIG. 7.—Low-resolution B -band isophotes of NGC 7531 and A2311.8-4353 based on CTIO plate 5297. The pixel size is $3'' \times 3''$, and smoothing has been applied according to the surface brightness levels: $\mu_B < 24.4$, no smoothing; $24.4 \leq \mu_B \leq 25.7$, 3×3 point Gaussian smoothing; $\mu_B > 25.7$, 5×5 point Gaussian smoothing. The contours labeled 1 are at the surface brightness level $\mu_B = 26.5$ mag arcsec^{-2} , and successive contours are separated by -0.50 mag.

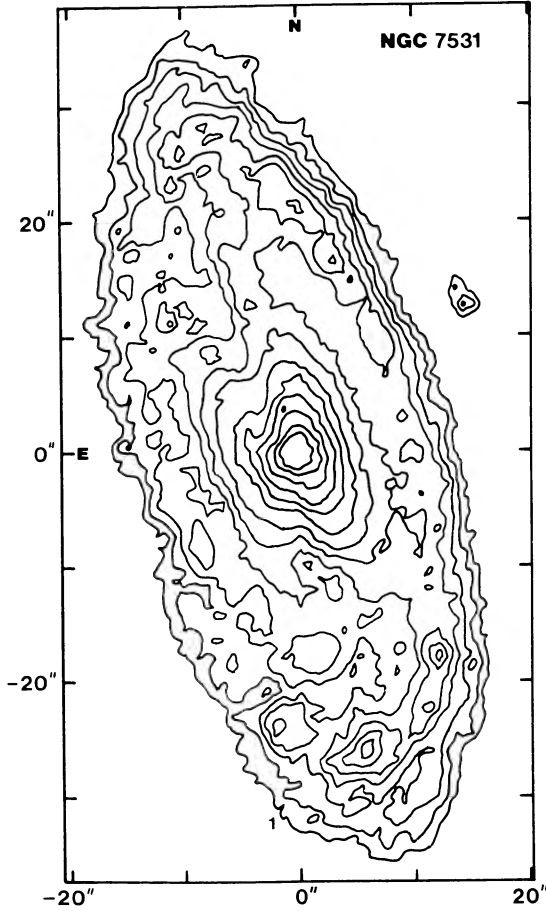


FIG. 8.—High-resolution B -band isophotes of the inner-ring region from CTIO plate 5308. The pixel size is $0\rlap{.}^{\prime\prime}75 \times 0\rlap{.}^{\prime\prime}75$, and no smoothing has been applied. The contour labeled 1 is the level $\mu_B = 21.75$ mag arcsec $^{-2}$, and successive contours are spaced by -0.25 mag.

in the sense that for pure exponential disk or $r^{1/4}$ spheroidal systems, C_{32} is always less than C_{21} , something which should also be true in systems including both an $r^{1/4}$ spheroid and an exponential disk. These concentration indices indicate an unusual light distribution in NGC 7531, and are certainly influenced by the bright, blue inner ring.

Isophote maps of NGC 7531 are presented at two resolutions in Figures 7 and 8. The low-resolution map (Fig. 7) is based on B plate 5297 and has been smoothed in the outer parts. The procedure and the weights used are taken from Jones *et al.* (1967). The maps show that the spiral structure of NGC 7531 disturbs the isophotes even at levels of only 1%–2% of night-sky brightness. This is in contrast to NGC 1433, where the isophotes become well-defined ellipses as the faintest surface brightnesses are reached.

The dwarf companion A2311.8–4353 is visible in this map as the large structure 2.6' west of NGC 7531. The maps reveal that a bar is present in this object, and that, to the same isophote level ($\mu_B = 26.5$ mag arcsec $^{-2}$), it is two-thirds the apparent angular size of NGC 7531. There appears to be no evidence of interaction between these two objects, and it is likely, as mentioned before, that their proximity is a chance superposition. It is nevertheless curious how the curvature of

the isophotes of the dwarf parallel those of the southwest spiral arm of NGC 7531.

The high-resolution map in Figure 8 (based on B plate 5308) is confined to the inner-ring region only. The isophotes of the ring are disturbed on the east side because of absorption in the plane of the galaxy. The linear dust lanes interior to the ring have only a subtle effect on the isophotes, which become nearly round in the nucleus.

Figures 9a and 9b show the axis ratio and position angle curves based on ellipse fits to the illustrated isophotes and to those based on other passbands. The axis ratio of the isophotes is nearly unity in the center but rapidly decreases outward until a minimum is reached at the position of the inner ring. This minimum is probably partly an artifact of the planar absorption which distorts the isophotes from an elliptical shape. At levels $\mu_B \approx 21.5$ mag arcsec $^{-2}$ the isophotes are elliptical in the ring region. This feature has an axis ratio $q_r = 0.42 \pm 0.01$ and major-axis position angle p.a. = $14^\circ \pm 1^\circ$ (1950).

Beyond the inner ring the isophotes are influenced by the spiral structure, and ellipses are poor fits. Fits to the outermost isophotes are reasonably well defined and indicate that the disk has an apparent axis ratio $q_d = 0.45 \pm 0.01$ and major-axis position angle p.a. = $25^\circ \pm 1^\circ$ (1950). The inner

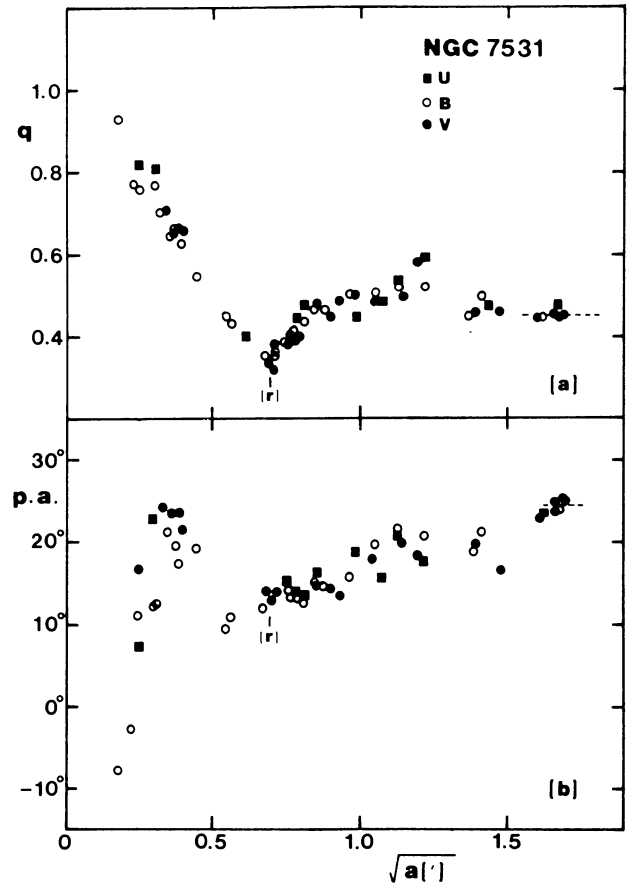


FIG. 9.—(a) Axis ratios (b/a) of isophotes of NGC 7531 based on ellipse fits. The parameter a is the semimajor axis radius. (b) Same as (a), but for the (1950) orientations of the isophotes. The position of the inner ring (r) is indicated.

ring has neither the same shape nor the same orientation as the disk, but the discrepancy is not nearly as significant as was found for NGC 1433.

Maps of the color distribution within NGC 7531 are illustrated in Figure 10 (Plate 3). The high-resolution maps for $B - V$, $V - R$, $B - I$, and $V - I$ are based on the CCD frames only, while the $U - B$ map is based on CTIO plates 5308 and 5358. In all the maps, the inner ring is seen to be a very well-defined feature that is considerably bluer than its surroundings (as in Paper II, “blue” features having $B - V < 0.5$, $U - B < -0.1$ are dark in these maps, while red features having $B - V > 0.8$, $U - B > 0.3$ are light). Except for the possible reddening on the east side (to be confirmed), the ring appears to be an almost completely closed feature rather than a collection of discrete “knots,” although such knots are certainly present. The dark lanes interior to the ring (see Fig. 1c) are visible in all of the maps as a single, nearly straight feature that is redder ($B - V \gtrsim 1.0$) than its surroundings, and hence must be due to dust. Exterior to the ring the $B - V$ color is almost everywhere bluer than in the interior region and includes a scattering of blue knots and large, obvious complexes of star formation.

In Figure 11 (Plate 4) low-resolution maps of the $B - V$ and $U - B$ color distributions are shown. These are based on CTIO plates 5297, 5306, and 5358. As is typical of late-type “grand design” spirals, the outer arms are lined by blue associations. These maps also highlight how the southwest spiral arm seems more affected by this star formation than the northeast arm.

b) Kinematics

The kinematics of the ionized gas in NGC 7531 was obtained from two sources. The first consists of nine spectrograms (Table 4) obtained in 1981 July and October with the Carnegie image-tube spectrograph at the Ritchey-Chrétien focus of the 4 m telescope of Cerro Tololo Inter-American Observatory. These were obtained at dispersions of 50 and 25 \AA mm^{-1} and are of very high quality for velocity work. The second source consists of a two-dimensional frame obtained under very poor sky conditions with the TAURUS Fabry-Perot interferometer (Taylor and Atherton 1980) on the AAT in 1982 November. Details of the reductions of both sets of data are given by Buta (1984).

BUTA

There have been no previously published studies of the kinematics of this galaxy, but the prominence of bright emission in the inner ring has been noted in a recent redshift survey (de Vaucouleurs, de Vaucouleurs, and Nieto 1979). Figure 12 (Plate 5) shows a reproduction of one of the slit spectra. This confirms that the brightest emission is in the inner ring, which is visible in all five major emission lines ($\text{H}\alpha$, $[\text{N II}] \lambda\lambda 6548, 6583$, and $[\text{S II}] \lambda\lambda 6716, 6731$) at about 30'' radius on either side of the nucleus. There is weak diffuse emission throughout the interior of the ring, and even fainter diffuse emission outside of the structure. The intensity of the emission in the ring relative to that outside it is reminiscent of NGC 4736 (van der Kruit 1974, 1976), but it does not appear to be as sharply bounded. The entire inner region whose continuum is plainly visible in Figure 12 appears to be filled with diffuse emission.

The errors in the new velocity measurements were obtained by computing a velocity profile in each of the position angles of the slit spectra (V_S) from the two-dimensional array of TAURUS velocities (V_T). From 65 overlapping points in 12 position angles, the mean differences were found to be $\langle V_T - V_S \rangle = -6 \pm 2 \text{ km s}^{-1}$, with $\sigma(\text{ST}) = 14.1 \text{ km s}^{-1}$. A small but significant zero-point difference between the two data sets is indicated, and, for the purposes of the later analyses, 6 km s^{-1} will be added to the TAURUS data to reduce it to the zero point of the slit spectra.

If the errors in the two velocity data sets are equal, then this analysis also implies $\sigma_S = \sigma_T = 10 \text{ km s}^{-1}$. However, most of the points in this comparison involve the inner ring, where the emission is very bright on the well-exposed spectra. From a comparison of the grating 420 spectra F1976A and F1976B with the grating 380 spectra F2036B and F2035B in the same position angles, the internal error in these bright regions is only 5 km s^{-1} . If this is more representative of the total errors in the slit spectrum velocities, then the errors in the TAURUS velocities would be $\sigma_T \approx 13 \text{ km s}^{-1}$. This larger total error is not unreasonable because the TAURUS velocities are based on only one line, and the data were obtained during poor observing conditions. The slit spectrum velocities are based on four or five lines in the ring, and the spectra were obtained during excellent observing conditions. Table 5 lists the velocity measurements from the spectrograms. The TAURUS velocities are not given, but these will be made available on request from the author.

TABLE 4
LOG OF CTIO CARNEGIE IMAGE-TUBE SPECTROGRAMS

CTIO Number	Position Angle	Exposure Time (minutes)	Nominal Dispersion (\AA mm^{-1})	Grating Number	Slit Width (μm)	Comparison Arc	Date 1981
F1976A.....	12°5	75	50	420	150	Ne	July 3
F1976B.....	102. 5	75	50	420	150	Ne	July 3
F1977A.....	43. 0	60	50	420	150	Ne	July 3
F1983A.....	21. 0	75	50	420	150	Ne	July 4
F1983B.....	133. 0	74	50	420	150	Ne	July 4
F1984A.....	2. 5	75	50	420	150	Ne	July 4
F2034B.....	153. 5	90	25	380	250	He-Ne-Ar	October 4
F2035B.....	102. 5	100	25	380	225	He-Ne-Ar	October 4
F2036B.....	12. 5	90	25	380	225	He-Ne-Ar	October 4

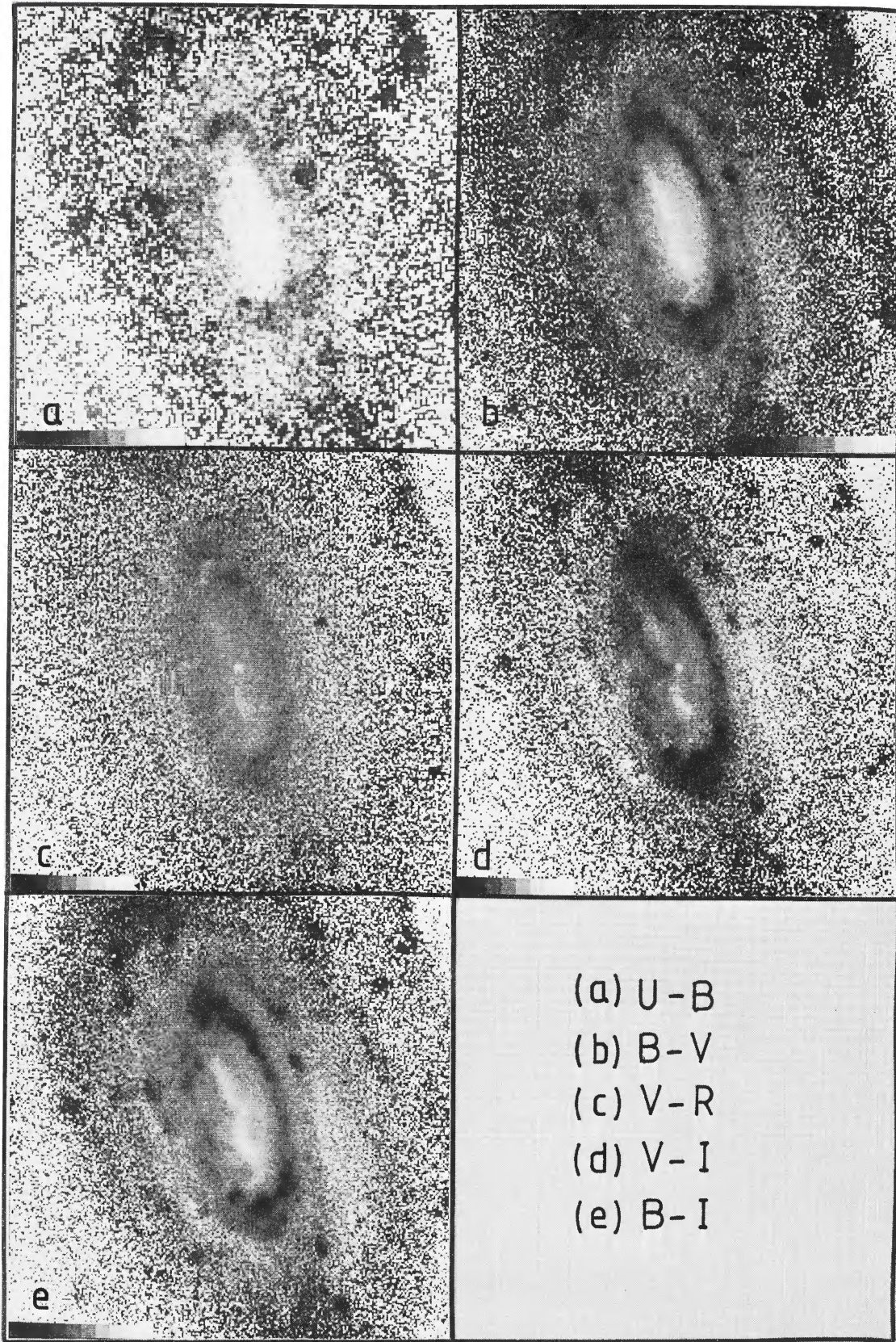


FIG. 10.—Detailed maps of the color distribution within the inner-ring region of NGC 7531. The gray scales are such that the sense *dark to light* corresponds to the sense *blue to red*. The scales are (*far left value, increment*): (a) (-0.6, 0.2), (b) (0.3, 0.1), (c) (0.1, 0.1), (d) (0.8, 0.1), (e) (0.9, 0.2). Note striking blue color ($B - V \sim 0.6$) of the inner ring, and the red dust lane ($B - V \approx 1.0$) interior to the ring.

BUTA (see page 8)

PLATE 4

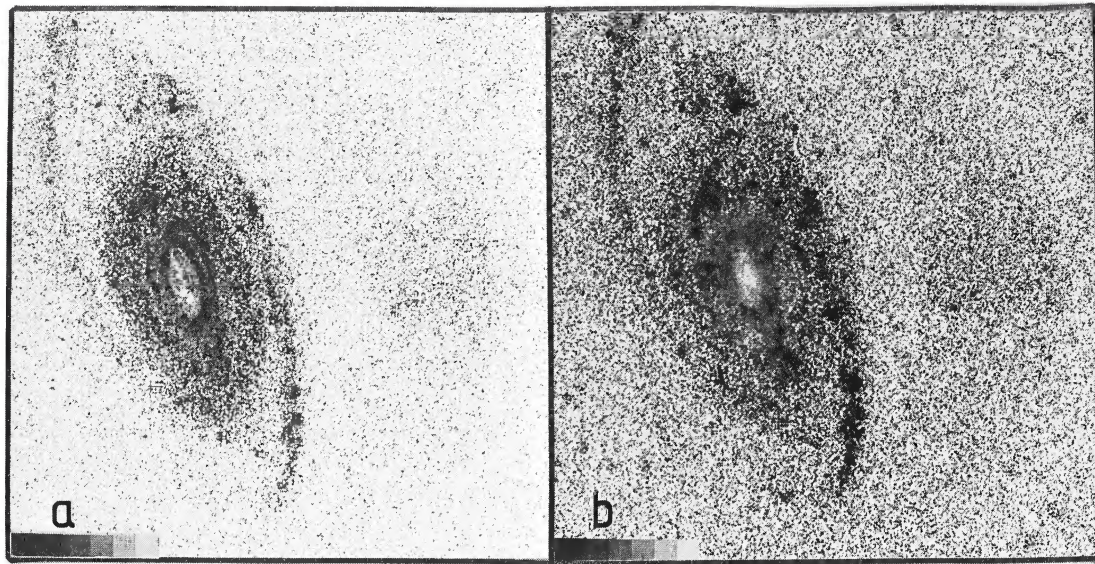


FIG. 11.—Maps of the large-scale color distribution within NGC 7531 for (a) $B - V$ and (b) $U - B$. Gray scales are the same as for Figs. 10b and 10a respectively. Note the patchy blue outer spiral arms.

BUTA (see page 8)

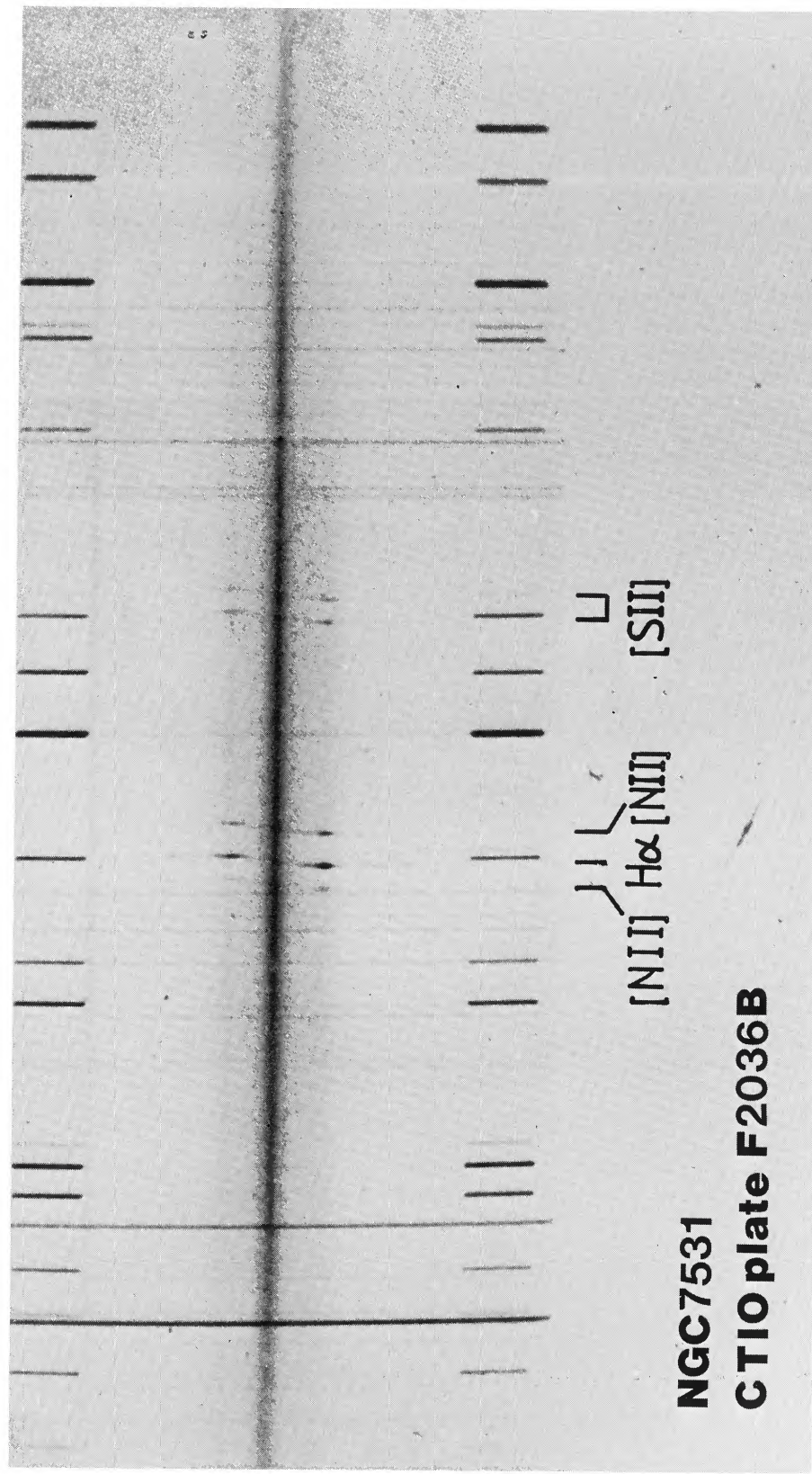


FIG. 12.—Reproduction of a spectrogram of NGC 7531 taken with the CTIO Carnegie image-tube spectrograph. The inner ring is visible as the maximum of emission in all five emission lines indicated.
BUTA (see page 8)

TABLE 5
CTIO SII λ SPECTRUM VELOCITIES

r	p. a.	V _θ	m.e. n	r	p. a.	V _θ	m.e. n	r	p. a.	V _θ	m.e. n	r	p. a.	V _θ	m.e. n	r	p. a.	V _θ	m.e. n			
1	2	3	4	5	1	2	3	4	5	1	2	3	4	5	1	2	3	4	5			
F1976A	192.5	1721	3	-53.9	282.5	1598	..	1	-32.7	223.0	1711	11	-49.1	201.0	1744	2	4	66.3	21.0	1446		
-62.2	192.5	1752	1	-51.2	282.5	1663	..	1	-30.4	223.0	1710	8	-46.8	201.0	1765	14	4	68.6	21.0	1424		
-59.9	192.5	1769	..	-42.4	282.5	1634	20	2	-28.1	223.0	1715	4	-44.5	201.0	1766	11	3	-52.3	182.5	1719		
-39.1	192.5	1749	4	-40.7	282.5	1618	7	2	-25.8	223.0	1713	6	-39.8	201.0	1764	9	2	-45.3	182.5	1738		
-36.8	192.5	1749	4	-37.7	282.5	1609	27	3	-21.1	223.0	1717	6	-37.5	201.0	1715	10	3	-40.7	182.5	1690		
-34.5	192.5	1758	8	-35.4	282.5	1621	..	1	-18.8	223.0	1712	1	-35.2	201.0	1761	6	5	-36.1	182.5	1719		
-32.2	192.5	1750	4	-33.1	282.5	1608	33	2	-16.5	223.0	1710	3	-32.9	201.0	1763	3	5	-33.8	182.5	1702		
-29.9	192.5	1745	2	-28.5	282.5	1631	..	1	-14.2	223.0	1692	2	-30.6	201.0	1753	3	5	-34.4	182.5	1754		
-27.6	192.5	1750	2	-21.6	282.5	1618	1	-11.9	223.0	1669	13	-26.0	201.0	1758	5	5	-31.5	182.5	1754			
-25.3	192.5	1750	2	-23.0	192.5	1753	3	4	-19.3	282.5	1607	10	-9.6	223.0	1679	6	3	-29.6	182.5	1741		
-20.7	192.5	1734	5	-17.7	282.5	1608	6	4	-5.3	223.0	1691	..	-21.4	201.0	1732	7	5	-60.7	182.5	1736		
-18.4	192.5	1710	4	-14.7	282.5	1601	5	4	-5.0	223.0	1647	..	-19.1	201.0	1734	5	5	-60.7	182.5	1725		
-16.0	192.5	1711	3	-12.4	282.5	1603	8	4	-2.7	223.0	1630	13	-16.8	201.0	1732	4	5	-20.0	182.5	1710		
-13.7	192.5	1709	1	-10.1	282.5	1612	13	3	-0.4	223.0	1616	7	-14.5	201.0	1766	9	4	-17.6	182.5	1673		
-11.4	192.5	1709	20	-7.8	282.5	1607	10	3	-1.9	223.0	1576	8	-12.2	201.0	1665	8	4	-13.0	182.5	1641		
-9.1	192.5	1665	11	4	-5.4	282.5	1618	67	2	4.2	43.0	1561	4	-9.9	201.0	1738	2	5	-63.0	182.5	1731	
-6.8	192.5	1680	10	2	-3.1	282.5	1649	8	2	6.5	43.0	1558	5	-7.5	201.0	1677	7	2	-46.9	182.5	1681	
-4.5	192.5	1648	2	-0.8	282.5	1595	27	2	8.8	43.0	1538	2	-5.2	201.0	1601	30	4	-44.6	182.5	1645		
-2.2	192.5	1626	..	1	1.5	102.5	1580	8	4	11.2	43.0	1525	8	-2.9	201.0	1629	16	4	-33.9	182.5	1594	
0.1	12.5	1581	..	1	3.8	102.5	1574	4	3	13.5	43.0	1509	2	-0.6	201.0	1621	11	3	-33.1	182.5	1583	
2.4	12.5	1602	5	6.1	102.5	1574	6	3	15.8	43.0	1501	3	4	1.7	21.0	1574	7	4	-30.7	182.5	1599	
4.7	12.5	1558	3	4	8.4	102.5	1559	6	4	18.1	43.0	1494	4	4.0	21.0	1559	9	4	-28.5	182.5	1578	
7.0	12.5	1538	5	10.7	102.5	1578	9	4	20.4	43.0	1489	2	6.3	21.0	1619	7	2	-16.9	182.5	1548		
9.3	12.5	1506	10	3	13.0	102.5	1591	9	4	22.7	43.0	1493	3	8.6	21.0	1525	4	4	-26.2	182.5	1543	
11.6	12.5	1521	11	2	15.3	102.5	1579	4	4	25.0	43.0	1487	8	4	10.9	21.0	1517	15	4	-23.9	182.5	1537
13.9	12.5	1498	3	17.6	102.5	1588	7	4	27.3	43.0	1495	3	13.2	21.0	1567	5	5	-10.0	182.5	1546		
16.3	12.5	1501	6	4	19.9	102.5	1581	4	4	29.6	43.0	1501	3	15.5	21.0	1574	11	3	-17.0	182.5	1593	
18.6	12.5	1491	2	4	22.2	102.5	1569	3	4	31.9	43.0	1505	12	4	17.8	21.0	1465	7	4	-14.7	182.5	1584
20.9	12.5	1481	5	4	24.5	102.5	1572	5	2	34.2	43.0	1508	6	4	20.1	21.0	1468	8	4	-12.4	182.5	1566
23.2	12.5	1468	3	4	26.9	102.5	1584	10	3	36.5	43.0	1507	..	2	22.4	21.0	1465	5	4	-10.0	182.5	1568
25.5	12.5	1455	3	4	29.2	102.5	1565	6	4	38.8	43.0	1513	..	1	24.8	21.0	1454	2	4	-7.8	182.5	1583
27.8	12.5	1454	2	4	36.1	102.5	1588	7	4	41.1	43.0	1493	2	3	27.1	21.0	1481	1	4	-17.0	182.5	1583
30.1	12.5	1456	4	4	38.4	102.5	1599	..	1	43.0	43.0	1495	12	4	29.4	21.0	1441	3	4	-3.0	182.5	1584
32.4	12.5	1459	2	4	40.7	102.5	1601	..	1	45.8	43.0	1503	12	4	31.7	21.0	1441	3	4	-0.7	182.5	1548
34.7	12.5	1451	3	3	45.3	102.5	1561	21	2	48.1	43.0	1509	13	2	34.0	21.0	1430	2	2	1.5	182.5	1479
37.7	12.5	1465	9	2	56.8	102.5	1501	4	2	50.4	43.0	1478	10	3	36.3	21.0	1434	4	4	3.8	182.5	1486
39.3	12.5	1451	4	2	63.8	102.5	1554	..	1	52.7	43.0	1499	6	2	38.6	21.0	1445	14	4	3.8	182.5	1483
43.9	12.5	1486	..	1	-106.5	223.0	1767	5	3	-55.0	43.0	1491	16	2	40.9	21.0	1464	17	2	8.3	182.5	1481
50.9	12.5	1433	12	3	-104.2	223.0	1749	7	4	-74.4	201.0	1785	..	1	45.5	21.0	1471	0	2	42.3	182.5	1489
53.2	12.5	1455	14	2	-101.9	223.0	1739	4	4	-52.1	201.0	1743	7	4	47.8	21.0	1436	6	4	45.6	182.5	1456
55.5	12.5	1452	1	2	-99.6	223.0	1731	11	4	-69.8	201.0	1742	7	4	50.1	21.0	1434	5	4	109.2	182.5	1452
57.8	12.5	1449	8	3	-97.3	223.0	1737	14	3	-62.9	201.0	1740	..	1	52.4	21.0	1428	1	4	111.5	182.5	1476
66.2	12.5	1483	..	1	-95.0	223.0	1743	5	4	-60.6	201.0	1741	13	5	54.7	21.0	1423	1	4	113.9	182.5	1536
78.5	12.5	1479	..	1	-92.7	223.0	1723	3	3	-58.3	201.0	1701	17	3	57.1	21.0	1430	13	4	118.5	182.5	1508
115.5	12.5	1500	1	2	-55.7	223.0	1705	10	3	-56.0	201.0	1729	8	2	59.4	21.0	1466	12	4	120.8	182.5	1440
117.8	12.5	1428	18	3	-53.4	223.0	1706	..	1	-53.7	201.0	1729	4	4	61.7	21.0	1456	17	3	55.7	182.5	1531
120.1	12.5	1505	9	2	-35.0	223.0	1718	7	3	-51.4	201.0	1736	9	5	61.0	21.0	1448	14	4	-53.4	182.5	1533
122.4	12.5	1486	0	2	-23.0	223.0	1736	..	1	-5.7	201.0	1733	..	1	-56.9	21.0	1482	14	4	-53.4	182.5	1533

BUTA

TABLE 5—Continued

r 1	p. a. 2	V_\odot 3	m.e. 4	n 5	r 1	p. a. 2	V_\odot 3	m.e. 4	n 5	r 1	p. a. 2	V_\odot 3	m.e. 4	n 5
-51.1	153.5	1539	7	2	-37.2	282.5	1599	..	1	-25.0	192.5	1753	2	5
-48.7	153.5	1526	15	3	-32.6	282.5	1581	..	1	-22.7	192.5	1753	1	5
-46.4	153.5	1551	11	3	-30.2	282.5	1629	5	2	-20.4	192.5	1748	3	5
-44.1	153.5	1549	12	3	-27.7	282.5	1610	..	1	-18.1	192.5	1730	6	4
-41.8	153.5	1532	29	3	-25.7	282.5	1603	..	1	-15.9	192.5	1709	6	3
-37.1	153.5	1538	..	1	-23.2	282.5	1613	11	2	-13.5	192.5	1688	20	3
-34.9	153.5	1550	13	3	-20.9	282.5	1603	3	3	-11.2	192.5	1687	22	4
-32.6	153.5	1536	10	3	-18.6	282.5	1606	6	4	-8.9	192.5	1678	4	4
-30.2	153.5	1519	19	4	-16.3	282.5	1603	2	4	-6.6	192.5	1654	6	4
-27.9	153.5	1536	5	5	-14.1	282.5	1608	10	3	-4.3	192.5	1634	21	4
-25.6	153.5	1535	3	4	-11.7	282.5	1613	5	4	-2.0	192.5	1611	11	5
-23.3	153.5	1536	4	4	-9.4	282.5	1616	6	4	0.3	12.5	1590	16	3
-21.0	153.5	1533	3	5	-7.1	282.5	1615	8	4	2.6	12.5	1562	5	4
-18.7	153.5	1528	2	5	-4.7	282.5	1611	4	3	4.9	12.5	1565	4	5
-16.4	153.5	1539	3	5	-2.5	282.5	1580	15	2	7.2	12.5	1541	10	3
-14.1	153.5	1546	2	5	-0.1	282.5	1580	13	3	9.6	12.5	1537	18	3
-11.8	153.5	1552	2	4	2.1	102.5	1586	8	3	11.8	12.5	1515	21	2
-9.5	153.5	1557	6	5	4.3	102.5	1591	7	2	14.2	12.5	1498	10	3
-7.2	153.5	1573	15	2	6.8	102.5	1592	5	3	16.5	12.5	1479	8	4
-4.9	153.5	1553	34	2	9.1	102.5	1562	9	3	18.8	12.5	1481	4	3
-2.6	153.5	1576	9	2	11.4	102.5	1572	4	4	21.1	12.5	1475	2	5
-0.3	153.5	1591	6	2	13.6	102.5	1589	12	3	23.4	12.5	1466	3	5
2.1	333.5	1591	2	2	15.9	102.5	1588	8	3	25.7	12.5	1461	2	5
4.4	333.5	1624	10	2	18.3	102.5	1585	5	4	28.0	12.5	1457	2	5
6.7	333.5	1633	1	2	20.6	102.5	1586	4	4	30.3	12.5	1455	2	5
9.0	333.5	1597	3	3	22.9	102.5	1573	6	3	32.6	12.5	1452	2	4
11.3	333.5	1605	6	3	25.2	102.5	1573	6	4	35.0	12.5	1453	3	4
13.6	333.5	1629	2	2	27.5	102.5	1558	3	3	37.3	12.5	1448	5	4
15.8	333.5	1658	8	2	29.8	102.5	1566	5	3	39.5	12.5	1469	5	3
18.1	333.5	1664	12	2	32.1	102.5	1562	6	3	42.0	12.5	1456	..	1
20.5	333.5	1667	6	2	34.3	102.5	1545	8	2	44.3	12.5	1448	..	1
22.8	333.5	1671	..	1	36.6	102.5	1533	..	1	46.4	12.5	1409	..	1
25.1	333.5	1687	..	1	F2036B					48.7	12.5	1416	20	2
27.4	333.5	1682	..	1	-68.9	192.5	1729	..	1	51.1	12.5	1429	7	2
29.7	333.5	1668	..	1	-66.6	192.5	1718	11	2	53.3	12.5	1442	..	1
32.0	333.5	1673	..	1	-64.3	192.5	1738	..	1	55.7	12.5	1453	1	2
34.3	333.5	1684	..	1	-61.9	192.5	1739	0	2	58.0	12.5	1434	0	2
36.6	333.5	1668	3	2	-59.7	192.5	1744	..	1	60.4	12.5	1446	..	1
38.9	333.5	1618	..	1	-57.3	192.5	1728	3	2	62.6	12.5	1440	..	1
41.2	333.5	1658	2	2	-55.1	192.5	1724	..	1	64.9	12.5	1428	7	2
43.5	333.5	1644	0	2	-50.3	192.5	1740	..	1	69.6	12.5	1430	11	2
45.8	333.5	1647	1	2	-43.4	192.5	1704	..	1	71.9	12.5	1471	10	2
48.1	333.5	1642	..	1	-41.2	192.5	1748	19	2	74.1	12.5	1432	..	1
50.4	333.5	1616	..	1	-38.8	192.5	1757	8	3	76.4	12.5	1452	..	1
F2035B					-36.6	192.5	1775	4	4	78.8	12.5	1469	19	3
-46.4	282.5	1671	..	1	-34.3	192.5	1765	5	5	81.1	12.5	1429	12	2
-44.1	282.5	1638	..	1	-32.0	192.5	1762	5	5	83.5	12.5	1441	..	1
-41.8	282.5	1618	5	2	-29.7	192.5	1752	1	5					
-39.5	282.5	1634	19	2	-27.3	192.5	1752	2	5					

NOTES.—Col. (1): radius (arcsec) from nucleus. Col. (2): position angle (degrees) of slit. Col. (3): weighted mean heliocentric radial velocity (km s^{-1}). Col. (4): mean error of weighted mean velocity. Col. (5): number of lines in mean. If all five lines were visible, the weights adopted were $w(\text{H}\alpha) = 1.0$, $w([\text{N II}] \lambda 6584) = 0.5$, and $w = 0.25$ for the others.

Figure 13 shows the distribution of velocity points based on the combined data from the slit spectra and the TAURUS observations. Emission is seen to be concentrated in the broad zone at the inner ring but is weak on the east side. Outside the ring a few isolated H II regions were detected with TAURUS, but only the slit spectra were exposed to faint enough levels to detect the diffuse emission throughout the inner regions.

The velocity field of NGC 7531 was obtained by averaging the data in $5'' \times 5''$ cells, and interpolating where possible. It is shown with and without smoothing in Figures 14a and 14b. The coverage is somewhat incomplete inside and outside the ring, but it is clear from both figures that the velocity field is fairly regular. However, both maps show that some of the isovelocity contours do not cross the major axis orthogonally but show a very subtle counterclockwise bending. This suggests that some nonaxisymmetric motion may be present. The phase of the possible nonaxisymmetric component responsible for this is evaluated in § IVe.

IV. DATA ANALYSIS

a) Spatial Orientation and Distance

The spatial orientation of NGC 7531 can be obtained from both the photometry and the kinematics. Unfortunately, the shape of the isophote at the surface brightness level $\mu_B = 25.0 \text{ mag arcsec}^{-2}$, often used for deriving inclinations (Bottinelli *et al.* 1983), is not reliable for NGC 7531 because this isophote is greatly disturbed by the spiral structure. The isophotes in blue light are best defined at the lowest light levels ($\mu_B \approx 26.6 \text{ mag arcsec}^{-2}$), where ellipse fits indicate a disk axis ratio of 0.45. The true flattening of NGC 7531 is unknown, but if we assume that it is average for its type, then by equations (1) and (2) of Bottinelli *et al.* (1983) the inclination is $65^\circ \pm 2^\circ$. The surface photometry also indicates that the major axis is in position angle $25^\circ \pm 1^\circ$.

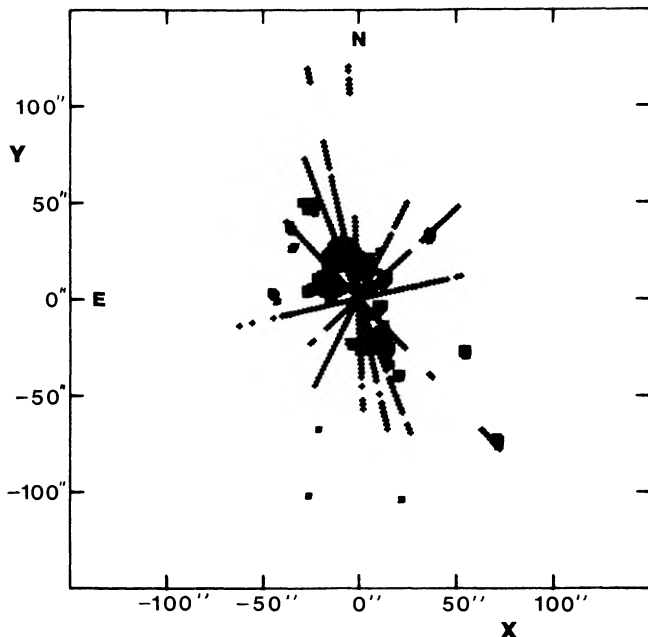


FIG. 13.—Distribution of radial velocity points based on slit spectroscopy and TAURUS Fabry-Perot interferometry. A few local field stars are also shown for reference.

TABLE 6
DISTANCE MODULUS OF NGC 7531

Method	μ_0	w	Notes
Luminosity index and $B_T^0, \log D_0$...	31.88	1.00	1
21 cm line width and $B_T^0, \log D_0$...	31.07	1.00	2
21 cm line width and $H_{-0.5}^c$...	30.75	1.00	3
Inner-ring diameter d_r ...	30.61	0.25	4
Radial velocity ...	30.78	0.25	5
Weighted mean ...	31.16	...	
Internal mean error ...	0.23	...	
Standard deviation ...	0.54	...	

NOTES.—(1) Based on SGC and RSA luminosity classifications and types ($\langle A_c \rangle = 0.65$). (2) Based on unpublished Parkes observations (G. and A. de Vaucouleurs 1983). (3) From Aaronson *et al.* 1981, reduced to zero point of de Vaucouleurs's distances to M31 and M33, and adjusted to the inclination derived in this paper. (4) Based on three-parameter calibration of Buta and de Vaucouleurs 1982. (5) Based on new radial velocity (1600 km s⁻¹) reduced to reference frame defined by nearby galaxies (de Vaucouleurs and Peters 1981).

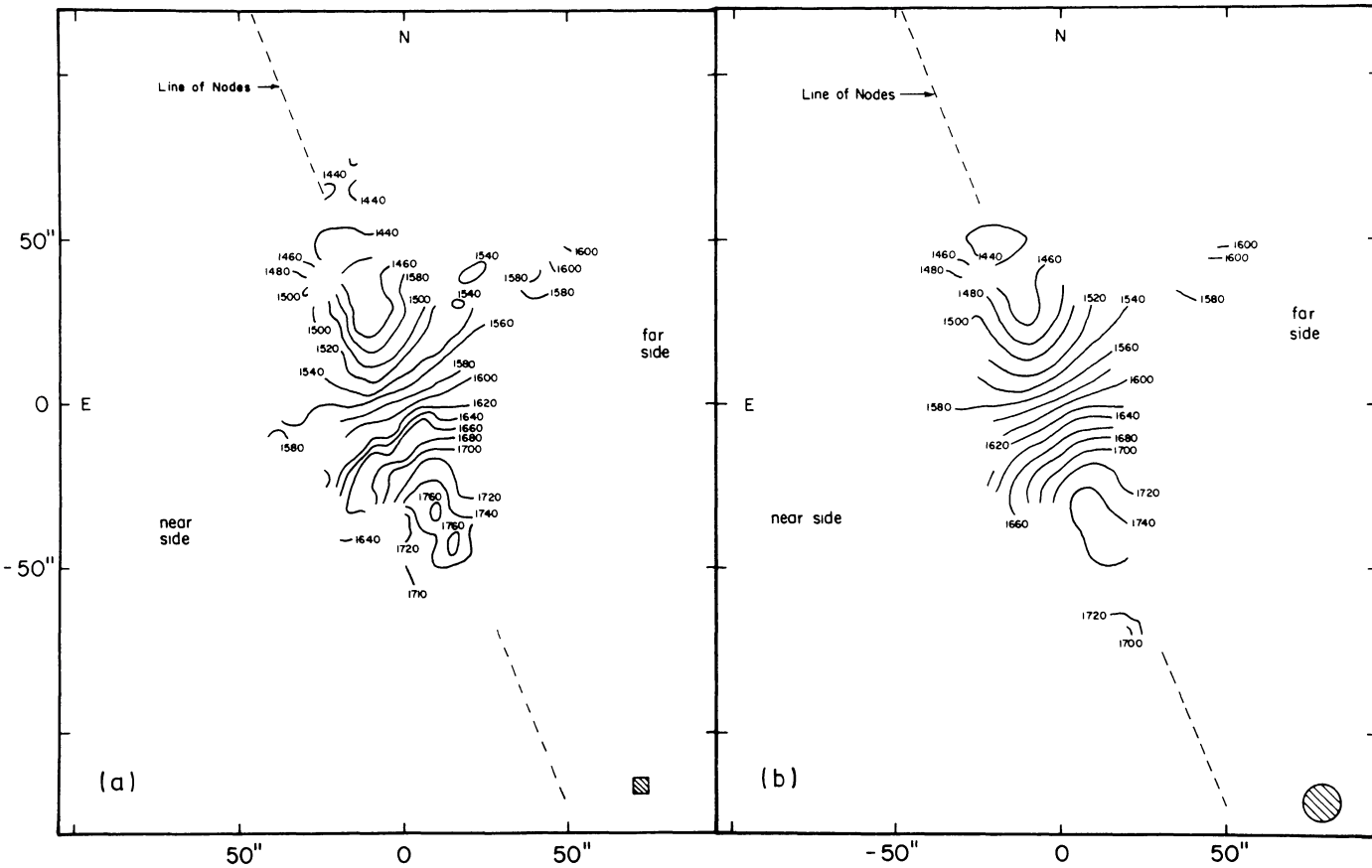


FIG. 14.—Velocity field of NGC 7531 (a) for 5'' \times 5'' resolution elements and (b) after 3 \times 3 Gaussian smoothing

BUTA

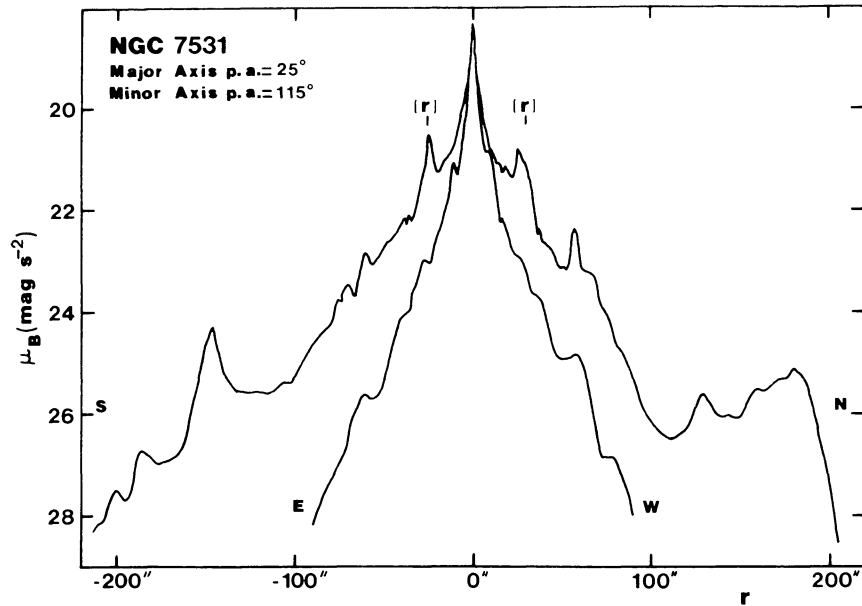


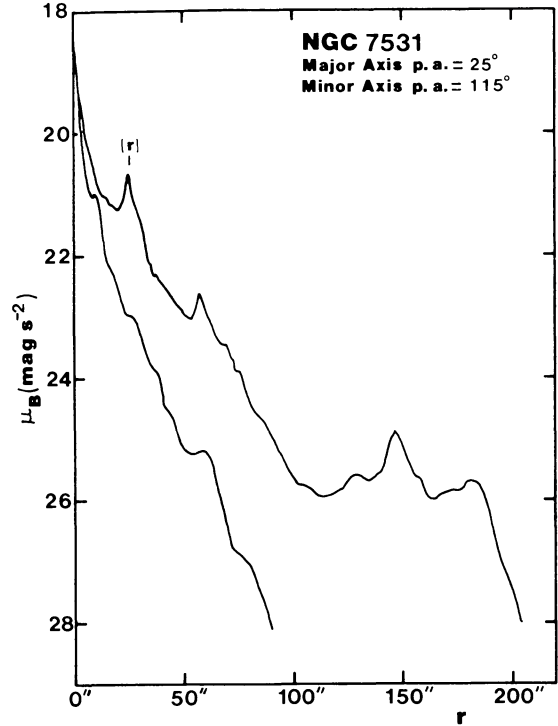
FIG. 15.—Unfolded luminosity profiles of NGC 7531 along the major and minor axes in blue light, based on CTIO plates 5297 and 5308

The method of Warner, Wright, and Baldwin (1973) was used to derive the spatial orientation from the velocities under the assumption that the motion in the plane is predominantly circular. This approach, which is iterative in nature, yielded a best-fitting inclination of $66^\circ \pm 2^\circ$ and a line-of-nodes position angle (approaching half) of $22^\circ \pm 1^\circ$. These values are in good agreement with the photometrically determined ones, but the difference between the line-of-nodes estimates is nevertheless significant. Some slight noncircular motions in the inner regions could account for it, but this is difficult to assess lacking the velocity field in the outer arms.

The distance to NGC 7531 is provided by the five estimates in Table 6. The luminosity index is based on luminosity class estimates from the *Southern Galaxy Catalogue* (Corwin, de Vaucouleurs, and de Vaucouleurs 1985, hereafter SGC) and the *Revised Shapley-Ames Catalogue* (Sandage and Tammann 1981, hereafter RSA). The RSA estimate was reduced to the RC2 system using a conversion formula given in Paper II. The methods are in fair agreement, and a weighted mean gives a distance of $\Delta = 17.1 \pm 1.8$ Mpc. Thus $1'' = 83$ pc. The apparent diameter of the inner ring is $0.94'$, implying a true diameter of 4.6 kpc. Within the intrinsic dispersion this is typical of the size found on average for SA or SAB inner rings by Buta and de Vaucouleurs (1982). It is about 2.5 times smaller than the inner ring of NGC 1433.

b) Interpretation of the Luminosity and Color Data

The unfolded and folded major- and minor-axis luminosity profiles of NGC 7531 are illustrated in Figures 15 and 16 respectively. These are based on *B* plates 5297 and 5308, since the precision of the *B*-band surface photometry is better at the larger radii than in any of the other passbands. Along the major axis the profile is complicated and is interrupted by “peaks” at the inner ring ($r = 28''$), an intermediate zone ($r \approx 60''$), and the outer arms ($r \approx 150''$). The inner-ring

FIG. 16.—Folded *B*-band luminosity profiles of NGC 7531 along the major and minor axes.

peaks are quite conspicuous, the surface brightness attained being $\mu_B = 20.55$ on the south side and $\mu_B = 20.80$ on the north side. These values are 3.5–4.5 times the night-sky brightness, and are considerably brighter than the inner-ring peak surface brightness observed in NGC 1433 ($\mu_B \approx 22.3$ –23.0). The second peak in Figures 15 and 16 at $r \approx 60''$

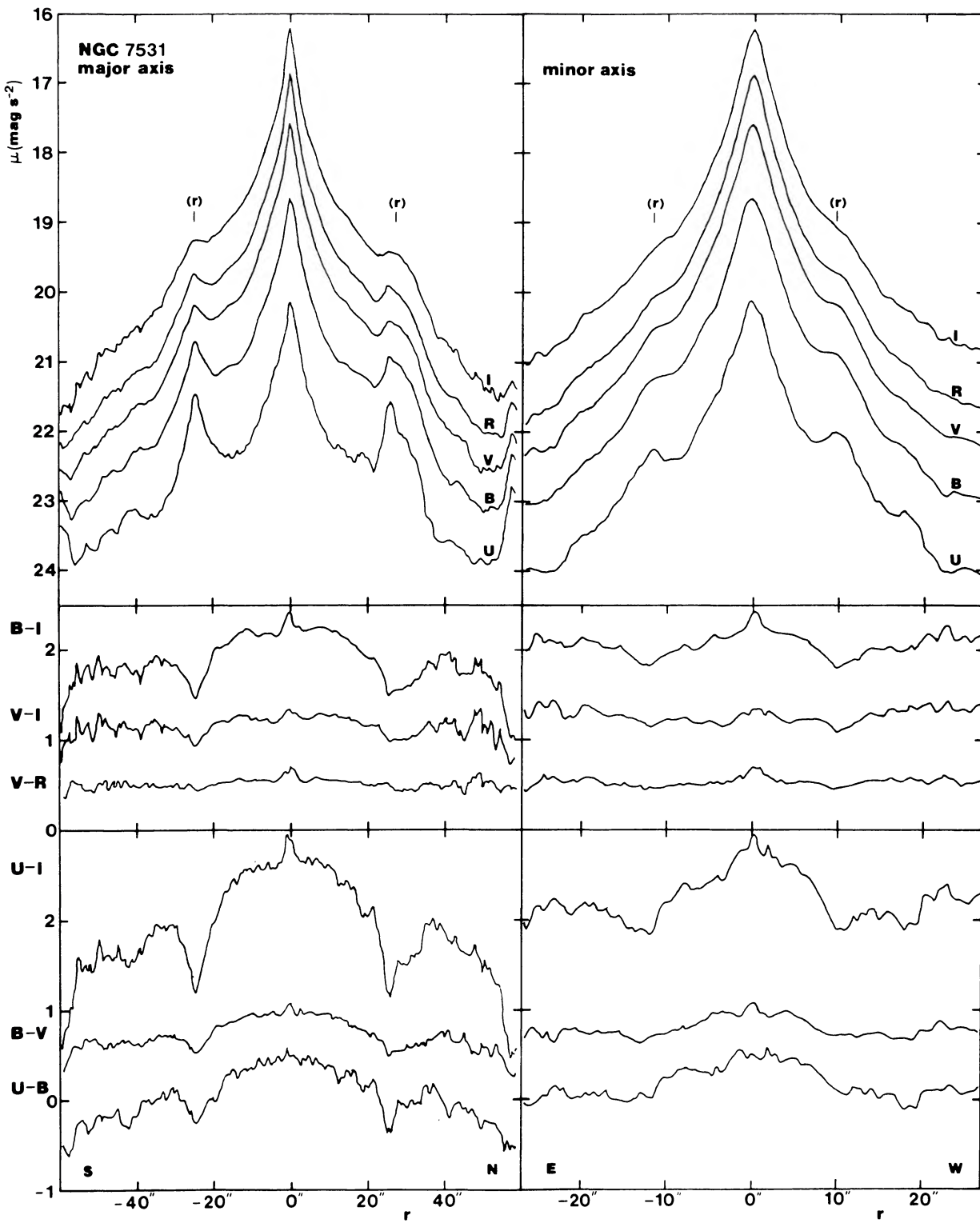


FIG. 17.—Observed surface brightness and color-index profiles along the major and minor axes of the inner regions of NGC 7531, in all passbands. The B , V , R , and I profiles are average profiles from two CCD frames each, while the U profiles are from CTIO plate 5358. The U profiles are displaced by +1 mag for clarity.

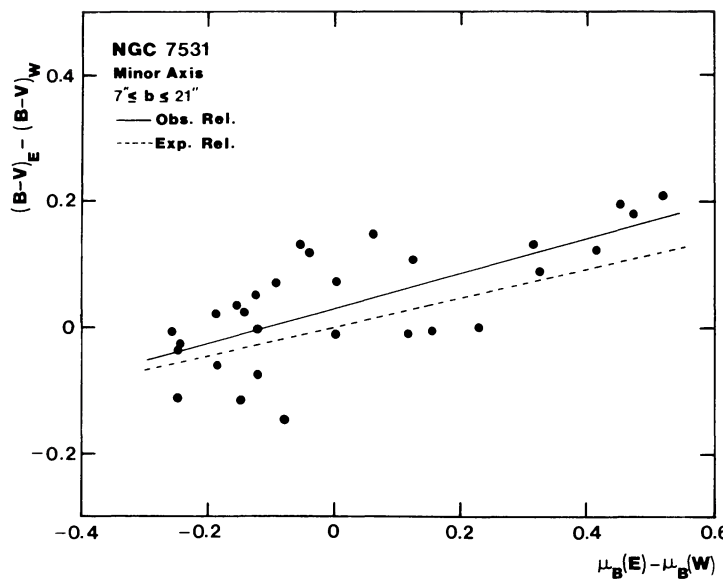


FIG. 18.—A color–surface brightness asymmetry plot for NGC 7531 in blue light, demonstrating that the east side is the near side

is due to two zones of star formation that are symmetrically placed with respect to the nucleus, but which are not necessarily part of a second ring. The outer arms are of very low surface brightness and are seen to dominate the major-axis luminosity profile for $\mu_B > 25.0$ mag arcsec $^{-2}$. On the north side the surface brightness is almost constant in the interval $100'' < r < 200''$.

Along the minor axis the inner ring is still visible as two peaks at $r \approx \pm 10''$, but it is much less conspicuous than along the major axis, presumably in part because of the larger relative contribution of the spheroid compared to the major axis. Beyond the inner-ring peaks the profile indicates that the specific intensities decrease nearly exponentially except for modulation by the spiral structure.

Figure 17 illustrates the major- and minor-axis surface brightness and color profiles for the inner regions only. For B , V , R , and I , these are based entirely on the CCD frames, while the U profile is based on CTIO plate 5358. The seeing is better on B plates 5308 and 5297, so the ring peaks have slightly smaller amplitudes in Figure 17 than in Figures 15 and 16. The major-axis profiles show that the relative amplitude of the inner-ring peaks increases substantially from I to U , as expected, since the ring is very blue. Of interest is how the inner ring still produces a visible bump in the I band along both axes (compare with Fig. 9 in Paper II). Large radial gradients are found in the color indices, especially those involving the U band. The ring itself corresponds to “dips” in the color profiles due to the crossing of young associations. The colors just outside the ring are nearly uniform at the values $B - V = 0.60$, $U - B = 0.00$, but are modulated by additional dips near $r = 60''$ associated with the intermediate zone. Similar color profiles were found for NGC 4736 by Simkin (1967) and in Paper II for NGC 1433.

The color profiles along the minor axis show a slight asymmetry between the east and west sides. If a thin layer of dust is present in a galaxy whose surface brightness distribu-

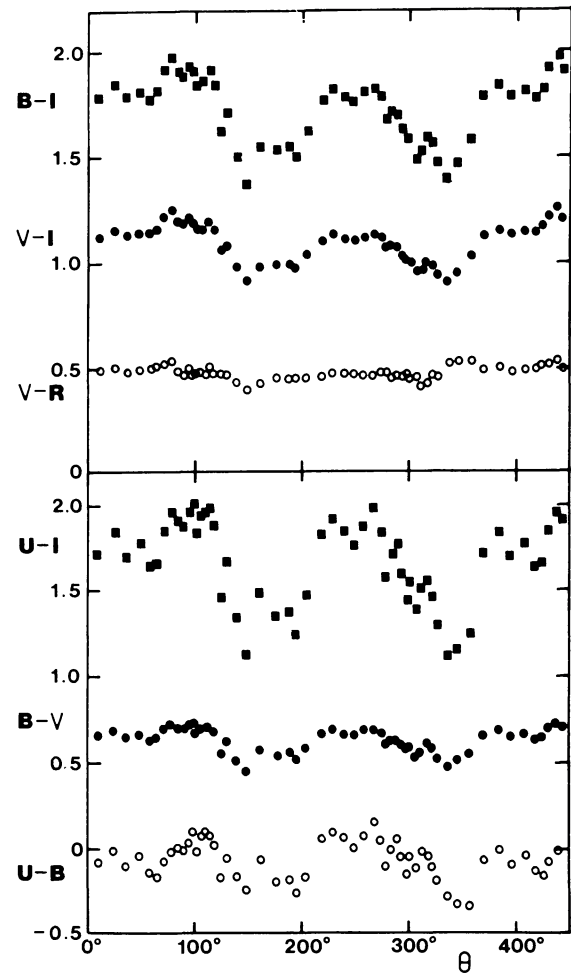


FIG. 19.—Azimuthal color-index profiles along the ridgeline of the inner ring of NGC 7531. These show that the ring is bluest in those regions close to the major axis (in the galaxy plane).

tion depends only on radius, then in an inclined system the near, reddened side should be fainter than the far, less reddened side (Lindblad 1941). To test whether the observed asymmetry in NGC 7531 is due to absorption, Figure 18 shows a plot of the B -band surface brightness difference, $\Delta B = \mu_B(E) - \mu_B(W)$, versus the color-index asymmetry, $\Delta(B-V) = (B-V)_E - (B-V)_W$. The plot shows the kind of correlation predicted by Lindblad. Also shown on the plot is the expected relation for a normal reddening law having a ratio of total-to-selective extinction of $R = 3.4$, which is seen to be a reasonable representation of the observed trend. This analysis confirms that the east side of the galaxy is preferentially obscured relative to the west side, and hence that the east side is the near side. Together with the kinematic data, this also implies that the spiral arms are trailing.

The azimuthal variations of apparent colors along the ridgeline of the inner ring are shown in Figure 19. A cursor was used with a TV display unit to select 47 points along the

ridgeline, and colors were obtained by integrating the flux within a circular aperture $3''$ in diameter. Table 7 lists the colors, and Figure 19 shows the colors plotted against the angle θ in the galaxy plane. (This angle increases counter-clockwise from the line of nodes.) The ring is substantially bluer along its (deprojected) major axis than along its minor axis, even if only the far side is considered. The effect is most striking in those colors involving the U band, and must be due at least in part to a change in the number of luminous young stars. As for NGC 1433, this may mean that compression is not uniform around the ring. The major-axis zones are also the regions where discrete associations in the ring are most prominent, and where the $H\alpha$ intensity is greatest (§ IIIb).

The UBV colors in Figure 19 can give us some information on the age and level of star formation which have characterized the ring. The data in Table 7 are plotted in Figure 20 after correction for Galactic extinction, inclination, and

TABLE 7
RIDGELINE COLORS OF THE INNER RING

r (")	p. a. (1950)	θ	μ_B (mag s $^{-2}$)	U-B	B-V	V-R	V-I	B-I	U-I
23.6	174.05	125.7	20.99	-0.16	0.56	0.48	1.06	1.62	1.46
25.5	179.3	131.2	21.08	0.04	0.63	0.47	1.08	1.71	1.67
27.2	185.4	139.9	20.82	-0.16	0.52	0.44	0.98	1.50	1.34
26.6	190.9	149.4	20.52	-0.24	0.46	0.40	0.92	1.37	1.13
25.9	197.0	161.6	20.79	-0.06	0.57	0.43	0.98	1.55	1.49
24.5	204.3	178.2	20.79	-0.19	0.54	0.46	0.99	1.54	1.35
22.8	209.2	189.8	20.81	-0.18	0.56	0.45	0.99	1.55	1.37
21.1	211.9	195.9	20.70	-0.26	0.52	0.46	0.98	1.50	1.24
19.8	216.2	205.0	20.86	-0.16	0.59	0.46	1.03	1.62	1.46
16.8	224.3	219.7	20.98	0.06	0.67	0.47	1.10	1.76	1.82
14.5	231.3	229.5	20.93	0.10	0.70	0.48	1.12	1.82	1.92
12.9	241.7	240.5	20.88	0.06	0.67	0.48	1.11	1.78	1.84
11.4	253.9	249.8	20.86	0.00	0.66	0.47	1.10	1.76	1.76
10.1	268.9	258.3	20.86	0.07	0.69	0.47	1.11	1.80	1.87
9.7	289.6	267.7	20.88	0.16	0.69	0.47	1.13	1.82	1.98
11.0	307.5	275.4	20.93	0.05	0.67	0.48	1.11	1.78	1.83
11.7	318.1	280.2	20.78	-0.10	0.61	0.48	1.07	1.68	1.58
13.1	328.5	285.6	20.81	0.00	0.63	0.46	1.08	1.71	1.70
14.9	336.5	290.5	20.78	0.06	0.63	0.47	1.07	1.70	1.76
16.4	342.3	294.6	20.68	-0.04	0.61	0.46	1.02	1.63	1.59
17.5	348.3	299.5	20.56	-0.14	0.58	0.47	1.00	1.58	1.44
19.9	351.0	302.0	20.65	-0.04	0.59	0.46	1.00	1.59	1.54
21.7	356.8	308.3	20.48	-0.11	0.54	0.46	0.95	1.49	1.38
24.1	0.5	312.9	20.61	-0.02	0.56	0.41	0.97	1.53	1.50
26.2	4.7	318.8	20.84	-0.05	0.61	0.43	0.99	1.59	1.55
27.9	7.4	323.1	20.88	-0.11	0.59	0.47	0.98	1.57	1.46
29.1	10.0	327.6	20.79	-0.19	0.53	0.46	0.95	1.47	1.29
28.7	15.2	337.7	20.64	-0.29	0.48	0.52	0.92	1.40	1.11
27.3	19.3	346.8	20.76	-0.32	0.52	0.53	0.95	1.47	1.15
25.6	24.3	358.4	20.99	-0.34	0.56	0.53	1.02	1.58	1.24
24.6	29.4	10.4	21.25	-0.07	0.66	0.49	1.12	1.78	1.71
23.0	36.3	25.4	21.32	-0.01	0.69	0.50	1.15	1.84	1.83
20.4	42.3	36.3	21.36	-0.10	0.66	0.48	1.13	1.79	1.69
18.4	50.8	48.8	21.41	-0.04	0.67	0.49	1.14	1.81	1.77
16.5	60.2	59.1	21.34	-0.14	0.63	0.50	1.14	1.77	1.63
15.1	67.6	65.3	21.35	-0.16	0.65	0.51	1.16	1.82	1.65
13.4	75.9	71.1	21.40	-0.07	0.71	0.52	1.21	1.92	1.84
12.1	88.7	78.2	21.35	-0.02	0.73	0.53	1.24	1.97	1.95
11.9	102.9	84.8	21.33	0.00	0.71	0.49	1.20	1.90	1.91
12.3	114.7	89.9	21.35	-0.01	0.70	0.47	1.19	1.88	1.88
14.2	127.3	95.3	21.57	0.03	0.71	0.50	1.21	1.92	1.96
15.8	136.8	99.6	21.60	0.09	0.72	0.47	1.19	1.91	2.00
18.1	143.0	102.7	21.66	-0.01	0.68	0.48	1.16	1.84	1.83
19.9	151.5	107.3	21.68	0.07	0.71	0.49	1.16	1.87	1.94
21.1	157.5	111.2	21.62	0.10	0.70	0.49	1.16	1.86	1.96
22.0	162.5	114.7	21.58	0.07	0.71	0.51	1.19	1.90	1.98
23.6	167.3	118.6	21.50	0.03	0.69	0.48	1.16	1.84	1.88

^aBased on integrations within a $3''$ aperture using CCD frames and CTIO plate 5358.

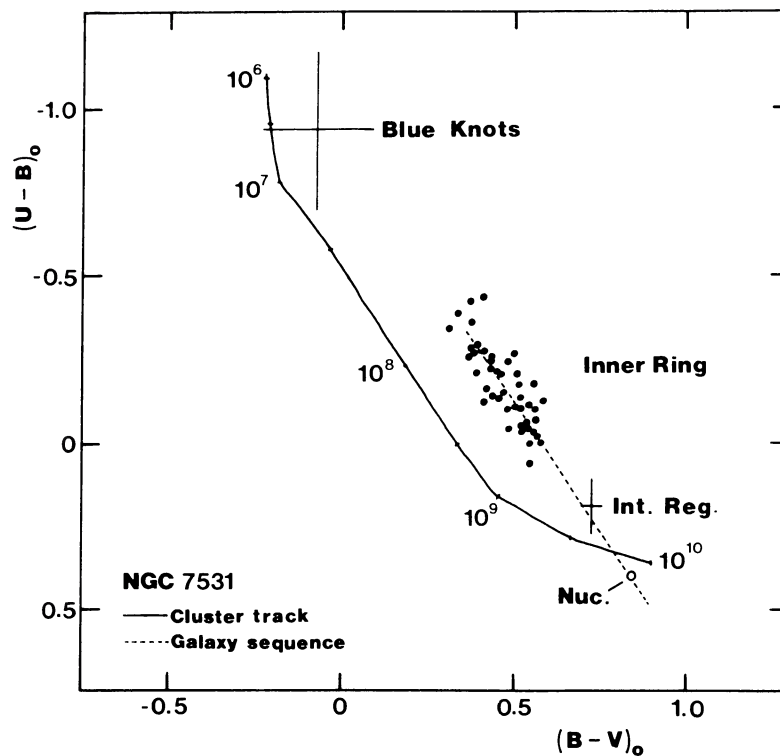


FIG. 20.—Color-color diagrams for selected features in NGC 7531. The labeled curve shows a theoretical evolving “cluster” track from Searle, Sargent, and Bagnuolo (1973) (labels in years), while the nearly straight line shows the observed color-color sequence for the integrated light of galaxies of all types from de Vaucouleurs (1977). The NGC 7531 points have been corrected for Galactic extinction, inclination, and redshift according to RC2 procedures.

redshift according to precepts outlined in RC2. The corrections amount to $E(B-V) = 0.14$ and $E(U-B) = 0.10$. Also shown are the positions of the nucleus, the region between the ring and the nucleus, and the mean of several blue knots in the outer arms. The larger solid curve represents a theoretical aging “cluster” track from Searle, Sargent, and Bagnuolo (1973), while the shorter, nearly linear curve represents the mean normal galaxy sequence from de Vaucouleurs (1977). As for NGC 1433, colors in the ring of NGC 7531 follow very closely the same sequence occupied by the integrated colors of *normal* galaxies in the type range Sbc–Im. This suggests that the ring is not a zone where star formation occurred in a single “burst” at some recent epoch (that is, the ring is not a feature which formed much less than 5×10^8 years ago), but rather it is a place where star formation has occurred at an enhanced rate continuously, for most of the lifetime of the galaxy (see also Larson and Tinsley 1978). That the ring is still prominent in the near-infrared suggests that an “old ring” has developed at the same position as the prominent thin, knotty ring visible in blue light (see Fig. 1 and § IVd). The points spread over a wide range of the galaxy sequence because some parts of the ring are influenced by more recent star formation (and more internal extinction) than others.

c) Decomposition of the Luminosity Profiles

The luminosity distribution within NGC 7531 is not readily decomposable into bulge and disk components. The disk is not well defined from the major-axis profile because of the modulation by the inner ring, the intermediate arms, and the

outer arms. These features are less conspicuous along the minor axis, which shows a nearly exponential decline in specific intensities for $r > 20''$. In this section the technique of successive approximations (Kormendy 1977; Tsikoudi 1977; Burstein 1979; Boroson 1981) is applied to the minor-axis profile as a means of deriving the photometric parameters of the disk, the spheroid, and the ring. The analysis is based mainly on the blue-light CTIO plates 5297 and 5308.

Two models are considered: (I) a two-component model consisting of an $r^{1/4}$ spheroid and an exponential disk and (II) a three-component model consisting of an $r^{1/4}$ spheroid, an exponential “blue” disk, and an exponential “red” disk. The need for model II will become clear only after discussion of model I.

i) Two-Component Model

The first model was constructed using the unobscured western half of the *B*-band minor-axis profile and is shown in the left-hand panel of Figure 21. The minima in specific intensity along this axis in regions with $r > 20''$ were used to make initial estimates of the exponential disk effective semi-minor axis radius b_e^{II} and effective surface brightness μ_e^{II} , the assumption being made that these regions are not seriously affected by spiral structure. The derived disk light was then subtracted from the profile; for radii $2'' \leq r \leq 6''.5$, a well-defined $r^{1/4}$ dependence was found and a solution could be made for the spheroid (giving parameters b_e^{I} and μ_e^{I}). The parameters of both the disk and the spheroid were iterated several times until a satisfactory (seeing-uncorrected) pre-

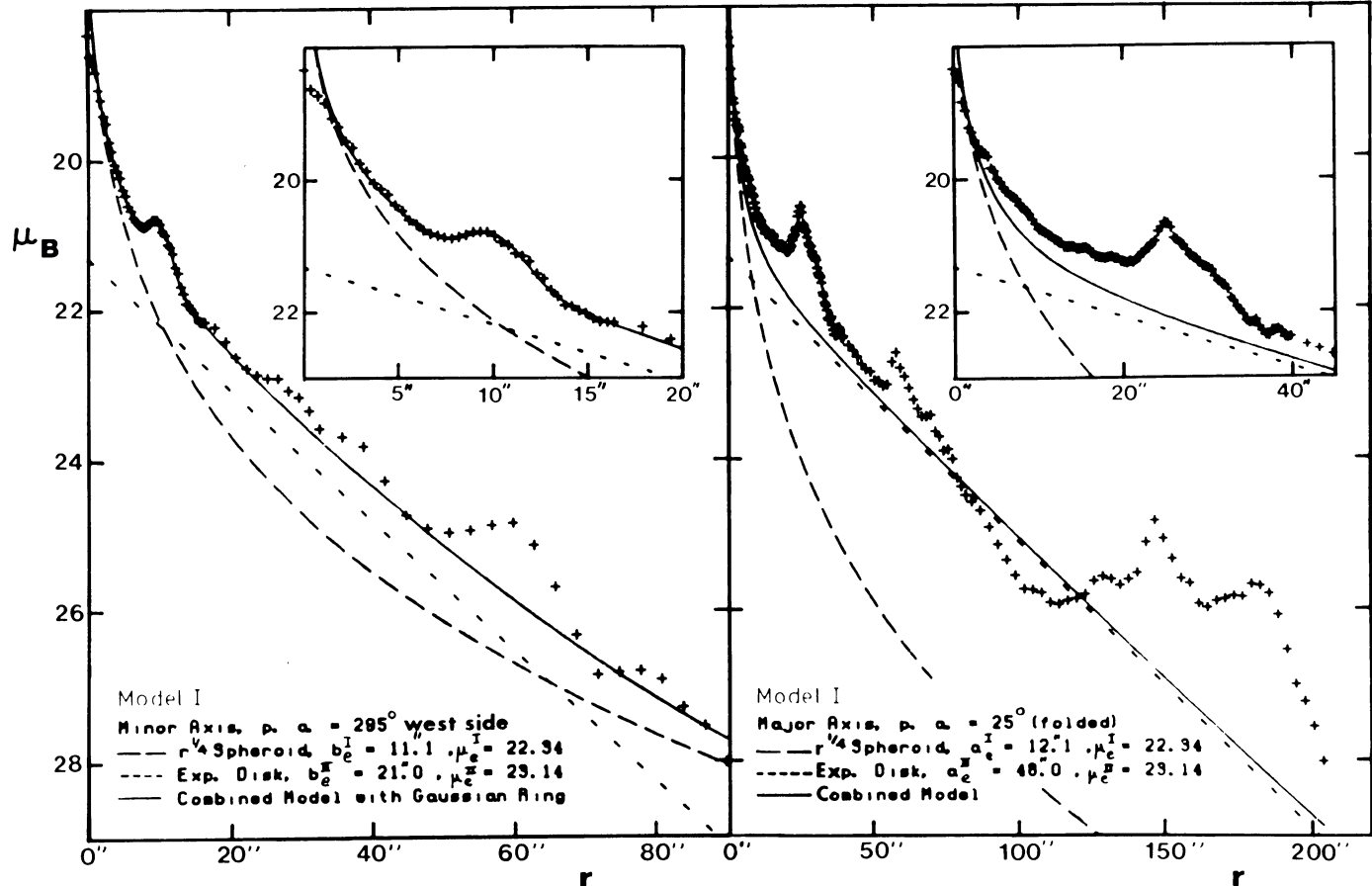


FIG. 21.—Two-component model (model I) of the light distribution within NGC 7531 including an $r^{1/4}$ spheroid and exponential disk: (a) western half of minor axis; (b) major axis. The inner ring along the minor axis has been modeled with a Gaussian. The model is based on the method of successive approximations as applied to the minor-axis profile only, and is projected to the major axis in (b). The model is not satisfactory because of excess light interior to the ring which is not accounted for by the model.

liminary solution was obtained. The surface brightnesses in the region $r < 2''$ were found to depart systematically from the combined model toward lower than predicted specific intensities, presumably largely because of seeing. To correct for the point-spread function, several stars having central densities near the peak value in the nucleus of the galaxy were scanned separately at high resolution, and their profiles modeled in terms of three Gaussian functions. Then an iterative technique described by Tsikoudi (1977) was used to approximately deconvolve the surface brightnesses for seeing and derive the true parameters of the spheroid. The adopted parameters are summarized in Figure 21.

Once the spheroid and disk parameters were established, the contributions of these components were subtracted from the minor-axis profile to reveal the luminosity profile of the inner ring. A Gaussian fit was found to provide an excellent representation. The dispersion, $\sigma = 1.5'$, is twice the “seeing” disk value of $0.7'$. The inner-ring profile is more complicated in other directions, but these will be considered separately (§ IVd). The inset in the left-hand panel of Figure 21 shows that the model I spheroid, disk, and Gaussian inner ring provide an excellent representation of the minor-axis profile of NGC 7531.

Assuming that the parameters derived from the minor-axis solution are correct, the right-hand panel in Figure 21 shows the predicted combined B -band model profiles as projected to the major axis. The major-axis effective radius of the disk was obtained using an inclination of 65° and assuming that the intrinsic flattening of the component is $q_t^{\text{II}} = 0.10$, consistent with the flattest galaxies in RC2. The major-axis effective radius of the spheroid was obtained assuming $q_t^{\text{I}} = 0.9$, consistent with the nearly round isophotes observed in the bulge. The resulting combined model profile is seen to be a reasonable representation of the general decline in specific intensity for radii $r > 50''$, but the inset in the right-hand panel of Figure 21 shows that there is considerable excess light interior to the ring peak which is not accounted for by the model. This indicates that model I is an inadequate representation of the light distribution within NGC 7531.

ii) Three-Component Model

The excess residual light interior to the ring along the major axis is so significant that it is probable that the model I spheroid parameters are in error. In this section a self-consistent combination of a spheroid and disk will be derived

that will include the contribution of a third component mostly confined inside the inner ring of NGC 7531.

The form of the third-component was derived as follows. First, a position angle was chosen that crossed a relatively "clean" (i.e., minimally obscured) part of the interior region and was at the same time relatively close to the major axis of the galaxy. The major axis itself could not be used because the inner dust lanes lie very nearly along that axis. The profile adopted for the analysis was instead chosen along the position angle 223° . Second, the model I parameters of the bulge and disk were subtracted from this profile, and the residual surface brightnesses were plotted against radius (Fig. 22). As for the major-axis profile, excess light was found to be present, and Figure 22 shows that the surface brightness of the excess varies linearly with radius in the zone $3'' \leq r \leq 10''$. Extrapolation of this variation across the large inner-ring hump in this plot suggests that the residual inner-ring light is superposed on an additional component whose specific intensity distribution decreases exponentially with radius. Since the isophotes interior to the ring are at least as elongated as the ring itself, except for the innermost few arcseconds, the additional component is flat like the disk. In the third step of the process, the effective radius and surface brightness of this additional exponential component were derived, and then the contribution of this and the model I disk component were subtracted from the minor-axis profile to reevaluate the parameters of the spheroid. The same approach was used for the U and V passbands in order to deduce the colors of the components. Because the three components in this model are tightly coupled, the effective radii of the bulge and disk solutions were forced to be identical in all three passbands, since any differences are difficult to separate from decoupling errors.

The results of the model are compiled in Table 8 and are illustrated in Figures 23a and 23b for the B band only. The important difference between models I and II is that the spheroidal component for model II contributes only $\sim 13\%$ of the total B -band flux, while for model I it contributes $\sim 23\%$. According to Simien and de Vaucouleurs (1986), the spheroidal components of Sbc galaxies contribute on average $\sim 16\%$ of the total blue light, hence model II is more reasonable in this regard. The model II profiles are also in better agreement with the observed profiles. Although model II yields a solution virtually identical with that of model I in the inner regions along the minor axis, Figure 23b shows that model II fits the outer parts of that profile better because of the decreased relative contribution of the spheroid.

It is of interest that the model indicates the inner disk to be much redder than the outer disk. The outer disk is bluer than those measured by Schweizer (1976) in a number of intermediate- to late-type spirals. The colors of the decoupled components are uncertain in any case, but Figure 24 shows that the model well represents the observed major axis $B - V$ and $U - B$ color profiles. It appears that the color gradients in NGC 7531 can be interpreted well in terms of the combined light of a "red" spheroid, an exponential "red" disk, and an exponential "blue" disk, all having different scale lengths. Although this is only a convenient mathematical representation, the implication is that the "old disk" of NGC 7531 has a color gradient in the inner regions. A similar

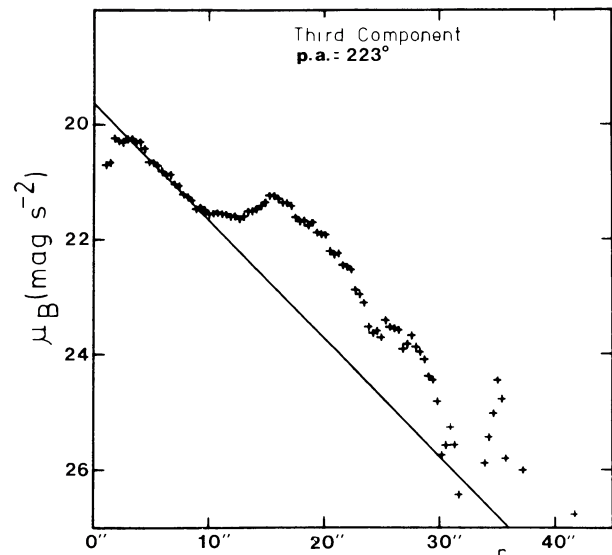


FIG. 22.—A possible additional component in the light distribution of NGC 7531 deduced by using model I as a first approximation to a three-component representation. Interior to the ring this component could be exponential with a scale length smaller than that of the outer disk.

TABLE 8
THREE-COMPONENT PHOTOMETRIC MODEL

Parameter ^a	Spheroid	Disk	Third Component	Inner Ring ^b
$k(U)$	0.08	0.47	0.05:	0.16
$k(B)$	0.13	0.44	0.10	0.15
$k(V)$	0.18	0.40	0.15	0.13
$B - V$	1.06	0.61	1.07:	0.54:
$U - B$	0.56	-0.10	0.88:	-0.03:
$(B - V)_0$...	0.92	0.47	0.93:	0.40:
$(U - B)_0$...	0.46	-0.20	0.78:	-0.13:

^a k = fractional contribution of component relative to total flux.

^bDefined by an elliptical annulus having parameters $18'' \leq a \leq 36''$, axis ratio $q = 0.42$, and position angle 14° .

gradient was found in the spiral galaxy M83 by Jensen, Talbot, and Dufour (1981). These authors argue that possible causes for a radial color gradient in the old disk population might be a systematic variation in the star formation history as a function of radius, a gradient in the mean metallicity of the stars contributing most of the light, or a centrally concentrated distribution of dust. There is much dust evident interior to the ring of NGC 7531 which would contribute to the effect. A radial abundance analysis of the gas would help to evaluate the second possibility.

d) Structure of the Inner Ring

It was shown in § IVc that the residual profile of the inner ring along the minor axis can be accurately represented by a Gaussian function. A casual inspection of profiles in other position angles suggests that such a simple interpretation may not be valid all around the ring; some profiles are asymmetric and more complicated. The ring profiles along other axes can

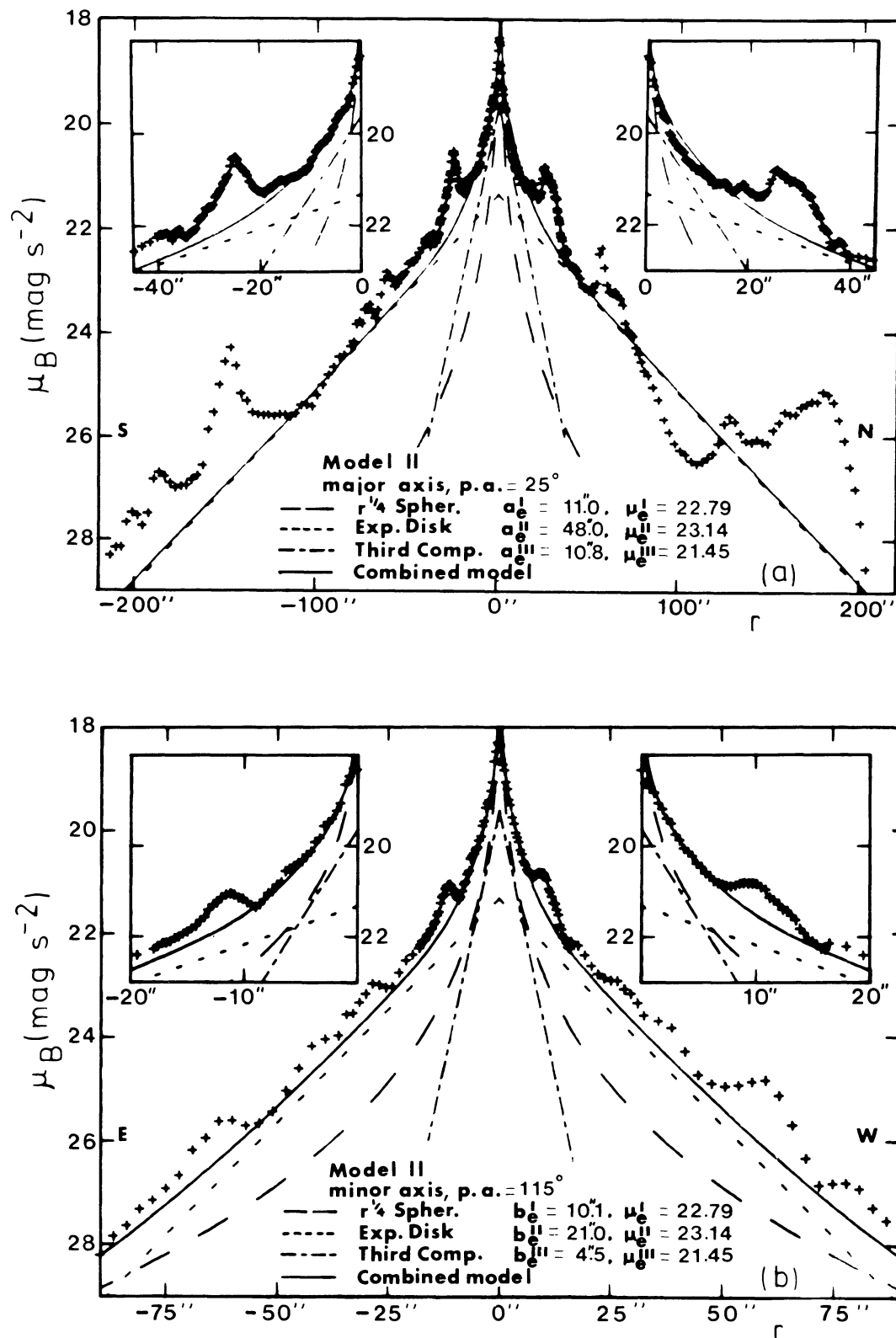


FIG. 23.—Three-component model (model II) of the light distribution of NGC 7531 based on an $r^{1/4}$ spheroid, an exponential “red” disk, and an exponential “blue” disk. Effective parameters of the components are indicated.

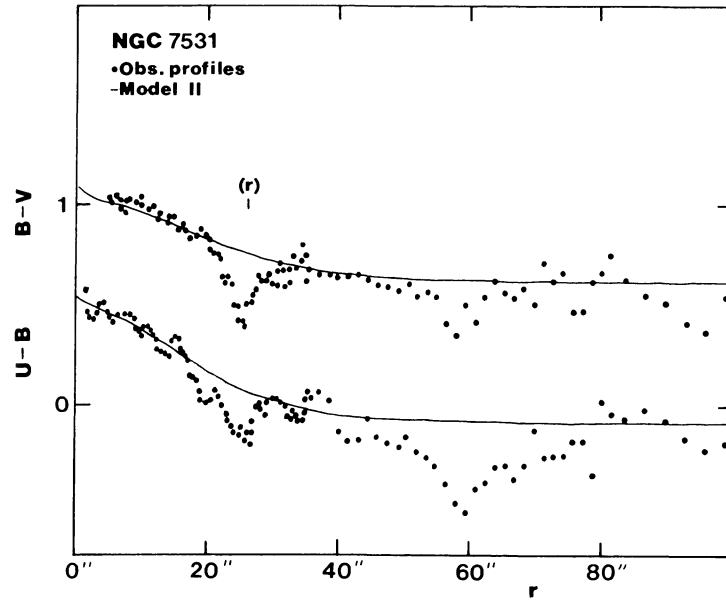


FIG. 24.—Model II predicted color-index profiles along major axis, as compared with observed folded color profiles

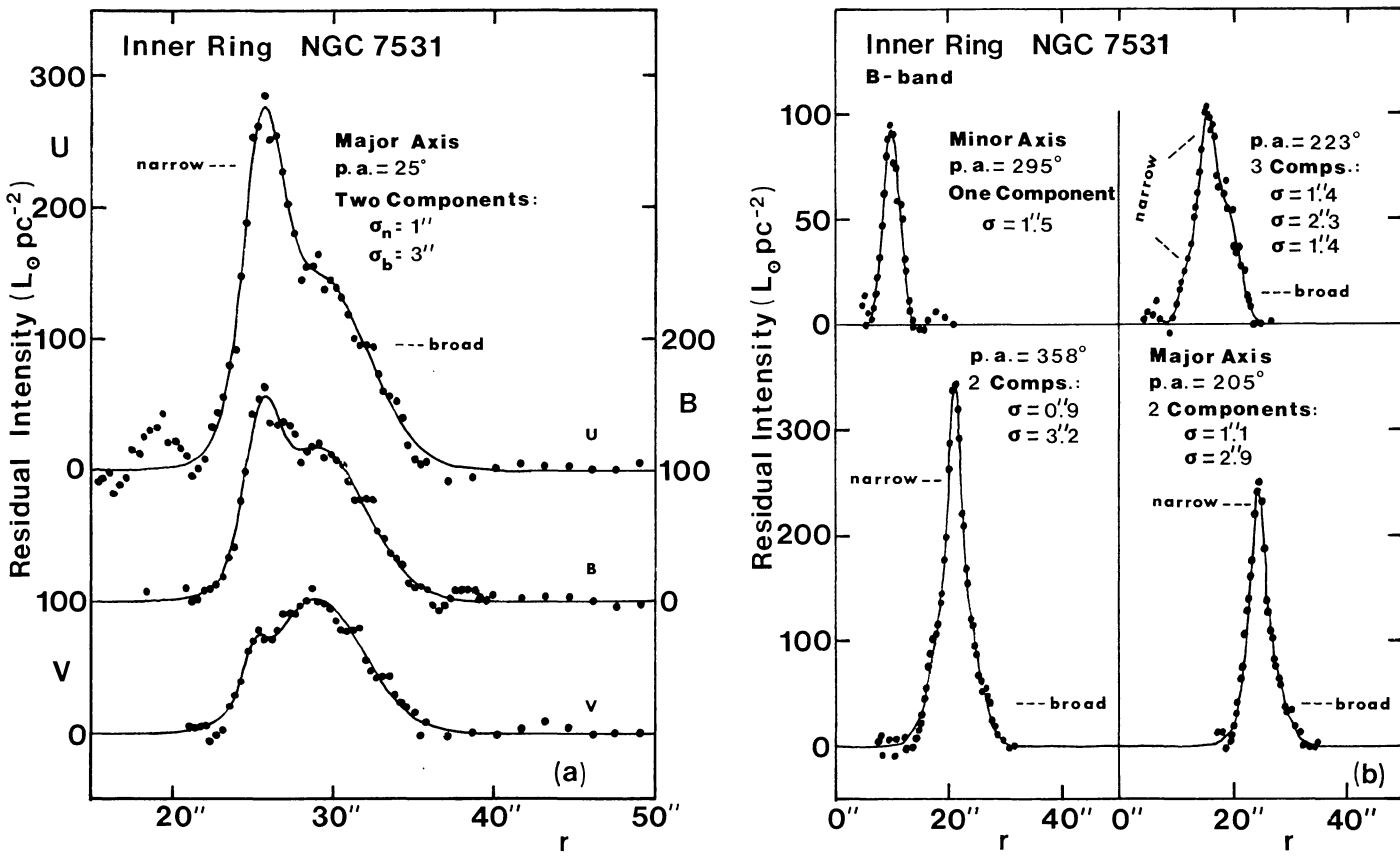


FIG. 25.—(a) Residual UBV profiles of inner ring along north half of major axis, fully corrected for background, showing the two main components of the ring: a broad red component and a very blue narrow component slightly misaligned with the broad one. (b) Residual B -band profiles of the ring in several other position angles. Broad and narrow components are identified in each profile, except for the minor axis, and in the lower panel these components almost exactly overlap.

instead be modeled as the sum of several Gaussians. Figure 25 shows several residual ring profiles which have been fully corrected for "background." These are based on CTIO plates 5308, 5313, and 5358, which have the best seeing. Figure 25a shows that the ring profile on the north side in position angle 25° can be represented in each passband as the sum of two Gaussian components, a narrow one having $\sigma \approx 1''$, and a broad one having $\sigma \approx 3''$. The narrow component is seen to be much more sensitive to the passband than the broad component, and the two have slightly displaced peaks. In Figure 25b two cases are shown in the lower panels where the broad and narrow components virtually exactly overlap, so that the ring profile has "wings." The dispersions of the two components are nearly identical with those for p.a. 25° . The most complicated case considered is in the upper right-hand panel of Figure 25b, where three Gaussians, two narrow and one broad, were needed to represent the profile.

The simplest interpretation of these profiles is that the inner ring of NGC 7531 consists of discrete associations superposed within a slightly diffuse background. The narrow components are either equal to or slightly larger than the seeing disk in each passband, and hence are either unresolved or barely resolved associations. Although the fitted central intensities of the Gaussian components are quite uncertain because of the method of background interpolation, the profiles in Figure 25a definitely indicate that the narrow component is bluer than the broad component. It is clear that the inner ring consists of an older component in addition to the prominent young component that dominates the visual impression on U - and B -band photographs; this is the "old ring" visible in the I -band image (Fig. 1) as a fairly smooth structure. In these respects the ring of NGC 7531 is very similar to that in NGC 1433.

e) Azimuthal Profiles, Arm-Interarm Amplitudes, and a Fourier Analysis of the Light Distribution

Two other approaches to exploring the photometric structure of NGC 7531 are to examine azimuthal profiles in the plane and to carry out a Fourier analysis. In this section I wish to use these techniques to search for the possible presence of a barlike distortion in the disk.

Figure 26 (Plate 6) shows a geometrically deprojected blue-light image of NGC 7531. The deprojection is purely geometric in the sense that pixels in the image have simply been transformed to their positions in the plane assuming an inclination of 65° and a major-axis position angle of 25° , and ignoring the finite thickness of the disk. The surface brightnesses are not precisely correctable for the extinction to the near side, but for the purposes of this discussion I wish only to illustrate with this approach how the intermediate region between the inner ring and outer arms may be intrinsically oval in shape. The image also highlights how the deprojected inner ring may also be slightly oval in shape. The deprojected axis ratio is 0.8, and, if correct, it is more elongated than is typical of SA inner rings (see Paper I).

Figure 27 shows B - and I -band azimuthal profiles in the radius range $40'' \leq r \leq 160''$. These show a roughly sinusoidal 2θ wave pattern across the "intermediate zone" ($r < 110''$) that is fairly significant. For $r \geq 120''$, this pattern is less

significant, while the outer arms, especially the southwest arm in blue light, are quite prominent. Figure 28 shows a color-amplitude plot (Elmegreen and Elmegreen 1984, 1985) of the ovally distorted region (*open circles*) and the southwest arm-interarm regions (*filled circles*). Here $A = I_{\max}/I_{\min}$ is the contrast ratio between the crest of the arm or oval and the interarm or oval minimum. The plot demonstrates that the oval is a stellar density enhancement because $A_B/A_I \sim 1$, but this is not true for the southwest arm points. For these A_B/A_I is fairly large, and using the simple models described by Elmegreen and Elmegreen (1984) the values imply that this arm is comprised of almost pure star formation. If a stellar density wave is present in this galaxy, it is weak compared with those observed in other late-type spirals such as those discussed by Schweizer (1976) and Elmegreen and Elmegreen (1984, 1985). The southwest arm is nevertheless plainly visible in Figure 1b.

The Fourier analysis was carried out by calculating the moments of the light distribution (see Paper II) using the intensity arrays in all passbands deprojected to face-on assuming an inclination of 65° and a major-axis position angle of 25° . Table 9 gives the variation of the $m = 0$ term (converted to surface brightness in mag arcsec $^{-2}$) separately for the photographic and the CCD photometry. Mean profiles, based on an average of the two data sets, are illustrated in Figure 29, while the color profiles these imply are illustrated in Figure 30. The inner ring and outer arms produce prominent bumps especially in the U and B profiles. The color gradients in the regions well beyond the inner ring can be explored more precisely with these profiles, and at least $B - V$, $U - B$, and $U - I$ imply that the region occupied by the outer arms ($r > 100''$) is very blue.

The first six Fourier amplitudes are plotted as a function of radius for the B and I passbands separately in Figure 31. However, these include one refinement which the azimuthally averaged profiles illustrated in Figures 29 and 30 do not: the spherical shape of the bulge has been allowed for in calculating the moments in order to correct for the false $m = 2$ Fourier terms that would arise by neglecting this shape. The bulge model from § IVd was used for this purpose, assuming $B - I = 2.31$. The procedure was as follows: first, the bulge model was subtracted from the two-dimensional intensity arrays; second, the moments of the residual light (assumed to lie purely in a thin disk) were calculated; last, the relative Fourier amplitudes (i.e., I_m/I_0) were computed by adding back the contribution of the bulge to the azimuthally averaged intensities I_0 . The resulting amplitudes show a dominant $m = 2$ component over the inner disk ($r < 100''$), and much smaller odd and higher even terms. These help to quantify the properties of the possible oval distortion somewhat better than Figures 27 and 28, and it is interesting to compare the amplitudes with those shown for NGC 1433 (Paper II, Fig. 18). The phases of the even Fourier terms provide further information on this possible distortion. Figure 32 shows that the phase of the dominant $m = 2$ component changes gradually from $\sim 140^\circ$ at the mean radius ($r = 28''$) of the inner ring to $\sim 100^\circ$ at the apparent optical edge ($r = 84''$) of the "intermediate zone" visible in Figure 1. If the significance of the $m = 2$ component in both passbands is due purely to

PLATE 6

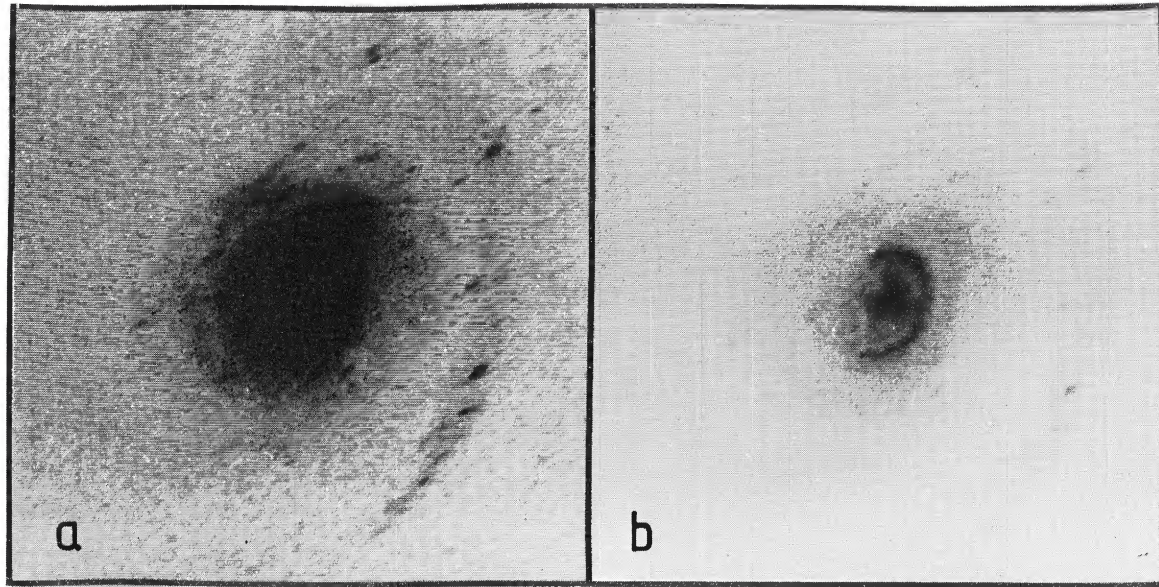


FIG. 26.—Geometrically deprojected image of NGC 7531 in blue light. The bulge has been treated as spherical using the model II parameters, and so has not been stretched by the deprojection.

BUTA (*see* page 21)

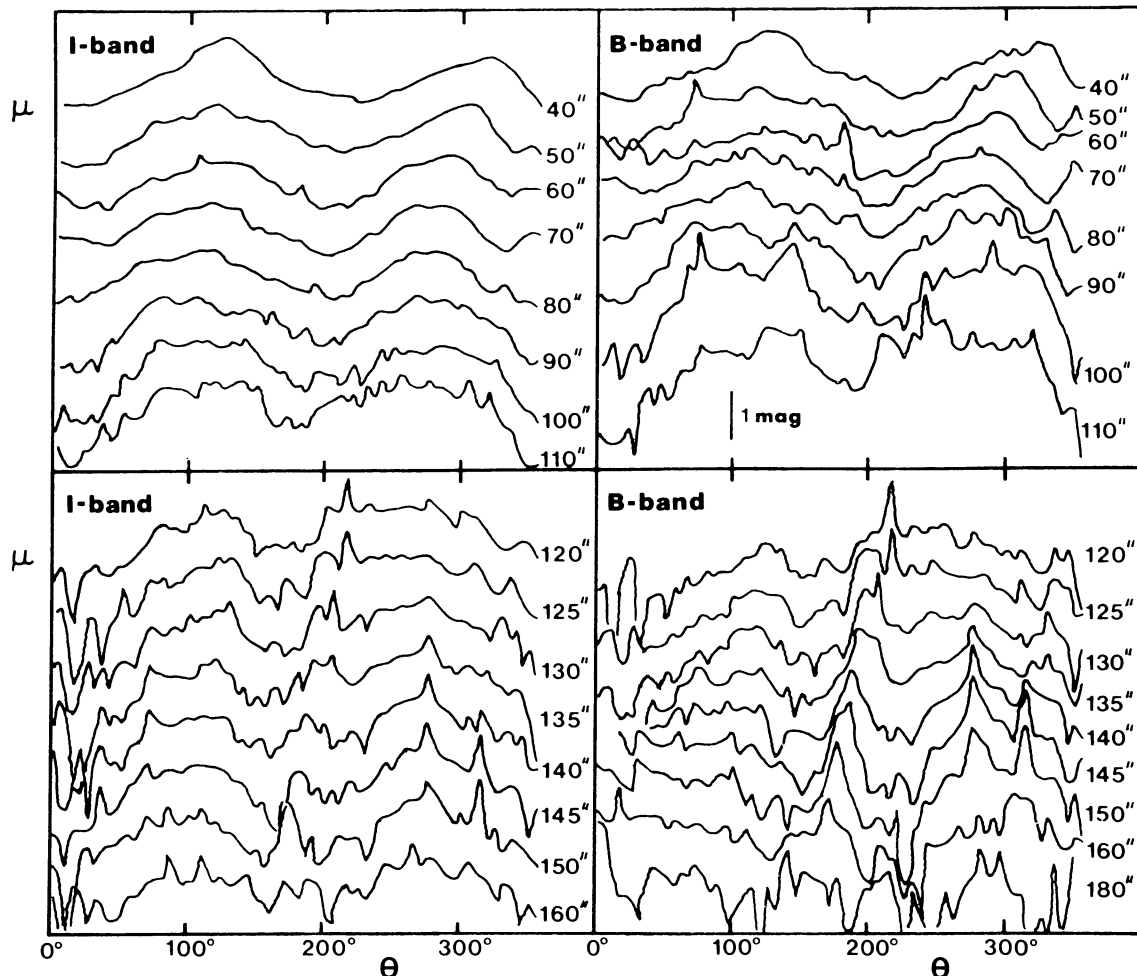


FIG. 27.—Azimuthal surface brightness profiles in the blue and near-infrared. The mean radius of each is indicated. These are profiles taken along circles in the plane of the galaxy assuming an inclination of 65° and major-axis position angle 25° . The sinusoidal pattern suggests that the intermediate zone could be ovaly distorted. This pattern dominates interior to $r = 100''$, while outside this radius the outer arms produce conspicuous peaks.

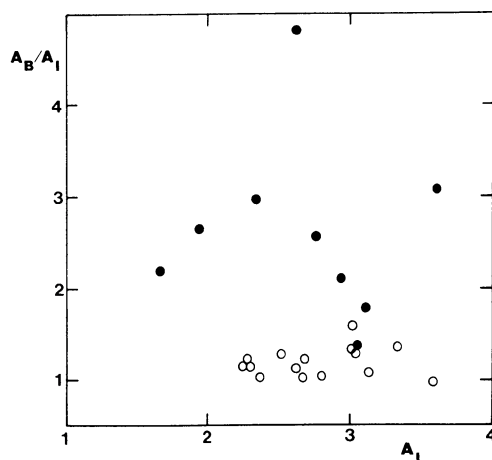


FIG. 28.—Color-amplitude plot of the arms (filled circles) and possible oval distortion (open circles) in NGC 7531. These are the relative contrast ratios in blue and near-infrared light as compared with the ratio in near-infrared light.

uncertainty in the inclination, then these false Fourier terms ought to have phases near 90° or 0° . The indication is that the oval distortion in NGC 7531 is being viewed nearly end-on. If true, this is an unfavorable orientation for detecting noncircular motions in the gas flow due to the influence of the distortion (see, for example, Kalnajs 1978), which may in part explain why the velocity field appears to be fairly regular.

In the outer disk ($r > 100''$), the odd terms are clearly significant in the B band and reflect the asymmetry of the outer arms. The terms seem less significant but are still apparent in the I band. The maximum amplitude of the $m = 1$ component occurs at $r \approx 120''$ and coincides with the bright association visible in the southwest arm in Figure 1.

f) Rotation Curve and Mass

The rotation curve of NGC 7531 is shown in Figure 33. For the sake of homogeneity this is based on the slit spectroscopy alone, since the spectra cover the largest range in radius with the most precision. The TAURUS data are mainly confined

TABLE 9A

AZIMUTHALLY AVERAGED PHOTOGRAPHIC SURFACE PHOTOMETRY^a

r	μ_B	U-B	B-V	V-R	V-I	μ_{BJ}	r	μ_B	U-B	B-V	V-R	V-I	μ_{BJ}
0	18.34	0.69	•••	•••	•••	•••	49	22.62	0.01	0.67	0.53	1.21	22.63
1	18.57	0.71	•••	•••	•••	•••	50	22.68	0.01	0.68	0.53	1.21	22.69
2	18.94	0.57	•••	•••	•••	•••	51	22.73	0.00	0.68	0.53	1.20	22.73
3	19.21	0.52	•••	•••	•••	•••	52	22.78	0.00	0.67	0.53	1.22	22.78
4	19.43	0.49	0.88	0.63	•••	•••	53	22.82	-0.01	0.67	0.53	1.23	22.83
5	19.63	0.49	0.91	0.58	•••	•••	54	22.86	-0.05	0.67	0.52	1.21	22.87
6	19.81	0.48	0.53	0.56	•••	•••	55	22.90	-0.15	0.67	0.52	1.21	22.91
7	19.96	0.45	0.92	0.59	•••	•••	56	22.94	-0.06	0.66	0.67	1.21	22.95
8	20.09	0.45	0.93	0.58	•••	•••	57	22.98	-0.05	0.67	0.53	1.19	22.98
9	20.21	0.43	0.94	0.53	•••	•••	58	23.00	-0.06	0.66	0.52	1.17	23.00
10	20.37	0.41	0.95	0.53	1.20	•••	59	23.04	-0.07	0.66	0.52	1.16	23.04
11	20.48	0.40	0.91	0.54	1.24	•••	60	23.07	-0.06	0.65	0.53	1.17	23.06
12	20.59	0.38	0.94	0.50	1.22	•••	61	23.13	-0.07	0.66	0.52	1.19	23.12
13	20.65	0.38	0.92	0.49	1.20	•••	65	23.29	0.13	0.67	0.53	1.14	23.32
14	20.71	0.36	0.91	0.48	1.19	•••	69	23.40	0.03	0.64	0.52	1.13	23.43
15	20.76	0.35	0.88	0.48	1.19	•••	73	23.55	-0.03	0.63	0.52	1.14	23.57
16	20.82	0.32	0.87	0.46	1.19	•••	77	23.74	-0.03	0.63	0.51	1.15	23.75
17	20.88	0.27	0.85	0.48	1.19	•••	81	23.93	-0.03	0.62	0.52	1.13	23.94
18	20.91	0.23	0.83	0.48	1.18	•••	85	24.13	-0.09	0.63	0.53	1.12	24.15
19	20.94	0.19	0.81	0.48	1.17	•••	89	24.27	-0.09	0.59	0.53	1.14	24.28
20	20.98	0.16	0.80	0.47	1.17	•••	93	24.42	-0.14	0.58	0.54	1.13	24.42
21	21.00	0.13	0.77	0.49	1.18	•••	97	24.54	-0.17	0.54	0.60	1.13	24.52
22	21.01	0.10	0.75	0.49	1.16	21.02	101	24.73	-0.23	0.57	0.57	1.15	24.71
23	21.00	0.10	0.72	0.50	1.15	21.01	105	24.88	-0.12	0.55	0.59	1.11	24.88
24	20.99	0.08	0.69	0.49	1.14	21.01	109	24.97	-0.28	0.55	0.53	1.22	25.00
25	20.99	0.07	0.67	0.49	1.13	21.01	113	25.03	-0.32	0.51	0.62	1.16	24.98
26	21.02	0.05	0.66	0.49	1.12	21.03	117	25.01	-0.36	0.45	0.60	1.12	24.95
27	21.06	0.03	0.65	0.50	1.12	21.07	121	21.92	-0.44	0.40	0.59	1.12	24.78
28	21.10	0.01	0.64	0.50	1.11	21.10	125	25.04	-0.44	0.41	0.67	1.17	24.95
29	21.13	0.00	0.62	0.50	1.10	21.14	129	25.23	-0.40	0.44	0.63	1.14	25.18
30	21.19	-0.01	0.61	0.51	1.11	21.20	133	25.33	-0.36	0.44	0.55	1.18	25.32
31	21.28	-0.01	0.63	0.51	1.11	21.29	137	25.39	-0.42	0.45	0.59	1.14	25.37
32	21.37	-0.01	0.64	0.51	1.12	21.37	141	25.38	-0.38	0.44	0.53	1.15	25.32
33	21.46	-0.01	0.64	0.51	1.14	21.47	145	25.36	-0.41	0.41	0.55	1.14	25.22
34	21.57	0.00	0.65	0.51	1.15	21.58	149	25.44	-0.34	0.44	0.59	1.07	25.32
35	21.68	0.02	0.67	0.51	1.16	21.68	153	25.60	-0.42	0.39	0.58	1.04	25.56
36	21.77	0.03	0.68	0.50	1.17	21.77	157	25.74	-0.40	0.38	0.64	1.20	25.76
37	21.85	0.05	0.68	0.51	1.18	21.86	161	25.93	-0.43	0.44	0.65	1.17	25.93
38	21.95	0.05	0.68	0.51	1.18	21.96	165	26.04	-0.43	0.44	0.82	1.24	26.00
39	22.03	0.05	0.68	0.51	1.20	22.04	169	26.12	-0.34	0.40	0.68	1.07	26.14
40	22.10	0.06	0.68	0.51	1.21	22.12	173	26.32	-0.39	0.45	0.57	1.02	26.46
41	22.17	0.06	0.69	0.52	1.20	22.19	177	26.39	-0.12	0.33	0.72	1.01	26.49
42	22.24	0.05	0.69	0.52	1.20	22.25	181	26.45	-0.53	0.40	0.86	1.13	26.50
43	22.29	0.02	0.68	0.52	1.20	22.30	185	26.56	-0.58	0.41	0.70	1.21	26.64
44	22.34	0.01	0.67	0.52	1.20	22.34	189	26.70	-0.52	0.38	0.88	1.34	26.89
45	22.40	0.01	0.68	0.53	1.20	22.41	193	26.92	-0.56	0.45	0.93	1.32	27.23
46	22.45	0.03	0.68	0.52	1.19	22.47	197	26.98	-0.57	0.46	0.85	0.64	27.15
47	22.50	0.03	0.67	0.52	1.20	22.52	201	27.15	-0.81	0.45	0.98	0.66	27.47
48	22.57	0.01	0.67	0.54	1.21	22.58	205	27.40	-0.92	0.49	0.91	0.51	27.58

^aSee note to Table 9A.

^aBased on averages within circular annuli in the plane of NGC 7531, assuming an inclination of 65° and a major-axis position angle of 25° . Radii are in arcseconds, and all surface brightnesses are in mag arcsec $^{-2}$. Note that U here is based only on CTIO plate 5358, since no U -band CCD photometry was obtained.

TABLE 9B

AZIMUTHALLY AVERAGED CCD SURFACE PHOTOMETRY^a

r	μ_B	U-B	B-V	V-R	V-I	μ_{BJ}	r	μ_B	U-B	B-V	V-R	V-I	μ_{BJ}
0	18.52	0.51	0.95	0.79	1.41	0	18.52	0.51	0.95	0.66	0.66	0.49	1.09
1	18.75	0.52	1.04	0.66	1.30	1	18.75	0.52	1.04	0.60	0.63	0.49	1.10
2	19.00	0.51	1.01	0.60	1.26	2	19.00	0.51	1.01	0.60	0.64	0.49	1.11
3	19.23	0.49	0.98	0.58	1.25	3	19.23	0.49	0.98	0.58	0.64	0.49	1.13
4	19.43	0.47	0.97	0.56	1.24	4	19.43	0.47	0.97	0.56	0.64	0.50	1.14
5	19.63	0.46	0.96	0.55	1.23	5	19.63	0.46	0.96	0.55	0.64	0.50	1.16
6	19.81	0.45	0.95	0.54	1.22	6	19.81	0.45	0.95	0.54	0.64	0.50	1.16
7	19.96	0.45	0.92	0.53	1.21	7	19.95	0.45	0.92	0.53	0.64	0.50	1.16
8	20.09	0.45	0.93	0.53	1.20	8	20.10	0.45	0.94	0.55	0.64	0.50	1.17
9	20.21	0.44	0.94	0.53	1.19	9	20.22	0.44	0.94	0.55	0.64	0.50	1.17
10	20.37	0.44	0.95	0.53	1.18	10	20.36	0.42	0.92	0.54	0.64	0.50	1.18
11	20.48	0.40	0.91	0.54	1.24	11	20.48	0.41	0.92	0.55	0.64	0.50	1.19
12	20.59	0.38	0.94	0.50	1.22	12	20.58	0.39	0.91	0.54	0.64	0.50	1.19
13	20.65	0.38	0.92	0.49	1.20	13	20.67	0.38	0.90	0.54	0.64	0.50	1.18
14	20.71	0.36	0.91	0.48	1.19	14	20.72	0.36	0.88	0.54	0.64	0.51	1.18
15	20.76	0.35	0.88	0.48	1.19	15	20.78	0.34	0.87	0.53	0.64	0.50	1.19
16	20.82	0.32	0.87	0.46	1.19	16	20.84	0.31	0.85	0.52	0.64	0.50	1.19
17	20.88	0.27	0.85	0.48	1.19	17	20.89	0.27	0.83	0.52	0.64	0.50	1.20
18	20.91	0.23	0.83	0.48	1.18	18	20.91	0.24	0.83	0.52	0.64	0.50	1.20
19	20.94	0.19	0.81	0.48	1.17	19	20.95	0.19	0.80	0.51	0.64	0.51	1.21
20	20.98	0.16	0.80	0.47	1.17	20	20.98	0.16	0.77	0.51	0.64	0.51	1.20
21	21.00	0.13	0.77	0.49	1.18	21	21.00	0.15	0.74	0.51	0.64	0.51	1.21
22	21.01	0.10	0.75	0.49	1.16	22	21.00	0.10	0.73	0.50	0.64	0.51	1.21
23	21.00	0.10	0.72	0.50	1.15	23	21.01	0.08	0.71	0.50	0.64	0.52	1.21
24	20.99	0.08	0.69	0.49	1.14	24	20.99	0.07	0.70	0.49	0.64	0.51	1.21
25	20.99	0.07	0.67	0.49	1.13	25	21.03	0.02	0.68	0.50	0.64	0.52	1.21
26	21.02	0.05	0.66	0.49	1.12	26	21.05	0.01	0.66	0.49	0.64	0.52	1.21
27	21.06	0.03	0.65	0.50	1.12	27	21.08	-0.03	0.65	0.49	0.64	0.52	1.21
28	21.10	0.01	0.64	0.50	1.11	28	21.11	-0.01	0.64	0.48	0.64	0.51	1.20
29	21.13	0.00	0.62	0.50	1.10	29	21.14						

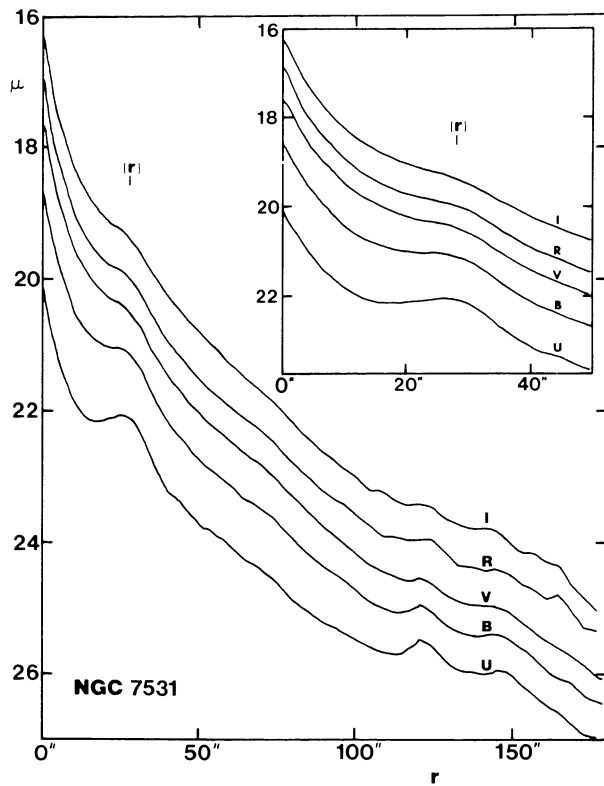


FIG. 29

FIG. 29.—Azimuthally averaged luminosity profiles (mag arcsec^{-2}) in all passbands. The averages were taken in circles in the plane of the galaxy, assuming that the inclination is 65° and the major-axis position angle is 25° . The U -band profile has been displaced by +1 mag for clarity. The position of the inner ring (r) is indicated.

FIG. 30.—Azimuthally averaged color-index profiles, illustrating the large radial color gradients. The position of the inner ring (r) is indicated.

to the ring region and will be used for the velocity-position angle analysis in § IVg. The inclination and line-of-nodes position angle used are those derived in § IVa, and it should be noted that only points within 40° of the major axis were used. Because of the diffuse emission the rotation curve is very well defined in the inner regions. The mean error per point is only 10 km s^{-1} or less in this region, and the rotation here is more precisely determined than outside the ring. At the position of the ring the mean error per point is less than 5 km s^{-1} . Figure 33 shows how close the inner ring is to exact turnover. The ridgeline radius in blue light is indicated on each side and is seen to be only very slightly inside of exact turnover.

Figure 33 also shows that there is a slight asymmetry in the rotation curve. The rotation velocities outside the ring are more or less constant on the northeast half of the major axis, but on the southwest half there is a dip outside the ring and then apparently a rise. All of the points at $r > 100''$ on this side are associated with the bright single H II region in the southwest spiral arm, and the TAURUS data and the slit spectra were found to be in good agreement on the radial velocity of the object. Lacking measurements of any other outer H II regions on this side, it cannot be determined whether the rise is due to a genuine asymmetry or to a large component of peculiar motion associated specifically with this

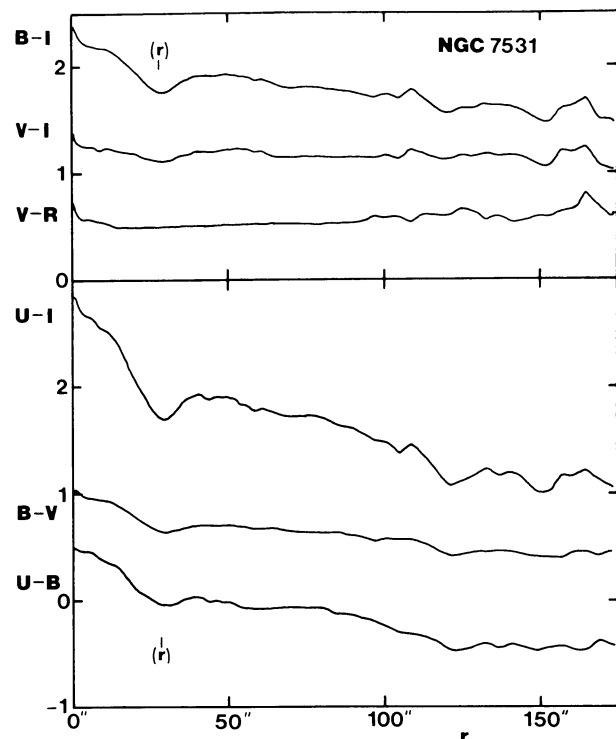


FIG. 30

object. In any case a mean representation of the rotation curve was obtained by ignoring the dip and the rise on the southeast side. The solid curves in Figure 33 are defined by the following equations:

$$V(r) = \begin{cases} 10.375r - 0.151r^2, & r < 34'' \\ 178.2, & r > 34'' \end{cases}$$

The standard deviation of the residuals from the parabolic solution for $r < 34''$ is only 3.1 km s^{-1} , and is seen to be an excellent representation.

Figure 34 shows four models of the rotation curve of NGC 7531 used to obtain a mass and mass-to-light ratio. For the purposes of the modeling, the rotation curve in Figure 33 was folded about the center and the points immediately outside the ring were averaged in $5''$ intervals, while all points having $r > 100''$ were averaged into a single point (see Table 10). The upper left-hand panel of Figure 34 shows a representation based on a combination of two inhomogeneous spheroids having a polynomial density distribution of index $n = 2$ (Perek 1962). The inner spheroid has a radius of $40''$ and an intrinsic axis ratio of 0.9 to represent the bulge, while the outer spheroid has a radius of $200''$ and an intrinsic flattening of 0.1 to represent the disk. The masses and mass-to-light ratios for this model are summarized in Table 11 for two values of limiting radii r_l : the edge of the zone just

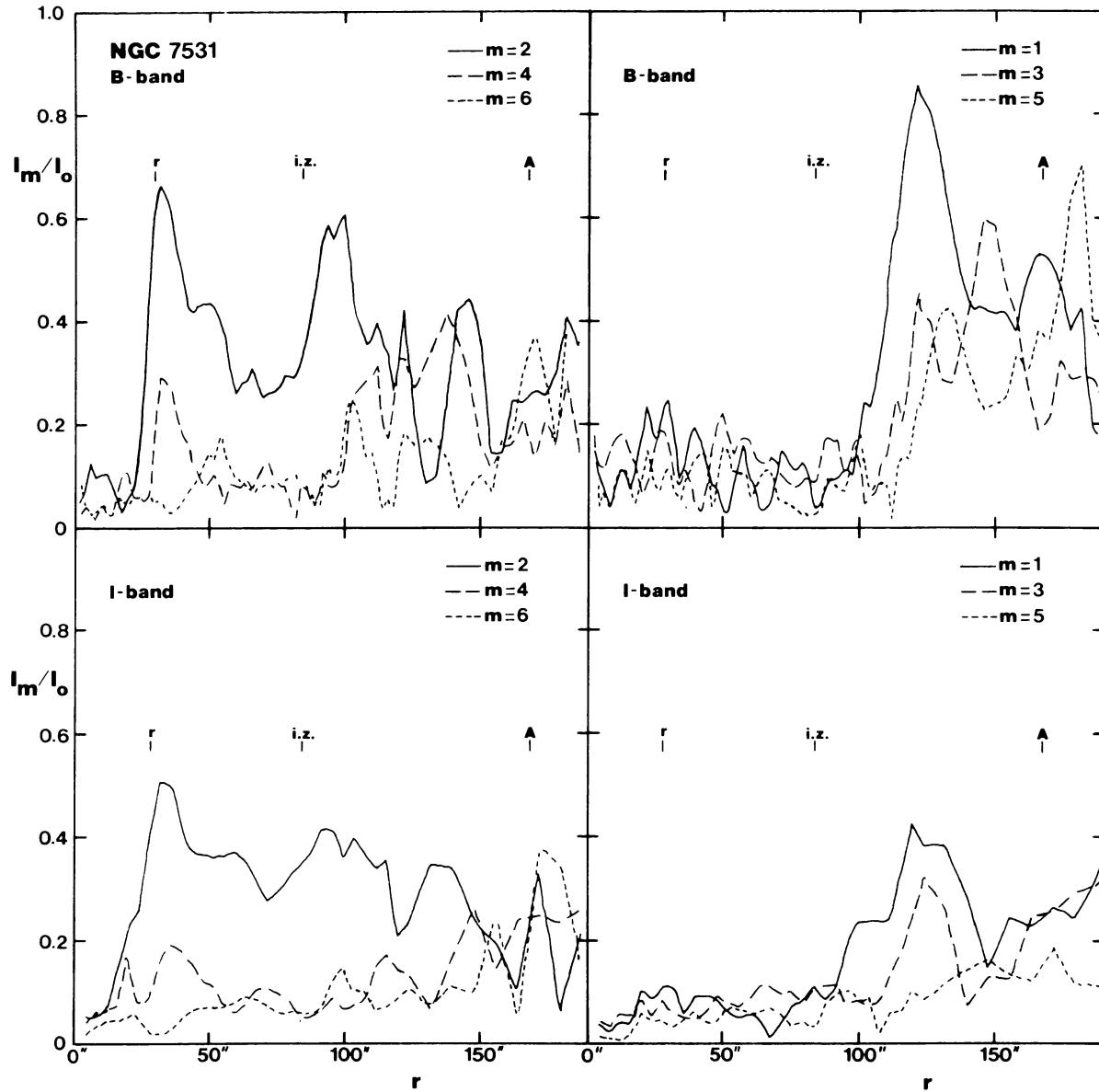


FIG. 31.—Relative amplitudes of Fourier components $m = 1-6$ in the B and I passbands. These allow for the spherical shape of the bulge, assuming the model II decomposition parameters. Note the dominance of the $m = 2$ term and the relative insignificance of the $m = 4$ and $m = 6$ terms. The odd terms are significant only in the outer regions and are due to asymmetries in the outer arms. The radial positions of the inner ring (r), the edge of the intermediate zone ($i.z.$), and the outer arms (A) along the major axis are indicated.

outside the ring at $r = 85''$, and the outermost mean point at $r = 131''$. The total luminosity enclosed within each of these points was derived from the blue-light surface photometry. The model appears to yield a mass-to-light ratio which increases with increasing radius. For the inner value of r_i , $M/L = 3.8$, while for the outer value, $M/L = 5.7$. The point mass-to-light ratio of 10.6 within the Holmberg radius ($185''$) is similar to average values derived for a large number of galaxies by Faber and Gallagher (1979), after reduction to the zero point of de Vaucouleurs's distance scale. As a check on the trend, the surface density of the Perek model was calculated, and, using the azimuthally averaged blue-light luminosity profile derived in § IVe, the radial variation of M/L was

derived. The result is illustrated in Figure 35, which shows that M/L rises from about 3.5 in the inner regions to about 13 near $r = 100''$.

Analogous to the inhomogeneous spheroid approach, the lower two panels in Figure 34 show the rotation curves predicted by the azimuthally averaged B - and I -band light distributions in NGC 7531. Kalnajs (1983) and Kent (1986) have shown how the assumption of constant M/L with radius can reproduce some optical rotation curves very well, sometimes without the need of introducing a massive halo to the potential. For the fits here, azimuthally averaged profiles of the disk corrected for the bulge were calculated, and rotation profiles for each component were derived separately.

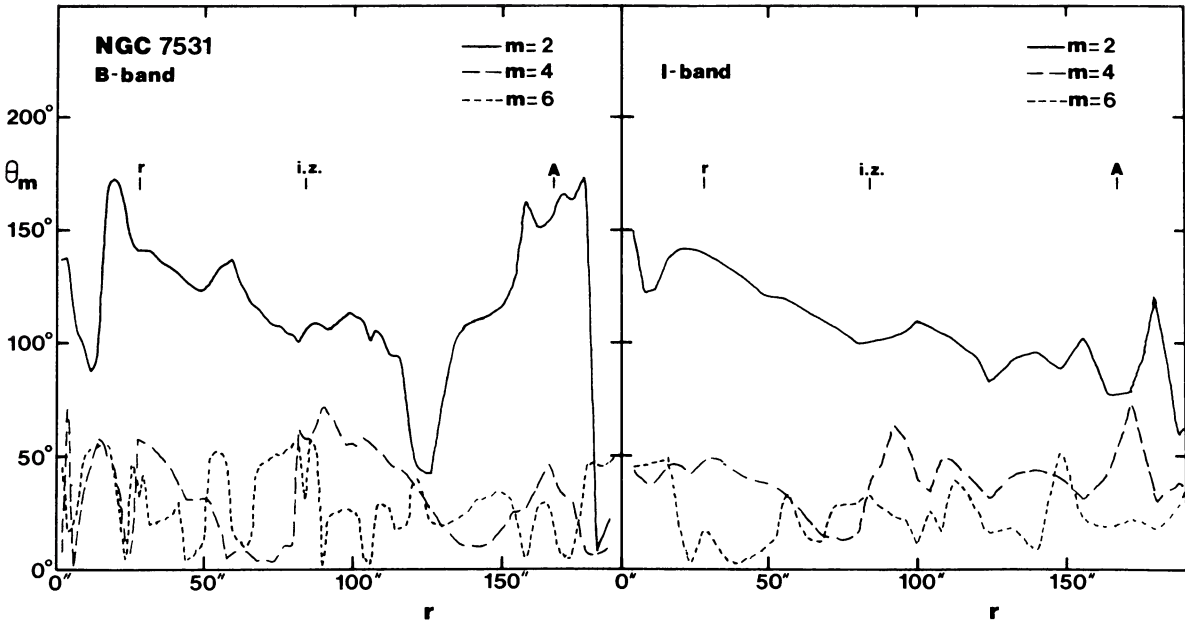


FIG. 32.—Phases of the even Fourier terms with respect to the line of nodes in the galaxy plane, for both the B and the I passband

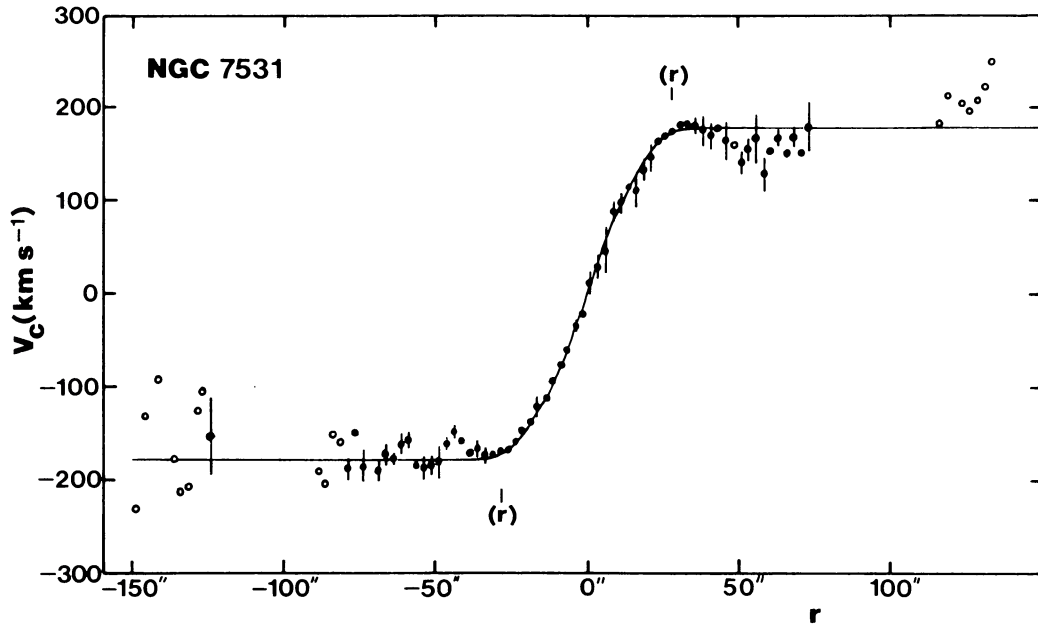


FIG. 33.—Emission-line rotation curve of NGC 7531. Note slight asymmetry between the northeast (negative radii) and southwest (positive radii) sides, and also how the inner ring lies very close to the “turnover radius” on each side. Points based on only a single spectrum are indicated by open circles.

Least-squares fits to the observed rotation curve were then made, allowing spheroid and disk to have different values of M/L . It was found that, for both passbands, best fits are obtained if the bulge either is ignored or has a much smaller M/L than the disk. In either case the light distribution provides a poor representation of the rotation curve. The inner ring causes a large effect even in the I band which is not

observed, while the inner regions predict too steep a rise and the outer regions predict a decline where the rotation velocity is mostly constant.

The decline in the outer parts is similar to that predicted by light distributions in NGC 753, NGC 1085, and NGC 2998 observed by Kent (1986), and suggests that NGC 7531 has a massive halo of dark matter. However, at least some of the

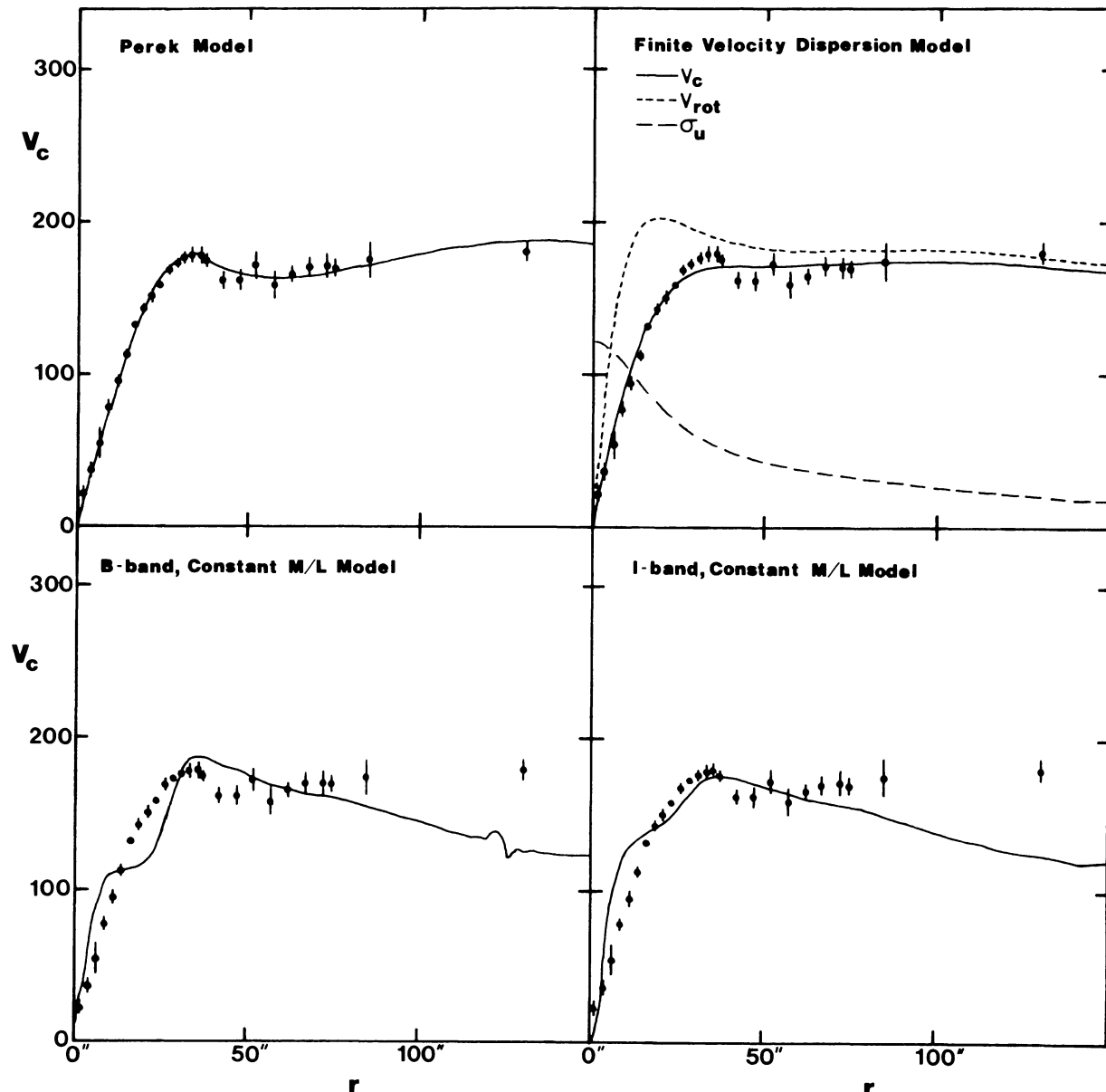


FIG. 34.—Models of the rotation curve of NGC 7531. The upper panels show two analytic models, one based on a combination of Perek inhomogeneous spheroids having a polynomial density distribution of index $n = 2$, and a second based on a two-component model having finite velocity dispersion. In this latter model, V_{rot} is the rotation component of the velocity, while σ_u is the radial velocity dispersion. The two lower panels show models where the B - and I -band azimuthally averaged light distributions have been transformed into a rotation curve, assuming that constant mass-to-light ratios characterize the bulge and disk. The spherical shape of the bulge has been allowed for in the fits using model II decomposition parameters.

disagreement in the inner regions (as well as the low required M/L of the bulge) may be due to neglect of finite velocity dispersion. To evaluate this, the upper right-hand panel of Figure 34 shows a two-component finite velocity dispersion model based on formulae given by Davoust and de Vaucouleurs (1980) and the precepts of Miyamoto and Nagai (1975). The model has five parameters (Table 12): the masses M_1 and M_2 of the bulge and disk, respectively, and three scale lengths a_1 , a_2 , and b such that the ratio $b/(a_1 + b)$ describes the flattening of the bulge and $b/(a_2 + b)$ describes the flattening of the disk. The model in Figure 34 is not the

best fit in a least-squares sense, but it has the most reasonable parameters, including a predicted central velocity dispersion which is reasonable for the type and absolute magnitude of NGC 7531. The model yields $\sigma_V(0) = 122 \text{ km s}^{-1}$, while a reassessment of the Faber-Jackson $L \sim \sigma_V^4$ law for spiral bulges by de Vaucouleurs and Olson (1982) and de Vaucouleurs (1983) suggests an expected dispersion, $\sigma_V(0) = 114 \text{ km s}^{-1}$, for the type and absolute magnitude of NGC 7531. The parameters indicate that for this model the M/L of the bulge exceeds that of the disk by a factor of ~ 3 . The model is not, however, satisfactory because the velocity dis-

TABLE 10
ROTATION CURVE OF NGC 7531

r (1)	V_c (km s $^{-1}$) (2)	N (3)	σ_1 (km s $^{-1}$) (4)	Mean Error (km s $^{-1}$) (5)	r (1)	V_c (km s $^{-1}$) (2)	N (3)	σ_1 (km s $^{-1}$) (4)	Mean Error (km s $^{-1}$) (5)
1.25.....	22.0	7	10.2	3.9	33.75....	179.2	7	13.0	4.9
3.75.....	37.3	6	10.6	4.3	36.25....	178.7	7	12.8	4.8
6.25.....	55.1	7	28.1	10.6	37.50....	175.5	12	8.9	2.6
8.75.....	78.4	8	9.4	3.3	42.50....	162.6	15	18.2	4.7
11.25.....	95.4	9	13.9	4.6	47.50....	161.9	11	21.6	6.5
13.75.....	113.2	6	6.7	2.7	52.50....	172.3	12	26.4	7.6
16.25.....	132.6	5	2.5	1.1	57.50....	158.7	9	27.5	9.2
18.75.....	143.5	6	6.0	2.4	62.50....	165.7	11	15.6	4.7
21.25.....	151.3	7	9.5	3.6	67.50....	170.7	12	20.6	5.9
23.75.....	159.1	7	4.6	1.7	72.50....	171.0	8	23.1	8.2
26.25.....	169.2	8	7.5	2.6	75.00....	170.0	12	19.1	5.5
28.75.....	173.5	6	2.9	1.2	85.00....	174.9	4	24.3	12.2
31.25.....	176.5	7	6.4	2.4	130.52....	180.1	15	32.4	8.4

Col. (1).—Radius in galaxy plane.

Col. (2).—Mean rotation velocity, assuming pure circular motion.

Col. (3).—Number of points in mean.

Col. (4).—Standard deviation about mean.

Col. (5).—Mean error of mean.

TABLE 11
MASS ESTIMATES FOR NGC 7531

r_t (kpc) (1)	$M(r \leq r_t)$ ($10^{10} M_\odot$) (2)	$L(r \leq r_t)$ ($10^{10} L_\odot$) (3)	$f_0(r < r_t)$ (4)	Notes (5)
10.83.....	7.98	1.01	7.9	1
15.30.....	11.27	1.06	10.6	2
10.83.....	5.71	1.01	5.7	3
7.03.....	3.34	0.89	3.8	4
.....	8.15	1.10	7.4	5

NOTES.—(1) Mass from point-mass method to $r_t = 131''$, using $V_m = 178$ km s $^{-1}$. (2) Mass from point mass method to Holmberg radius, $r_t = 185''$, assuming same value of V_m . (3) Mass from Perek model to $r_t = 131''$. (4) Mass from Perek model to edge of “intermediate zone” at $r_t = 85''$. (5) Mass from finite velocity dispersion model.

Col. (1).—Radius of farthest point.

Col. (2).—Mass interior to farthest point.

Col. (3).—B-band luminosity interior to farthest point.

Col. (4).—Mass-to-blue light ratio within r_t ($\odot = 1$).

persion remains fairly high (~ 20 km s $^{-1}$) in the disk. This may be due to the main weakness of the model, the requirement that the parameter b be the same for the bulge and disk components (de Vaucouleurs, Pence, and Davoust 1983). The model nevertheless suggests that the low values of M/L for the bulge required by the light distribution fits and implied by the Perek model may be due (at least in part) to neglect of finite velocity dispersion in the inner regions.

g) Kinematics and Dynamics of the Inner Ring

The inner ring of NGC 7531 is a locally enhanced zone of ionized gas embedded within a diffuse disk of ionized gas. To examine the kinematics of the material in this region, I use a

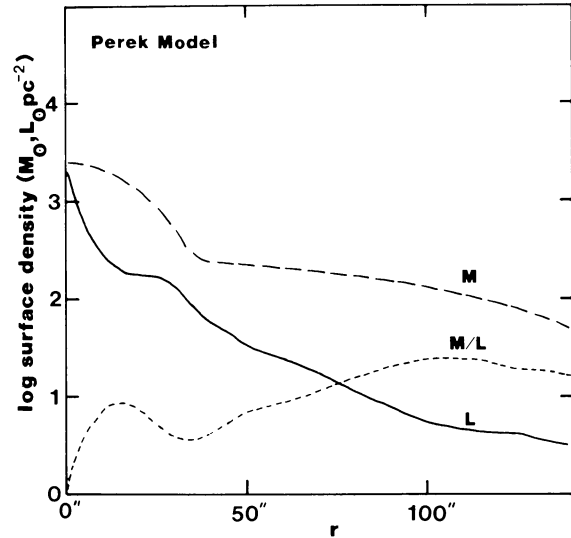


FIG. 35.—Surface densities and mass-to-blue light ratio for the Perek inhomogeneous spheroids model, to illustrate how this kind of model predicts a very low mass-to-light ratio in the bulge. An identical effect is found in the light-curve fits. This may be partly an artifact of the neglect of finite velocity dispersion.

velocity-position-angle diagram such as was used by van der Kruit (1974, 1976) for the inner ring of NGC 4736. The ring of NGC 7531 is most similar to that in NGC 4736 in terms of size and relative brightness than to the ring of NGC 1433, and hence a comparison with NGC 4736 is worthwhile.

The velocity-position-angle diagram for the inner ring was obtained by isolating all velocity points in an elliptical annulus having major-axis position angle 14°, axis ratio 0.42, and in the narrow radius range $24'' \leq r \leq 30''$. Three models

were fitted to the resulting curve: pure circular motion, expanding/contracting ring, and resonance dispersion orbit.

The pure rotation fit is shown in Figure 36a. The high inclination gives a cusped appearance to the radial velocity curve, and the model is seen to give a very good representation of the data. The model parameters, $V_{\text{sys}} = 1598 \text{ km s}^{-1}$ and $\theta_0 = 202.2^\circ \pm 0.8^\circ$, are in excellent agreement with those derived from the iterative method described in § IVa. This agreement is important because the results from the iterative method are based on points within 40° of the major axis only and over a large radius range, while the ring fit is only over a $6''$ range.

TABLE 12
PARAMETERS OF FINITE VELOCITY DISPERSION MODEL

Parameter	Value	Notes
Spheroid		
a_1 (kpc)	0.46	
b (kpc)	0.58	
c_1/a_1	0.56	
M_1	$2.48 \times 10^{10} M_\odot$	
L_1	$0.14 \times 10^{10} L_\odot$	1
$f_{01} (\odot=1)$	17.6	
Disk		
a_2 (kpc)	12.91	
b (kpc)	0.58	
c_2/a_2	0.043	
M_2	$5.67 \times 10^{10} M_\odot$	
L_2	$0.95 \times 10^{10} L_\odot$	2
$f_{02} (\odot=1)$	6.0	

NOTES.—(1) Assumes $k_1(B) = 0.13$ from Table 8.
(2) Assumes $k_{\text{II}}(B) = 1 - k_1(B)$.

An attempt to fit a ring having a uniform radial component in addition to the circular motion is shown in Figure 36b. The model is essentially identical with the pure rotation fit, because the resulting expansion velocity is an insignificant $5 \pm 5 \text{ km s}^{-1}$. At the high inclination of NGC 7531, any significant expanding motion would be visible as an asymmetry in the velocity-position-angle diagram and would be accompanied by a shift of the apparent line of nodes. Since no shift or very significant asymmetry is observed, it appears that the inner ring of NGC 7531 is not expanding.

The final model that I consider is an epicyclic orbit at the inner Lindblad resonance (ILR) (Lindblad 1955; Lindblad and Jorsater 1981). This represents an ordinary unperturbed galactic orbit which appears closed in a reference frame rotating at an angular velocity $\Omega_p = \Omega - \kappa/2$ (Ω = mean circular angular velocity; κ = epicyclic frequency). An unperturbed dispersion orbit has variable radial and tangential velocity components as motion proceeds, but angular momentum is a constant of the motion. The path is characterized by a harmonic motion about a “guiding center,” r_0 :

$$r = r_0 + \Delta r \cos \kappa(t - t_0), \quad (1a)$$

$$\theta = \theta'_0 + \Omega(t - t_0) - 2(\Omega \Delta r / \kappa r_0) \sin \kappa(t - t_0), \quad (1b)$$

where Δr is the amplitude of the radial displacement of the epicycle and θ'_0 is the major-axis position angle of the deprojected orbit. The radial and tangential velocity components in the inertial frame are given by

$$v_r = -2\Delta r(\Omega - \Omega_p) \sin 2(\theta' - \theta'_0), \quad (2a)$$

$$v_t = r\Omega - 2\Omega\Delta r \cos 2(\theta' - \theta'_0), \quad (2b)$$

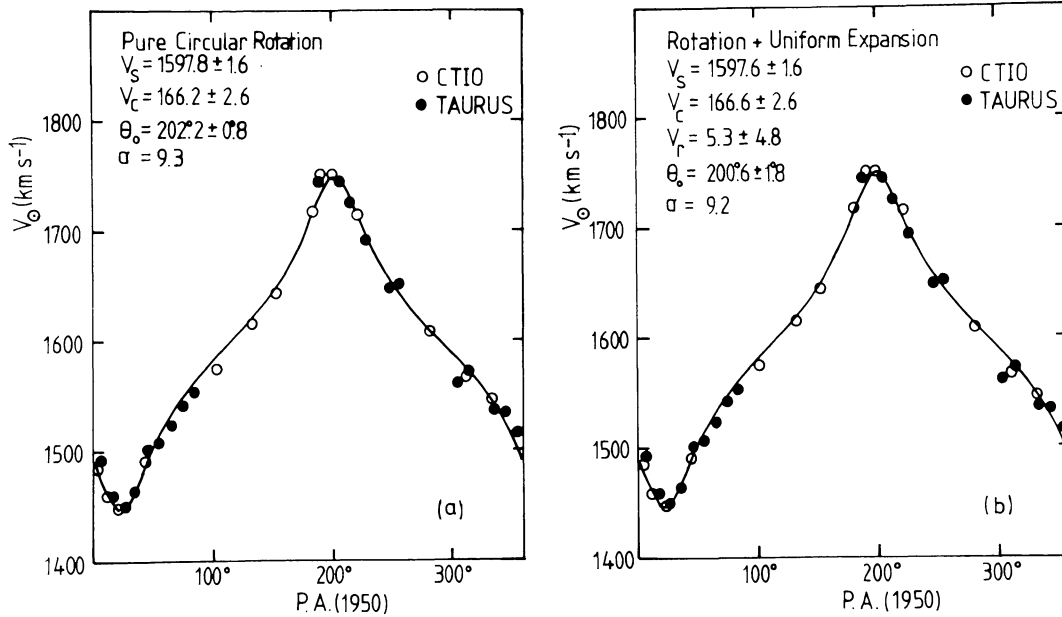


FIG. 36.—Models of the velocity-position-angle diagram of the inner ring of NGC 7531 for the cases of (a) pure circular rotation and (b) circular rotation with uniform radial expansion. Units are km s^{-1} for systemic velocity V_s , circular velocity V_c , expansion velocity V_r , and standard deviation σ .

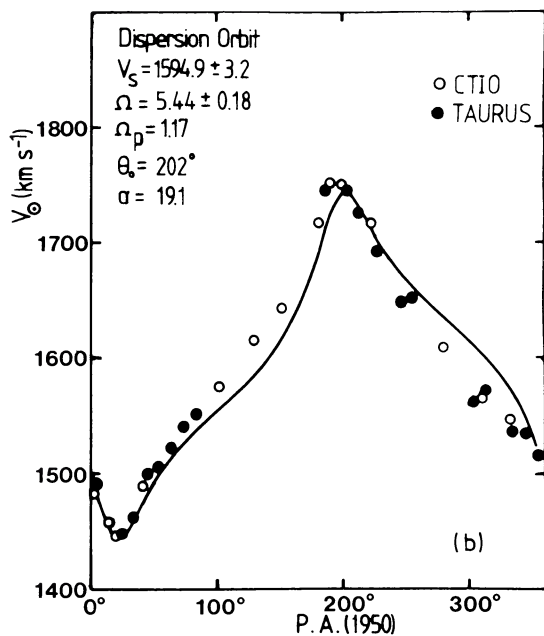
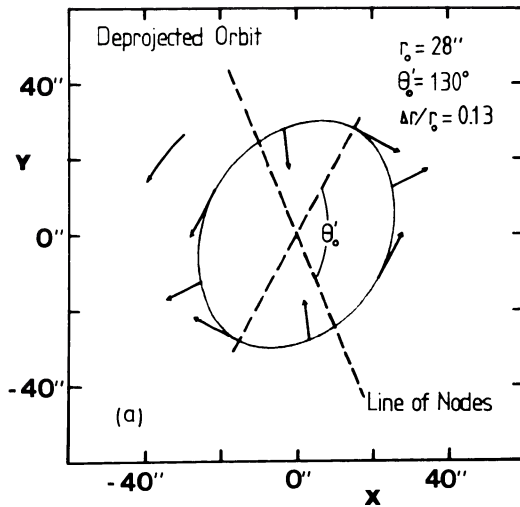


FIG. 37.—Dispersion orbit model of the inner ring of NGC 7531: (a) Geometry of the deprojected orbit, showing line of nodes, major-axis position angle, and epicyclic velocity. (b) Predicted velocity-position-angle diagram for the orbit as compared with velocities in the ring. Units of Ω and Ω_p are $\text{km s}^{-1} \text{arcsec}^{-1}$.

where θ' is the part of θ which moves uniformly with time t . In applying these equations, the parameters $i = 65^\circ$ and $\theta_0 = 202^\circ$ are assumed to obtain the true shape and orientation of the orbit (Fig. 37a).

In Paper II the large eccentricity of the inner ring of NGC 1433 together with accurate knowledge of its true shape was used to measure the pattern speed of the bar. However, for a highly inclined galaxy this approach is difficult to apply because dust and finite thickness can affect the apparent shape of the ring, leading to considerable uncertainty in the true shape. Rather than use the orbit to derive the pattern speed, I will instead make an estimate of the pattern speed from the rotation curve alone. The pattern speed, Ω_p , is derived from the variation of $\Omega - \kappa/2$ with radius implied by the rotation curve, assuming that the mean radius of the deprojected ring is exactly at the ILR (Fig. 38). The polynomial representation of the rotation curve is used for this purpose, and no consideration is given to the effects of velocity dispersion. If the inner ring is assumed to be located at the ILR, then the pattern speed required for the mean radius of $28''$ is $\Omega_p = 1.17 \text{ km s}^{-1} \text{arcsec}^{-1} = 14 \text{ km s}^{-1} \text{kpc}^{-1}$ if the distance is 17 Mpc. If the identification with the ILR is correct, then this approach indicates that corotation (CR) should occur near $r \sim 150''$, which is in the region of the faint outer arms. The arms themselves extend to a radius near $r \sim 170''$ along the major axis. Note that in density-wave models of spiral structure, the radius of the outermost H II region is considered one of the principal tracers of the location of CR (see, for example, Roberts, Roberts, and Shu 1975). At least for NGC 7531, the extent of the spiral pattern and the location of a bright inner ring are roughly consistent with the same pattern speed, and hence the galaxy may be a

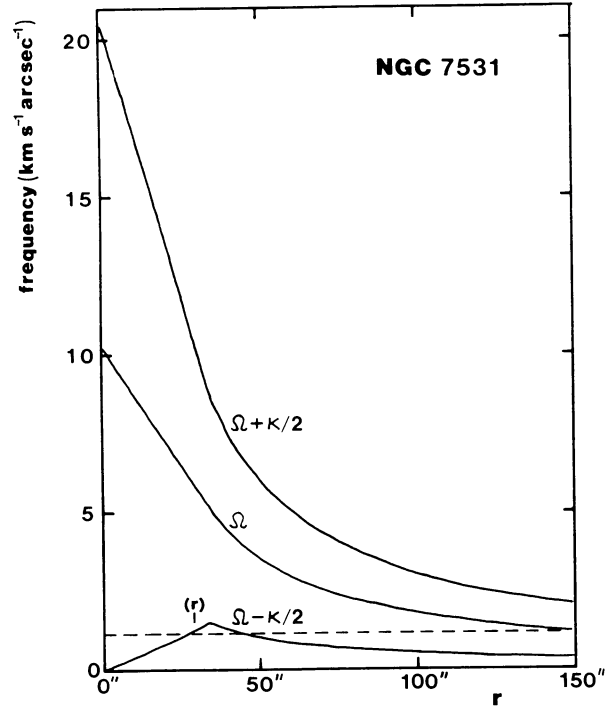


FIG. 38.—Plots of the angular velocity Ω and the precession frequencies $\Omega \pm \kappa/2$ against radius, based on the polynomial representation of the rotation curve. This ignores the effects of velocity dispersion, and is used to estimate the pattern speed in NGC 7531 assuming the inner ring is associated with inner Lindblad resonance. The pattern speed, Ω_p , from this assumption is shown by the dashed line.

fruitful one to examine further in the context of density-wave models. With this choice of pattern speed, only the systemic velocity and the mean angular velocity Ω are solved from the velocity-position-angle diagram of the inner ring by least squares.

The model is shown in Figure 37b. It predicts a large asymmetry in the apparent shape of the velocity-position-angle diagram which is not observed. Figure 37a shows why: the deprojected orientation of the orbit places virtually the full effect of the radial component of the epicyclic motion (in its outward phase) along the line of sight. We have no freedom in this case to vary the lines-of-nodes position angle, θ_0 , significantly in order to improve the fit because this parameter is determined reliably both from surface photometry and from the velocity points in the rest of the galaxy. The poor quality of the fit indicates either that an unperturbed dispersion orbit is perhaps too unrealistic an interpretation of the inner ring, or that the deprojected shape and orientation of the feature are incorrect. Figure 37a shows that the deprojected orbit has an intrinsic axis ratio of about 0.8, and this arises in part because the apparent major-axis position angle of the ring is displaced 8° from the (kinematic) line of nodes. It is possible that dust and finite thickness are affecting the apparent shape significantly enough that the deprojected orbit is being made too elongated. A model of pure circular rotation seems the best for this case.

V. DISCUSSION

Although the observations in this paper do not prove that the ring is a resonance feature, they do help to rule out one alternative model which has gained some acceptance in recent years. This is the "explosion hypothesis," first suggested by van der Kruit (1974, 1976) as being the most likely explanation for the motions observed by him in the inner ring of NGC 4736. Sanders and Bania (1976) examined the theoretical consequences of such an explosion and concluded that an H II ring would form having properties similar to those observed in NGC 4736. The main property of such a feature which is most relevant to NGC 7531 is that, because the gas in the ring comes from regions having lower angular momentum than the local material encountered farther out, the gaseous rotation curve should show a "dip" across the ring. Sanders and Bania (1976) suggest that these dips ought to be of order 75 km s^{-1} for a typical explosion energy of 10^{58} ergs and present radius of 2–3 kpc. The fact that the ring of NGC 7531 shows no such dips, is located almost exactly at turnover, shows little evidence for expanding motions, and is filled with diffuse emission would appear to rule out this kind of model completely.

If the ring is a resonance feature, is it a resonance with an oval distortion or a density wave? Kormendy and Norman (1979) showed that density waves are maintained most easily in the presence of differential rotation if bars or companions are present, but that in the absence of these structures, disk instabilities survive well only if the disk rotates rigidly enough to avoid an ILR. There are no large companions near NGC 7531, except for the (probable) dwarf A2311.8–4353. It is not clear that this object is associated with NGC 7531, and even if

it were, it probably does not have a large enough mass to influence the internal dynamics of NGC 7531 significantly. Among more distant companions, those having size and brightness similar to NGC 7531 are NGC 7496, NGC 7552, and the Grus Group, NGC 7582, NGC 7590, and NGC 7599. All of these are 10 or more standard RC2 isophotal diameters distant, and may not be near enough to have had a significant recent effect on the internal dynamics of NGC 7531. A few smaller galaxies are closer than this, but are of unknown redshift and not obviously related to NGC 7531.

The global outer spiral pattern in NGC 7531 would place it in the "grand design" class of SA spirals (Elmegreen 1981). In the notation of Elmegreen and Elmegreen (1982), the arm class is AC = 12, implying that the optical appearance is dominated by two long, sharply defined symmetric arms. These authors showed that while grand design spirals are found in only 32% of field SA galaxies, nearly 70% of SA galaxies which are members of groups show such patterns. They argue that group companions, like binary companions, enhance global spiral patterns. Since NGC 7531 is a member of a loose group, the environmental influences could be driving a density wave which in turn possesses an ILR near the center.

The most plausible interpretation nevertheless is that the ring and outer arms of NGC 7531 have formed in response to a weak barlike distortion or oval. The Fourier analysis suggests that such a structure probably exists in NGC 7531 in the intermediate zone, but even if this is an artifact of uncertain orientation parameters, there is still some evidence for a near-infrared bar interior to the ring. It has been demonstrated by many authors (see Kormendy 1982 and references therein) that only a mild oval or barlike distortion could generate rings and density waves in the gas distribution, and many other authors (de Vaucouleurs 1963; Kormendy 1979; Simkin, Su, and Schwarz 1980; Kormendy and Norman 1979; Bosma 1978; Paper I) have emphasized how widespread these distortions are among spirals. Any such distortion, if sufficiently subtle, would sometimes be difficult to detect in optical surface brightness distributions (especially in systems at high inclination), but often can significantly perturb the gas flow (e.g., Bosma 1978). The main problem with this interpretation is that if a bar is present in NGC 7531, it is either not strong enough to perturb the gas flow greatly or the orientation of the bar is not favorable for detecting the associated noncircular motions with the limited coverage of the optical velocity data.

The coincidence between the position of the ring and the turnover radius is interesting because it suggests that the very weak near-infrared bar interior to the ring has been built up in a manner proposed by Lynden-Bell (1979). This bar would therefore be a different phenomenon from that in NGC 1433, which is probably built up from orbits extending to near corotation (see also Kormendy 1982 and Elmegreen and Elmegreen 1985).

Can the observations of NGC 7531 shed any light on why the inner rings of SA galaxies show a much larger dispersion in relative and absolute sizes compared with barred galaxies? The most straightforward interpretation is that many of the features classified as inner rings in (single-ring) SA galaxies

are probably linked with the ILR (as in NGC 7531) and not with the inner second harmonic resonance (2HR⁻), the resonance (where $\Omega_p = \Omega - \kappa/4$) believed to be linked with most SB inner rings (Schwarz 1979, 1984a, b, c, 1985). Hence, their positions would be very sensitive to the dynamics of the inner regions. It is in the inner regions where galaxy rotation curves are least homogeneous because the rate of rise to maximum velocity depends on the amount of mass in the bulge and the central density (Rubin, Ford, and Thonnard 1980; Rubin *et al.* 1982, 1985). The relative position of the ILR, for example, with respect to the standard isophotal radius would be expected to be much less homogeneous than the relative position of 2HR⁻ because of this (Athanassoula *et al.* 1982; de Vaucouleurs and Buta 1980b; Buta 1984).

However, *absolute positions* are another matter. If rings are in general linked to resonances, then absolute positions will be determined not only by the form of the rotation curve but also by the pattern speed. Absolute sizes of SA inner rings are just as inhomogeneous as relative sizes, while both the sizes and relative sizes are homogeneous for barred spirals (de Vaucouleurs and Buta 1980b; Buta and de Vaucouleurs 1982).

A second explanation for the inhomogeneity is that, for reasons not well understood, some features classified as inner rings in SA galaxies (especially in those objects of early Hubble types) form at 2HR⁻ just as those in barred spirals. This is likely because in many double-ring SA galaxies, the same ring ratio, $\langle d_R/d_r \rangle = 2.2$, is observed as in barred galaxies (see Paper I). This ratio is believed to link outer rings strongly to the outer Lindblad resonance (OLR) and inner rings to 2HR⁻ in barred galaxies (Athanassoula *et al.* 1982), and its observation in SA galaxies suggests that the same resonances are involved (Buta 1984; Athanassoula and Bosma 1985). Occasional three-ring SA systems are observed that reinforce these remarks (Paper I).

A third explanation is that the spiral structure in some SA galaxies is driven by a companion (Kormendy and Norman 1979). The ring could then represent a resonance with a density wave rather than a bar (for example, NGC 5364; see Lin 1971; Buta 1984), and the pattern speed of this wave would perhaps in part be determined by the external forcing. Such forcing is not likely to be as homogeneous as that from the internal perturbations which can arise naturally in galaxies, and therefore rings associated with such density waves need not be homogeneous in size.

Finally, the resonance hypothesis may not be able to account for all types of rings observed in SA galaxies. Of special interest are SA galaxies showing "NGC 2841-type" or flocculent spiral structure (Kormendy 1979; Elmegreen 1981). Some galaxies of this type also show rings and pseudorings, a few examples being NGC 488, NGC 5055, and NGC 7217 (all are illustrated in Sandage 1961). In these cases it is not clear that the ring can be a resonance with even a density wave because Elmegreen and Elmegreen (1984) showed that the flocculent structure is almost pure star formation in some galaxies that is probably produced by a stochastic process (Seiden and Gerola 1979). While it is possible that rings in such galaxies *originally* formed in response to perturbations whose growth was eventually inhibited or even reversed by the influence of an ILR (Kormendy and Norman 1979), some

rings may be tidally produced, expanding structures (P. J. Quinn 1983, private communication) or axisymmetric disturbances (Toomre 1964; Miller 1978; J. M. Huntley 1983, private communication). Again, such structures should add inhomogeneity to ring size and shape distributions, and furthermore are likely to be transient.

VI. CONCLUSIONS

The main results of this paper can be summarized as follows:

1. NGC 7531 is a global, two-armed spiral galaxy possessing a bright inner ring with a radius of 2.3 kpc. The ring has an average surface brightness in blue light $\sim 4\text{--}6$ times higher than that in NGC 1433, and is also 2.5 times smaller in size.

2. The ring is a zone of active star formation and H II region concentration. It appears to consist of discrete associations embedded within a diffuse background, or "old ring." The colors within the ring (uncorrected for underlying components) are the same as the integrated colors of ordinary Sbc-Im galaxies, implying that the feature is not a single "starburst" phenomenon but rather is a place where star formation has occurred continuously. The enhancement of H α is also embedded within a diffuse H α disk that permeates the entire zone inside the ring.

3. The light distribution within NGC 7531 cannot be modeled in terms of a simple combination of an $r^{1/4}$ spheroid, exponential disk, and ring. A third component which is flat like the disk contributes significantly within the ring. This component appears to be much redder than the disk, and may have an exponential profile with a smaller scale length than the disk.

4. A Fourier analysis suggests that the "intermediate zone" between the inner ring and the outer arms is intrinsically oval with a phase of $\sim 100^\circ$ with respect to the line of nodes in the galaxy plane. There may also be a very weak bar interior to the ring which is most prominent in the near-infrared.

5. There appear to be intrinsic azimuthal variations in color around the ring. Except for the near (east) side, which is affected by dust, the ring is bluest near its deprojected major axis. These zones are also where the greatest concentrations of H II regions and associations are found.

6. The rotation curve of NGC 7531 is fairly normal for an intermediate- to high-luminosity spiral galaxy, but the ring itself displays a curious coincidence: it is located almost exactly at the turnover radius. This coincidence is not usually found for the inner rings of early to intermediate barred spirals, but is more analogous to what is found for the *nuclear rings* of such galaxies (see Buta 1984).

7. The optical kinematics of the galaxy do not show evidence for significant noncircular motions. Even when the analysis is restricted to a narrow range including the ring only, there is no evidence for expanding motions or motions consistent with even a simple resonance dispersion orbit model. Nevertheless, there are some reasons to believe that small-amplitude noncircular motions are present owing to the slight disagreement between the photometric and kinematic major axes and some aspects of the appearance of the iso-velocity contours.

8. Assuming that the ring is nevertheless some kind of resonance feature, the most plausible interpretation is that it is linked with the inner Lindblad resonance, not the inner second harmonic resonance as was found for NGC 1433. The pattern speed inferred from this identification suggests that the outer spiral arms of NGC 7531 may not extend much beyond corotation.

While these observations provide an interesting picture of an intriguing ringed galaxy, they do not really explain why the ring has formed at a resonance different from that in typical barred spirals, nor why it is much larger than a typical ILR (or nuclear) ring in such spirals. I suggest that many more rotation curves of ringed, nonbarred galaxies should be obtained in order to explore in more detail the frequency of "turnover rings" and to help further understand the differences between barred and nonbarred galaxies. They should also be obtained in order to examine as carefully as possible the systematics of galaxy pattern speeds along both the Hubble family and stage sequences, because it is an important fact that *multiple-ring* systems are most often observed among early Hubble types, while *single-ring* (or nonring) systems are most often observed among late types (de Vaucouleurs 1975b; de Vaucouleurs and Buta 1980a, b).

Finally, an important observation would be the mapping at high resolution of the distribution and kinematics of neutral

hydrogen in this galaxy to see how it compares with most other (nonringed) galaxies which have been extensively observed to date. Such observations are also likely to be able to establish more firmly any systematic large-scale noncircular motions that may be present as a result of the influence of an oval distortion.

I would like to thank Drs. D. A. Allen, G. V. Bicknell, and D. C. Carter and Mr. S. M. G. Hughes for obtaining the CCD frames of NGC 7531 while I was in a hospital recuperating from an accident. I would also like to thank Drs. B. G. Elmegreen, C. Norman, A. Kalnajs, and P. Goldreich for helpful discussions and for their interest in the problems of these kinds of galaxies. I am grateful to Dr. A. Kalnajs and Mr. S. M. G. Hughes for allowing me to use their computer program which transforms a luminosity profile into a rotation curve, and to Dr. E. Davoust for helpful unpublished details concerning the finite velocity dispersion rotation curve model. I am also grateful for the excellent copy plates of NGC 7531 which were provided to me by the UK Schmidt Telescope Unit. Finally, I am grateful to Professor G. de Vaucouleurs for initiating my interest in this galaxy and for his enthusiastic support of this work. This work is based in part on my dissertation research.

APPENDIX

THE DWARF COMPANION GALAXY A2311.8–4353

The low surface brightness companion galaxy A2311.8–4353 was included in the scans of all of the plates of NGC 7531, thereby allowing me to derive some useful photometric information on the object (Table 13). The *B*-band plate 5297 provides the deepest, most well-calibrated image of the dwarf at low light levels among all the plate material, and was used first to define a center for the object. Figure 7 shows how the isophotes of the dwarf seem to be reasonably unaffected by NGC 7531 to $\mu_B = 26.5$ mag arcsec $^{-2}$. I have therefore used this isophote to define the approximate center to be 160'' west, 34'' south of the nucleus of NGC 7531. The position angle of the major axis was also estimated to be $171^\circ \pm 3^\circ$ from this isophote.

Figure 39 shows the major- and minor-axis luminosity profiles of the dwarf based on *B* plate 5297. To improve signal-to-noise ratio at the very low surface brightness of the dwarf, the original intensity array was binned into pixels $6'' \times 6''$ in size. This low resolution has little consequence for the dwarf, since it possesses little structure on scales this small. The striking thing illustrated by Figure 39 is that this object is an excellent example of a galaxy where the standard RC2 isophotal diameter, D_{25} , may not exist. If the photometry is reliable, the peak surface brightness reached is only $\mu_B = 25.2$ mag arcsec $^{-2}$ in the faint bar (see Fig. 7). The major-axis profile is asymmetric and shows a sharper decline on the north side as compared with the south side. The minor-axis surface brightnesses (here displaced by +0.5 mag for clarity) are nearly uniform for $r < \pm 30''$, and rapidly decline thereafter in a roughly exponential manner. The dashed portion of this profile on the east side marks the region where the southwest arm of NGC 7531 is encountered.

Figure 40 shows azimuthally averaged profiles of the dwarf in all passbands (see also Table 14). The averaging was carried out in ellipses having an apparent axis ratio of 0.42, a (1950) major-axis position angle of 171° , and centered 160'' west, 34'' south of the nucleus of NGC 7531. The *B*-band profile shown is based on an average of the profiles from CTIO plate 5297 and UK Schmidt plate 2533. The latter plate did not have as reliable a calibration as the CTIO plate, but the two plates were nevertheless found to be in excellent agreement on the shape of the average profile. The UK Schmidt *J*-band profile was reduced to the zero point of the CTIO plate, and then the average was taken. The important aspect of the average profile is that it appears that the decline is exponential for $r > 105''$. If we assume that this trend can be extrapolated to infinity, then the analysis yields a total magnitude $B_T = 14.81$. It is difficult to evaluate the total uncertainty on this result, since it depends on the reliability of the sky subtraction, the calibration at very low light levels, and, most important, on the validity of the extrapolation. A conservative estimate is ± 0.2 mag.

Knowing the total magnitude, we can derive the mean effective surface brightness, m'_e , within the circular aperture which transmits half the total light, and μ'_e , the mean surface brightness within the ellipse transmitting half the total light, meant to approximate the effective isophote. The results (Table 13) show first that μ'_e and m'_e differ by a small amount (0.21 mag). Olson

TABLE 13
BASIC PARAMETERS FOR A2311.8–4353

Parameter	Value	Notes
Right ascension (1950)	23 ^h 11 ^m 80	1
Declination (1950)	-43°53'0	1
SGC Hubble type and luminosity class.....	IB(s)m V?	2
$\log A_e$	1.38 ± 0.03	
$\log D_{25}$	3
$\log D_{\text{Ho}}$	1.55 ± 0.02	4
$\log R_{\text{Ho}}$	0.38 ± 0.02	4
$\log D_{27}$	1.61 ± 0.03	
$\log D_{28}$	1.70 ± 0.04	
θ_0 (1950)	171° ± 3°	
B_T	14.81 ± 0.20	
$\mu_B(\text{max})$	25.2 mag arcsec ⁻²	
m'_e	26.09 mag arcsec ⁻²	5
m'_{e0}	25.83 mag arcsec ⁻²	6
μ_e	25.88 mag arcsec ⁻²	7
$(B-V)'_e$	0.79 ± 0.14	8
$(U-B)'_e$	0.46 ± 0.18	8
$(V-R)'_e$	0.43 ± 0.14	8
$(V-I)'_e$	1.3 ± 0.2	8
$C_{21}(B)$	1.68	

NOTES.—(1) Coordinates obtained using RC2 position of NGC 7531 (Table 1), assuming center of dwarf is 160'' west, 34'' south of the nucleus of NGC 7531. (2) From Corwin, de Vaucouleurs, and de Vaucouleurs 1985. (3) For this object the standard RC2 isophotal diameter does not exist. (4) Diameter and axis ratio measured at Holmberg's standard isophotal surface brightness level, assuming that this corresponds to $\mu_B = 26.6$ mag arcsec⁻² (see RC2). (5) Mean surface brightness within the effective aperture A_e . (6) Same as (4), corrected for the RC2 model of Galactic extinction. (7) Mean surface brightness within the effective ellipse transmitting half the total *B*-band flux (ellipse defined by orientation parameters $q = 0.42$, $\theta_0 = 171^\circ$). (8) Integrated colors within the effective ellipse.

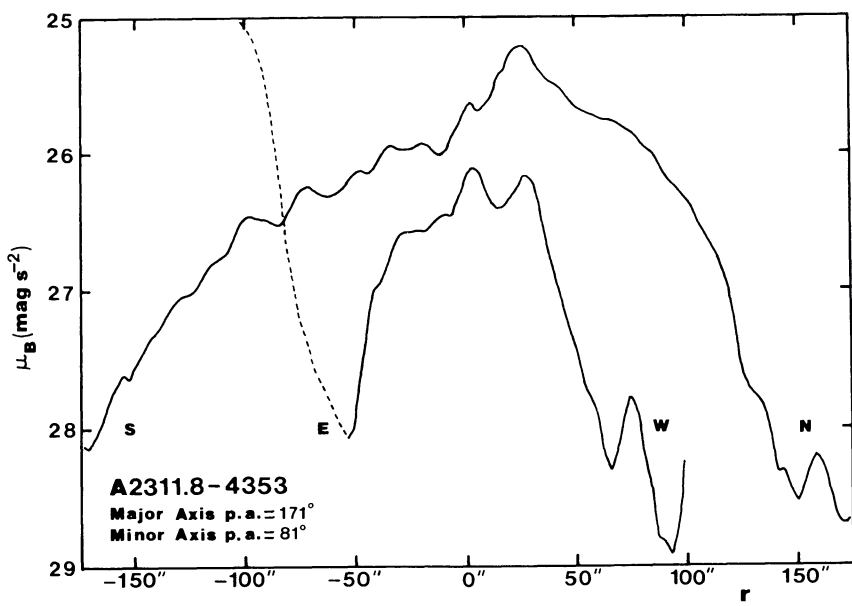


FIG. 39.—Major- and minor-axis *B*-band luminosity profiles of A2311.8–4353, based on CTIO plate 5297. The minor-axis profile has been displaced by +0.5 mag for clarity, and the dashed part of this profile represents the region where the southwest spiral arm of NGC 7531 is crossed. The central position corresponds to a point 160'' west, 34'' south of the nucleus of NGC 7531.

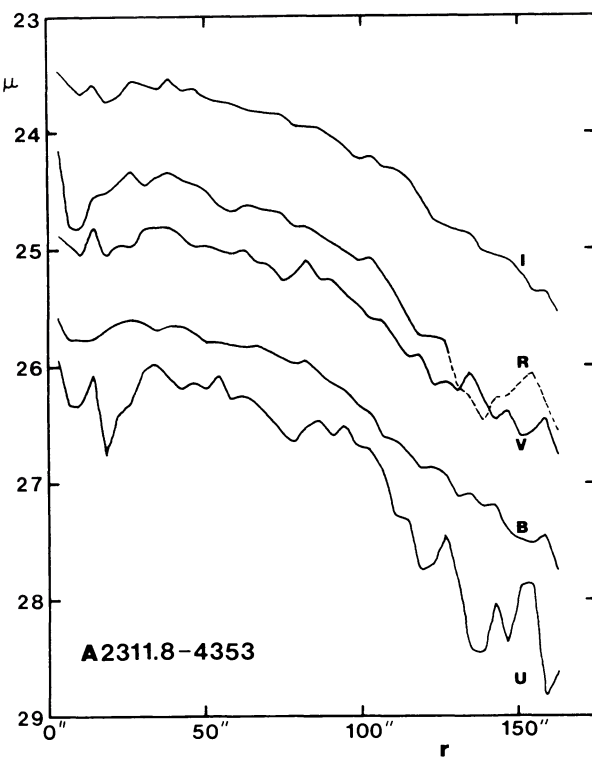


FIG. 40.—Azimuthally averaged luminosity profiles of A2311.8-4353 in all passbands, from averages within ellipses having an axis ratio $q = 0.42$ and a (1950) major-axis position angle of 171° .

TABLE 14
AZIMUTHALLY AVERAGED SURFACE PHOTOMETRY OF A2311.8-4353^a

r	μ_U	μ_B	μ_V	μ_R	μ_I	r	μ_U	μ_B	μ_V	μ_R	μ_I
0''.....	26.14	25.68	24.93	24.58	23.52	83'' ...	26.51	25.96	25.09	24.80	23.95
3	25.94	25.59	24.88	24.14	23.47	87	26.45	26.07	25.27	24.89	23.97
7	26.34	25.78	24.97	24.82	23.58	91	26.60	26.16	25.27	24.95	24.05
11	26.32	25.76	25.07	24.82	23.68	95	26.50	26.22	25.40	25.03	24.13
15	26.05	25.76	24.80	24.54	23.59	99	26.69	26.34	25.48	25.11	24.23
19	26.76	25.68	25.06	24.50	23.75	103	26.71	26.41	25.60	25.07	24.20
23	26.39	25.63	24.94	24.41	23.69	107	26.89	26.60	25.61	25.22	24.29
27	26.31	25.59	24.98	24.32	23.56	111	27.27	26.64	25.78	25.40	24.32
31	26.02	25.62	24.82	24.46	23.58	115	27.30	26.74	25.93	25.58	24.38
35	25.97	25.69	24.81	24.38	23.64	119	27.75	26.87	25.90	25.75	24.55
39	26.08	25.65	24.80	24.33	23.53	123	27.69	26.86	26.16	25.75	24.75
43	26.21	25.65	24.89	24.40	23.65	127	27.43	26.93	26.13	25.79	24.81
47	26.12	25.70	24.98	24.44	23.62	131	27.85	27.12	26.23	26.19	24.85
51	26.20	25.80	24.96	24.50	23.71	135	28.43	27.09	26.05	26.27	24.87
55	26.06	25.80	25.01	24.64	23.74	139	28.46	27.22	26.28	26.49	25.03
59	26.29	25.83	25.04	24.69	23.75	143	28.02	27.18	26.47	26.27	25.05
63	26.24	25.84	25.00	24.62	23.81	147	28.39	27.43	26.37	26.26	25.10
67	26.32	25.83	25.12	24.65	23.82	151	27.87	27.50	26.61	26.15	25.19
71	26.44	25.88	25.14	24.68	23.85	155	27.85	27.52	26.57	26.05	25.36
75	26.57	25.94	25.27	24.69	23.86	159	28.83	27.44	26.43	26.32	25.36
79	26.66	25.99	25.21	24.81	23.95	163	28.60	27.77	26.78	26.58	25.56

^aBased on averages within elliptical annuli having an apparent axis ratio of $q = 0.42$ and a major-axis position angle of $\theta_0 = 171^\circ$. All surface brightnesses are in mag arcsec $^{-2}$.

and de Vaucouleurs (1981) have shown that for a pure exponential disk system, the two mean surface brightnesses are related by the quadratic relation

$$\mu'_e \sim m'_e - 1.26(\log R_{25})^2,$$

where R_{25} is the isophotal axis ratio at the surface brightness level $\mu_B = 25.0$ mag arcsec $^{-2}$. Since this isophote does not exist for the dwarf, I use the axis ratio associated with the Holmberg diameter, $\log R_{Ho} = 0.38 \pm 0.02$, which implies that $m'_e - \mu'_e$ should be ~ 0.18 mag. This agrees well with the observed value.

The extinction-corrected mean effective surface brightness, $m'_{e0} = m'_e - A_B(G) = 25.83$ mag arcsec $^{-2}$, can be compared with similar data for a large sample of "DDO dwarfs" observed by de Vaucouleurs, de Vaucouleurs, and Buta (1981, hereafter VVB). Here $A_B(G)$ refers to the RC2 Galactic extinction model. Comparison with Figure 2 of VVB shows that the mean effective surface brightness of A2311.8-4353 is fainter than all of the DDO dwarfs measured. A further comparison can be made for the colors. Table 13 gives integrated colors of A2311.8-4353 within the effective ellipse, whose semimajor axis radius is 101''. These should be more reliable than total colors obtained by extrapolating the average profiles in the other passbands. Corrected for Galactic extinction, the observed effective colors correspond to $(B-V)'_e \sim 0.73$ and $(U-B)'_e \sim 0.4$. For comparison, VVB showed that, for the DDO dwarfs, the average corrected mean effective colors are $\langle(B-V)_e \rangle \sim 0.4$, $\langle(U-B)_e \rangle \sim -0.2$, which would make A2311.8-4353 redder than the typical DDO dwarf. Instead, the object is more similar to the red dwarf irregulars observed in the Virgo Cluster by Gallagher and Hunter (1986). The colors (especially $U-B$) are uncertain in any case, but the object is very smooth and shows no obvious tracers of recent star formation. Photoelectric confirmation of the colors derived here would be worthwhile before further interpretation is made.

The distance to A2311.8-4353 would be needed in order to assess its intrinsic properties. Were it at the same distance as NGC 7531, it would have an absolute magnitude $M_T^0(B) = -16.6$, similar to that of the Small Magellanic Cloud (de Vaucouleurs 1978), but it would not be a dwarf in size. The Holmberg diameter is 0.58 times that of NGC 7531. I suggest that the low-velocity range be searched near NGC 7531 to detect any possible neutral hydrogen gas associated with the dwarf, for a better assessment of the distance of this curious object. Note that if it turns out that the two galaxies really are at the same distance, then a weak interaction between them may provide a possible explanation for the asymmetries observed in the rotation curve and outer arms of NGC 7531.

REFERENCES

- Aaronson, M., Dawe, J. A., Dickens, R. J., Mould, J. R., and Murray, J. B. 1981, *M.N.R.A.S.*, **195**, 1.
- Athanassoula, E., and Bosma, A. 1985, *Ann. Rev. Astr. Ap.*, **23**, 147.
- Athanassoula, E., Bosma, A., Crézé, M., and Schwarz, M. P. 1982, *Astr. Ap.*, **107**, 101.
- Bessell, M. S. 1979, *Pub. A.S.P.*, **91**, 589.
- Boroson, T. 1981, *Ap. J. Suppl.*, **46**, 177.
- Bosma, A. 1978, Ph.D. thesis, University of Groningen.
- Bottinelli, L., Gouguenheim, L., Paturel, G., and de Vaucouleurs, G. 1983, *Astr. Ap.*, **118**, 4.
- Burstein, D. 1979, *Ap. J.*, **234**, 435.
- Buta, R. 1984, *Univ. Texas Pub. Astr.*, No. 23.
- _____. 1986a, *Ap. J. Suppl.*, **61**, 609 (Paper I).
- _____. 1986b, *Ap. J. Suppl.*, **61**, 631 (Paper II).
- Buta, R., and de Vaucouleurs, G. 1982, *Ap. J. Suppl.*, **48**, 219.
- Carignan, C. 1983, Ph.D. thesis, Australian National University.
- Corwin, H. G. 1981, Ph.D. thesis, University of Edinburgh.
- Corwin, H. G., de Vaucouleurs, A., and de Vaucouleurs, G. 1985, *Southern Galaxy Catalogue* (*Univ. Texas Monog. Astr.*, No. 4) (SGC).
- Davoust, E., and de Vaucouleurs, G. 1980, *Ap. J.*, **242**, 30.
- de Vaucouleurs, G. 1956, *Mem. Commonwealth Obs. Mt. Stromlo*, Vol. 3, No. 13.
- _____. 1959, *Handbuch der Physik*, **53**, 275.
- _____. 1963, *Ap. J. Suppl.*, **8**, 31.
- _____. 1975a, in *Stars and Stellar Systems*, Vol. 9, *Galaxies and the Universe*, ed. A. Sandage, M. Sandage, and J. Kristian (Chicago: University of Chicago Press), p. 557.
- _____. 1975b, *Ap. J. Suppl.*, **29**, 193.
- _____. 1977, in *The Evolution of Galaxies and Stellar Populations*, ed. B. Tinsley and R. Larson (New Haven: Yale University Observatory), p. 43.
- _____. 1978, *Ap. J.*, **223**, 730.
- _____. 1983, *Ap. J.*, **268**, 451.
- de Vaucouleurs, G., and Buta, R. 1980a, *A.J.*, **85**, 637.
- _____. 1980b, *Ap. J. Suppl.*, **44**, 451.
- de Vaucouleurs, G., and Capaccioli, M. 1979, *Ap. J. Suppl.*, **40**, 699.
- de Vaucouleurs, G., and de Vaucouleurs, A. 1964, *Reference Catalogue of Bright Galaxies* (*Univ. Texas Monog. Astr.*, No. 1).
- de Vaucouleurs, G., de Vaucouleurs, A., and Buta, R. 1981, *A.J.*, **86**, 1429 (VVB).
- de Vaucouleurs, G., de Vaucouleurs, A., and Corwin, H. G. 1976, *Second Reference Catalogue of Bright Galaxies* (Austin: University of Texas Press) (RC2).
- de Vaucouleurs, G., de Vaucouleurs, A., and Nieto, J. L. 1979, *A.J.*, **84**, 1811.
- de Vaucouleurs, G., and Olson, D. W. 1982, *Ap. J.*, **256**, 346.
- de Vaucouleurs, G., Pence, W. D., and Davoust, E. 1983, *Ap. J. Suppl.*, **53**, 17.
- de Vaucouleurs, G., and Peters, W. L. 1981, *Ap. J.*, **248**, 395.
- Elmegreen, B. G., and Elmegreen, D. M. 1985, *Ap. J.*, **288**, 438.
- Elmegreen, D. M. 1980, *Ap. J. Suppl.*, **43**, 37.
- _____. 1981, *Ap. J. Suppl.*, **47**, 229.
- Elmegreen, D. M., and Elmegreen, B. G. 1982, *M.N.R.A.S.*, **201**, 1021.
- _____. 1984, *Ap. J. Suppl.*, **54**, 127.
- Faber, S. M., and Gallagher, J. S. 1979, *Ann. Rev. Astr. Ap.*, **17**, 135.
- Gallagher, J. S., and Hunter, D. A. 1986, *A.J.*, **92**, 557.
- Grierson, D. G. 1980, *A.J.*, **85**, 789.
- Jensen, E. B., Talbot, R. J., and Dufour, R. J. 1981, *Ap. J.*, **243**, 716.
- Jones, W., Obitts, D., Gallet, R., and de Vaucouleurs, G. 1967, *Astrophysical Surface Photometry by Numerical Mapping Techniques* (*Univ. Texas Pub. Astr.*, Vol. 1, Ser. II, No. 8).
- Kalnajs, A. J. 1978, in *IAU Symposium 77, The Structure and Properties of Nearby Galaxies*, ed. E. M. Berkhuijsen and R. Wielebinski (Dordrecht: Reidel), p. 113.
- _____. 1983, in *IAU Symposium 100, Internal Kinematics and Dynamics of Galaxies*, ed. E. Athanassoula (Dordrecht: Reidel), p. 87.
- Kent, S. M. 1986, *A.J.*, **91**, 1301.
- Kormendy, J. 1977, *Ap. J.*, **214**, 359.
- _____. 1979, *Ap. J.*, **227**, 714.
- _____. 1982, in *Morphology and Dynamics of Galaxies* (Geneva: Geneva Observatory), p. 115.
- Kormendy, J., and Norman, C. A. 1979, *Ap. J.*, **233**, 539.
- Landolt, A. U. 1983, *A.J.*, **88**, 439.
- Larson, R. B., and Tinsley, B. M. 1978, *Ap. J.*, **219**, 46.
- Lin, C. C. 1971, *Highlights Astr.*, **2**, 88.
- Lindblad, B. 1941, *Stockholm Obs. Ann.*, Vol. 13, No. 8, p. 25.
- _____. 1955, *Stockholm Obs. Ann.*, Vol. 18, No. 6.
- Linblad, P. O., and Jorsater, S. 1981, *Astr. Ap.*, **97**, 56.
- Longo, G., and de Vaucouleurs, A. 1983, *A General Catalogue of Photoelectric Magnitudes and Colors in the U, B, V System of 3,578 Galaxies Brighter than the 16th V-Magnitude* (*Univ. Texas Monog. Astr.*, No. 3).
- Lynden-Bell, D. 1979, *M.N.R.A.S.*, **187**, 101.
- Miller, R. H. 1978, *Ap. J.*, **226**, 81.
- Miyamoto, M., and Nagai, H. 1975, *Pub. Astr. Soc. Japan.*, **27**, 533.
- Olson, D. W., and de Vaucouleurs, G. 1981, *Ap. J.*, **249**, 68.
- Perek, L. 1962, *Adv. Astr. Ap.*, **1**, 165.

- Roberts, W. W., Roberts, M. S., and Shu, F. H. 1975, *Ap. J.*, **196**, 381.
 Rubin, V. C., Burstein, D., Ford, W. K., and Thonnard, N. 1985, *Ap. J.*, **289**, 81.
 Rubin, V. C., Ford, W. K., and Thonnard, N. 1980, *Ap. J.*, **238**, 471.
 Rubin, V. C., Ford, W. K., Thonnard, N., and Burstein, D. 1982, *Ap. J.*, **261**, 439.
 Sandage, A. 1961, *The Hubble Atlas of Galaxies* (Carnegie Inst. Washington Pub., No. 618).
 Sandage, A., and Tammann, G. 1981, *A Revised Shapley-Ames Catalog of Bright Galaxies* (Carnegie Inst. Washington Pub., No. 635) (RSA).
 Sanders, R. H., and Bania, T. M. 1976, *Ap. J.*, **204**, 341.
 Schwarz, M. P. 1979, Ph.D. thesis, Australian National University.
 _____. 1981, *Ap. J.*, **247**, 77.
 _____. 1984a, *Astr. Ap.*, **133**, 222.
 _____. 1984b, *M.N.R.A.S.*, **209**, 93.
 _____. 1984c, *Proc. Astr. Soc. Australia*, **5**, 458.
 Schwarz, M. P. 1985, *M.N.R.A.S.*, **212**, 677.
 Schweizer, F. 1976, *Ap. J. Suppl.*, **31**, 313.
 Searle, L., Sargent, W. L. W., and Bagnuolo, W. G. 1973, *Ap. J.*, **179**, 427.
 Seiden, P. E., and Gerola, H. 1979, *Ap. J.*, **233**, 56.
 Shobbrook, R. 1966, *M.N.R.A.S.*, **131**, 351.
 Simien, F., and de Vaucouleurs, G. 1986, *Ap. J.*, **302**, 564.
 Simkin, S. M. 1967, *A.J.*, **72**, 1032.
 Simkin, S. M., Su, H. J., and Schwarz, M. P. 1980, *Ap. J.*, **237**, 404.
 Taylor, K., and Atherton, P. D. 1980, *M.N.R.A.S.*, **191**, 675.
 Toomre, A. 1964, *Ap. J.*, **139**, 1217.
 Tsikoudi, V. 1977, *Univ. Texas Pub. Astr.*, No. 10.
 van der Kruit, P. C. 1974, *Ap. J.*, **188**, 3.
 _____. 1976, *Astr. Ap.*, **52**, 85.
 Warner, P. J., Wright, M. C. H., and Baldwin, J. E. 1973, *M.N.R.A.S.*, **163**, 163.

RONALD J. BUTA: Department of Astronomy, University of Texas, Austin, TX 78712